Mechanistic prediction of drug-induced proarrhythmic risk via simulation of afterdepolarisations in cardiac myocytes

Beth McMillan
Somerville College

Computational Cardiovascular Science Group
Department of Computer Science
University of Oxford

Trinity Term 2022

This thesis is submitted to the Department of Computer Science, University of Oxford, for the degree of Doctor of Philosophy. This thesis is entirely my own work, and, except where otherwise indicated, describes my own research.

Abstract

During the drug development process, many promising compounds are discarded due to risk of drug-induced Torsades de Pointes. Testing for block of the hERG potassium current is a sensitive way to rule out torsadogenic risk, but it lacks specificity, meaning that safe, useful medicines may be unduly prevented from coming to the market. The safety of some compounds which block the hERG channel but are not proarrhythmic may be due to their effects on other cardiac ion currents. Computational methods which integrate early-stage ion current screening data with electrophysiological modelling of cardiomyocytes offer a fast, low-cost method for prediction, and could reduce the requirements for animal experimentation. In this thesis, we present a novel method for predicting proarrhythmic risk by simulating early afterdepolarisations in human ventricular cardiac cell models. By applying ion current drug block to the cell model and provoking early afterdepolarisations using a range of interventions, we developed several metrics for the prediction of risk.

Interventions included simulation of the Long QT syndromes and injury current. We assessed the accuracy of prediction using machine learning techniques and leave-one-out cross-validation. We also compared our metrics to previous metrics that have been suggested in the literature, and investigated the effect of combining metrics together and adding pro- and anti-arrhythmic modifiers on classification accuracy.

The EAD metrics outperformed every other metric we calculated using this dataset, with the exception of APD90. The EAD metrics were also able to classify correctly some drugs which APD90 gets wrong, showing that they can provide extra information over the APD90 metric in some cases.

Acknowledgements

Thanks to the staff at the John Radcliffe Hospital who saved my life from a pulmonary embolism in June 2021.

I would like to thank my supervisors Blanca, Xin, and Elisa for their unwavering support during a very difficult period in my life, and for being inspirational scientists. I would also like to thank my previous supervisors, Gary and Dave, for sharing their knowledge with me. I certainly learned a lot from them. Thanks also to Louise, Kylie, and Ross for their help and companionship, and to Joe and Louie for all of our pair-programming sessions.

My DPhil was funded by the Engineering and Physical Sciences Research Council through the Systems Biology Doctoral Training Centre. I'd like to thank my cohort at the DTC for accompanying me on my learning journey - especially Izzy, Paul, Anna, Ali, Kathryn, and Will, for all the board games and group therapy sessions. To John, for always believing in me, looking after me, and putting up with all the weird songs I sang to the cat. Thanks to Eoin for his horrifying anecdotes and pub lunches, to Reb for not killing him in his sleep, and to both of them for looking after the cat. Thanks to the Somerville College MCR, especially Sacha, Nele, Tallulah, and Lauren for all the hours we spent playing Settlers of Catan and putting the world to rights. Thanks to Wren, Laura, Benji, and Astrid for keeping me sane for all these years.

Finally, thanks go to my family. To my mum, for her emotional, financial, and practical support throughout this process, as well as her proofreading and cheering-up services. To my dad, for teaching me to program on a Commodore 64, and to both of my parents for nurturing my love of maths and learning. To my brother Paul, for putting me up on his sofa for a month, for our experimental cooking sessions - especially the watermelon curry - and for providing me with sage advice. To my other brothers Peter and Michael, as well as Michelle, Louise, Hannah, Ezra and Rafa, for long Zoom calls, rowdy family holidays, and generally making my life more fun.

Publications

Below is a list of publications related to the work described in this thesis:

Beth McMillan, David J. Gavaghan, and Gary R. Mirams. Early afterdepolarisation tendency as a simulated pro-arrhythmic risk indicator. Toxicology Research 6(6), 2017.

Fergus R. Cooper, Ruth E. Baker, Miguel O. Bernabeu, Rafel Bordas, Louise Bowler, Alfonso Bueno-Orovio, Helen M. Byrne, Valentina Carapella, Louie Cardone-Noott, Jonathan Cooper, Sara Dutta, Benjamin D. Evans, Alexander G. Fletcher, James A. Grogan, Wenxian Guo, Daniel G. Harvey, Maurice Hendrix, David Kay, Jochen Kursawe, Philip K. Maini, **Beth McMillan**, Gary R. Mirams, James M. Osborne, Pras Pathmanathan, Joe M. Pitt-Francis, Martin Robinson, Blanca Rodriguez, Raymond J. Spiteri, and David J. Gavaghan. Chaste: Cancer, Heart and Soft Tissue Environment. Journal of Open Source Software, 5(47), 2020.

Conference abstract: **Beth McMillan**, Ross H. Johnstone, David J. Gavaghan, Gary Mirams. A Comparison of Existing and New Methods for Torsade de Pointes Risk Classification Based on Multi-ion Channel Screening. Journal of Pharmacological and Toxicological Methods, 2017.

Conference abstract: **Beth McMillan**, David J. Gavaghan, Gary Mirams. Predicting drug-induced arrhythmia using afterdepolarisations. Journal of Pharmacological and Toxicological Methods, 2016.

Posters and presentations

- Physiology conference poster July 2016
- In Vitro Toxicology Society conference presentation November 2015
- Safety Pharmacology Society conference posters September 2015 and 2016
- Gordon Research conference poster March 2015
- ID2 conference presentation June 2014

Awards

- Somerville College Barbara Craig fund for Physiology 2016.
- Physiology Society travel grant for Physiology 2016.
- Student bursary for 2015 IVTS meeting.
- Selected to give an oral presentation at 2015 IVTS meeting.
- Selected to give an oral presentation at ID2 conference in 2014.

Contents

Abbreviations

ATP	Adinosine tri-phosphate
CICR	Calcium-induced calcium release
CiPA	Comprehensive in-vitro Pro-arrhythmia Assay
DAD	Delayed afterdepolarisation
EAD	Early afterdepolarisation
EC	Electrotonic current
$\mathrm{EFTPC_{max}}$	Maximum effective free therapeutic plasma concentration
hERG	Human ether-a-gogo related gene
$\mathrm{IC_{50}}$	Half maximal inhibitory concentration
$\mathrm{I_{CaL}}$	L-type calcium current
$\mathrm{I_{Kr}}$	Rapid rectifier (hERG) potassium current
$\mathrm{I_{Na}}$	Fast sodium current
$\mathrm{I_{pNa}}$	Persistent sodium current
LDA	Linear discriminant analysis
LQTS	Long QT syndrome
RyR	Ryanodine receptor
SERCA	Sarco/endoplasmic reticulum calcium ATPase
SVM	Support vector machines
TdP	Torsades de Pointes

Chapter 1

Introduction

Contents

1.1 Introduction

Torsades de Pointes (TdP) is a type of cardiac arrhythmia that can cause cardiac arrest or sudden death (Schwartz et al., 2012; Fabiato and Coumel, 1991). TdP can be caused by some medicines (Bauman et al., 1984; Woosley et al., 1993; Bryan, 2011; Rampe et al., 1997; Committee on Safety of Medicines and Medicines Control Agency, 2000), and so prediction of potential drug-induced TdP is a central part of any drug development programme, and is therefore of great importance to both the pharmaceutical industry and regulatory authorities. Prediction of drug-induced TdP has previously relied upon block of the hERG cardiac potassium current (European Medicines Agency, 2005). However, this measure may be too restrictive, preventing useful drugs from making it to market (Stockbridge et al., 2013), as some drugs block hERG but are not linked to TdP (Milberg and Haverkamp, 2005; Cobbe, 2004), possibly due to their effects on other ion channels. Computational modelling is therefore currently of great interest in proarrhythmic risk prediction. Simulated action potential duration and QT prolongation have been used as a metric for TdP risk prediction. However, some drugs which prolong QT are not linked to Torsades (Sager, 2008). The Comprehensive in-vitro Pro-arrhythmia Assay (CiPA) is a proposal to use multi-ion channel screening in combination with human stem cell-derived cardiomyocytes and computational cardiac modelling to create new metrics for the prediction of drug-induced TdP (Sager et al., 2014).

Progress towards the goals of the CiPA initiative includes updated versions of the O'Hara et al. (2011) model (Li et al., 2017; Dutta et al., 2017; Tomek et al., 2019), novel metrics based on current balance during the action potential (Li et al., 2017; Dutta et al., 2017) and on EADs provoked by increased drug concentration (Passini et al., 2017; Christophe, 2013; Christophe and Crumb, 2019; Christophe, 2022), as well as representations of variability in ion current measurements (Johnstone et al., 2016; Li et al., 2019) and in underlying physiology (Passini et al., 2017).

The existing work on the proarrhythmia problem could be extended by investigating torsadogenic effects at physiological drug concentrations, and considering the genesis of EADs provoked by simulation of disease states such as the Long QT syndromes or injury current.

1.2 Rationale for DPhil project

Torsades de Pointes (TdP) is a particular type of polymorphic ventricular tachycardia, characterised by an unusual electrocardiogram, in which the QRS complex appears to be twisted around the baseline. TdP usually spontaneously resolves, sometimes causing syncope (sudden fainting due to a drop in blood pressure), but it can also cause cardiac arrest or sudden death (Schwartz et al., 2012; Fabiato and Coumel, 1991).

Several classes of medications have been reported to cause Torsades de Pointes. Anti-arrhythmic drugs, such as quinidine, (Bauman et al., 1984) are commonly linked to TdP. Terfenadine, a non-sedating anti-histamine, was one of the first non-cardiac drugs to be linked to increased TdP risk (Woosley et al., 1993). Terfenadine was withdrawn from the market in 1997 after being linked to 41 cases of TdP, one of which was lethal (Bryan, 2011). Cisapride is a drug that was used for treating gastroesophageal reflux disease (Rampe et al., 1997). After causing

97 cases of TdP, of which six were fatal, cisapride was withdrawn from the market (Committee on Safety of Medicines and Medicines Control Agency, 2000).

Quinidine, terfenadine, and cisapride were all found to strongly block I_{Kr}, the rapid delayed rectifying potassium current in the heart, which is carried by the channel whose primary subunit is a product of the human ether-a-go-go related gene (hERG) (Po et al., 1999; Curran et al., 1995; Woosley et al., 1993; Rampe et al., 1997).

Since these discoveries, testing for hERG block has become a mandatory requirement for new pharmaceuticals (European Medicines Agency, 2005). hERG block as a measure of TdP risk is very sensitive, i.e. it gives few false negatives, and has prevented torsadogenic drugs from entering the market. Certain drugs that are still on the market, such as verapamil and ranolazine, block hERG but are not linked with TdP (Milberg and Haverkamp, 2005; Cobbe, 2004). There are therefore concerns that hERG block lacks specificity (gives false positives for TdP risk), preventing the development of potentially useful drugs (Stockbridge et al., 2013). As such, elucidation of other factors that mediate TdP risk is needed.

Early afterdepolarisations (EADs), phenomena in which the membrane depolarises a second time during the action potential, are heavily implicated in the onset of TdP (Frommeyer and Eckardt, 2015). Hearts suffering from TdP show EADs alongside transmural dispersion of repolarisation (Habbab and El-Sherif, 1990; El-Sherif et al., 1988; Choi et al., 2002; Roden, 1993).

The prediction of arrhythmias by *in silico* modelling of action potentials in response to ion channel block offers a new way to test novel compounds at the pre-clinical stage. A previous study created an improved measure of a compound's propensity for causing TdP arrhythmias, using simulated action potential duration as a metric (Mirams et al., 2011). The approach takes into account the contributions of multiple ion channels to the shape and length of the action potential, and classifies drugs into discrete risk categories, based on their effect on action potential duration. This method was shown to be more accurate than the commonly-used hERG safety factor, which is defined as the ratio of hERG IC_{50} to effective free therapeutic plasma concentration (EFTPC), or $\log_{10}(\text{hERG IC}_{50}/\text{EFTPC}_{\max})$ (Redfern et al., 2003). Simulation studies have been extended to predict results of rabbit wedge studies and the Thorough QT study (Beattie et al., 2013; Mirams et al., 2014).

Another study used principal component analysis to assemble a large number of biomarkers from different models, with the results suggesting that a two-dimensional binary classification based on both the simulated diastolic calcium concentration and the APD50 was effective at separating drugs into positive or negative for torsadogenicity (Lancaster and Sobie, 2016). The appearance of simulated EADs at increased drug concentrations has been investigated previously as a risk indicator for TdP (Christophe, 2013).

Passini et al. (2017) represented human variability using a population of models approach and created a TdP score metric using repolarisation abnormality counts in the population. In Li et al. (2017), the total persistent sodium and L-type calcium currents during a single action potential were used to create the cqInward metric, which was then updated by Dutta et al. (2017) to create the qNet metric, which was assessed in Li et al. (2019).

1.3 Thesis goals

In this thesis, we aim to develop an improved metric for the prediction of torsadogenic risk, using computational modelling of early afterdepolarisations in human ventricular myocytes.

First, we aim to create a dataset of drug data, including IC50s, EFTPCs, and torsadogenic risk categories, using manual patch clamp ion current measurements where possible, from drugs of known levels of torsadogenic risk. We will use this dataset to implement ion current block in a human ventricular cell model to mimic effects of the drugs at realistic physiological concentrations.

The next aim of this thesis is to create a suite of physiology-based EAD-inducing interventions that can be applied to cell models, including simulation of the changes in ion current conductance from the Long QT syndromes and injury current from acute ischaemia. We aim to create a utility for detecting and categorising afterdepolarisations in simulations, and implement a thresholding algorithm for detecting the level of intervention required to induce an EAD.

Using the EAD threshold data, we aim to classify the drug dataset into risk categories using machine learning techniques, and to use these classifications to assess the accuracy of each metric, compared to other published metrics, which will be calculated using the same drug data. We will compare the accuracy of different machine learning techniques for this classification problem, and use combinations of metrics to increase the separation between risk categories. We will also assess categorisation accuracy for a binary classifier, using both the most extreme risk categories and the entire dataset, in order to get a broader picture of the strengths and weaknesses of each type of metric. We hypothesise that the level of pro-arrhythmic intervention necessary to provoke an EAD will relate to the risk category of the drug, allowing for improved categorisation over ion current block data alone.

The final aim of this thesis is to improve upon the EAD threshold metrics by simulating both pro- and anti-arrhythmic conditions, including different cycle lengths, hypo- and hyperkalemia, drug concentration, and choice of epi- or endocardial methods. We hypothesise that differential effects under each of these conditions between drug safety categories might increase the separation between groups.

1.4 Structure of thesis

In Chapter 2, I lay out the biological and electrophysiological background to computational cardiac modelling, and discuss the history of electrophysiological models. Chapter 3 is a review of the relevant literature about Torsades de Pointes arrhythmias, early afterdepolarisations, and the prediction of drug-induced pro-arrhythmic risk. The computational methods used for our study are outlined in Chapter 4. The results are presented in Chapter 5, the discussion is in Chapter 6, and then the conclusion can be found in Chapter 7.

Chapter 2

Background

Contents

In this chapter, I will describe the physiology and electrophysiology of the human heart, and then lay out the history of computational cardiac modelling.

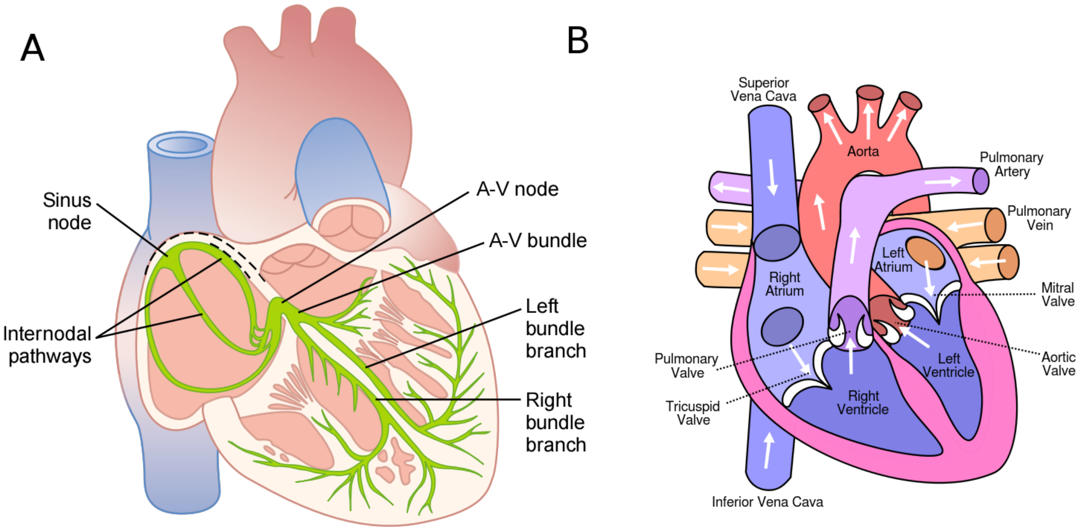

Figure 2.1: A) Labelled diagram of the electrical systems inside the heart. Labelled are the sinus or sinoatrial node, the atrioventricular (A-V) node, the atrioventricular bundle (also know as the bundle of His), the left and right bundle branches, and the pathways between the nodes (Hall, 2010). B) Labelled diagram of the physiology of the heart. Labelled are the blood vessels: the superior and inferior venae cavae, the pulmonary artery, pulmonary vein, and the aorta; the right and left atria and ventricles; and the mitral, pulmonary, aortic and tricuspid valves (Wikimedia Commons, 2016).

2.1 Physiology of the heart

Blood flow around the human body is maintained by the rhythmic and orderly contraction of each of the four chambers of the heart. The circulatory system is vital for the transport of oxygen and nutrients to all of the parts of the body. Defects in heart rhythm can cause fainting, low blood pressure and, in some cases, sudden death (Hall, 2010).

A diagram of the anatomy of the human heart can be found in Figure 2.1B. In a single cardiac cycle, first, blood flows into both the left and right atria of the heart from the pulmonary vein and the venae cavae. Increasing pressure inside the atria forces the mitral and tricuspid valves to open. The walls of the atria then contract, forcing the blood into the ventricles (Hall, 2010).

The rising pressure in the ventricles closes the mitral and tricuspid valves and opens the aortic and pulmonary valves. The ventricles then contract from the bottom to the top, squeezing blood out of the heart (Hall, 2010).

Blood from the right side of the heart is pumped into the lungs to be oxygenated, while the left side of the heart is used to supply the circulatory system of the rest of the body. The order and pace at which these events occur is vital for correct heart rhythm (Hall, 2010).

2.2 Electrophysiology of the heart

The contraction of the heart is triggered by a wave of electrical activity that travels from the group of pacemaker cells at the top of the right atrium. This group of cells is known as the sinoatrial or sinus node. The signal is then conducted down through the muscle cells (myocytes) of both atria, causing them to contract. The wave of excitation then travels to the atrioventricular node at the centre of the heart and down, through the Bundle of His and the Purkinje fibres, to the bottom of the ventricles. Finally, the signal travels up the ventricles, causing the myocytes in the walls of the ventricles to contract, squeezing blood through the heart in the sequence described above (Sherwood, 2004). A diagram of the electrical systems in the heart can be seen in Figure 2.1A.

When an electrical current is carried in a wire, the charge is carried by electrons shared via metallic bonds. In a biological system, charge is carried by ions in solution. The electrical signal that originates in the sinoatrial node is caused by the movement of charged ions across the cell membrane of the sinoatrial node cells. Ion channels, pumps, and exchangers are formed of membrane proteins which are specific to particular ions. These allow passage of ions from the inside to the outside of the cell, and vice versa, as well as transport between intracellular compartments. Mathematical cardiac electrophysiological models commonly only consider voltage-dependent gating of these ionic currents; however, the currents can also be dependent on stretch, temperature, ATP, and methylation. Currents carried by sodium, potassium, calcium, chloride, and some other ions are involved in the process of electrical excitation in the heart (Hall, 2010).

In the sinoatrial node, thanks to a complex interplay between different voltage-gated ion channels in the cell membrane, the membrane potential oscillates rhythmically over time, as in Figure 2.2. This oscillation is what governs the rhythmic activity of the heart. The atrioventricular node, Purkinje fibres, and Bundle of His all show oscillating action potentials in isolation, and can act as secondary pacemakers if the sinoatrial node is not functioning. The rest of the

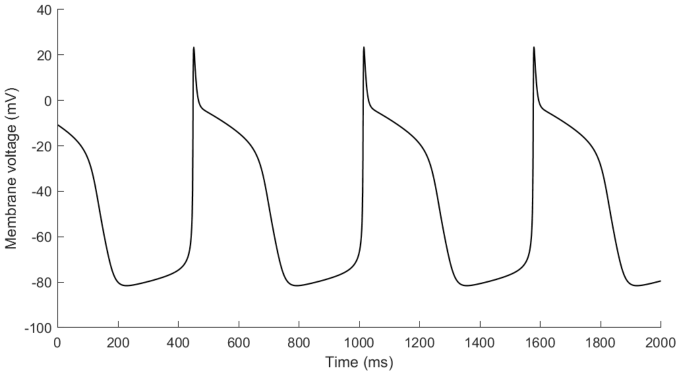

Figure 2.2: Graph of the action potential in a pacemaker cell (Noble, 1962). Simulation performed in OpenCOR (Garny and Hunter, 2015) using CVODE. Pacemaker cells show rhythmic depolarisations of the membrane.

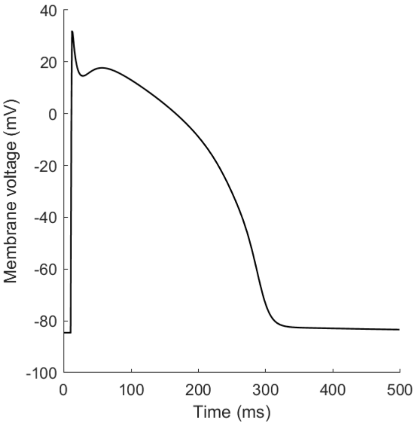

Figure 2.3: Graph of the action potential in a ventricular cell (Beeler and Reuter, 1977). Simulation performed in OpenCOR using CVODE.

cells of the heart, however, have a stable resting voltage, as in Figure 2.3. This means that in the absence of stimulation, the cells will not depolarise, except in certain disease states.

2.2.1 Sodium channels

The initial depolarisation at the beginning of an action potential is caused by the opening of voltage-gated SCN5A sodium channels in the membrane, allowing positively charged sodium ions to flood into the cell. The sodium channels are voltage-gated, meaning that when the membrane voltage reaches a particular threshold, they open. This voltage change is triggered, in a nonpacemaker cell, by a current of ions from neighbouring cells via “gap junctions” – holes in the membrane between cells. The ensuing flood of sodium ions makes the inside of the membrane less negative with respect to the outside, giving the membrane a positive voltage. Once the voltage has reached its maximum point, the voltage-gated sodium channels are inactivated, preventing them from opening again until the action potential has finished (Catterall, 2014).

2.2.2 Potassium channels

The repolarisation of the cell after the initial depolarisation is largely mediated by the action of the potassium channels. When potassium channels open, they allow the positively charged potassium ions out of the cell, returning the membrane voltage to its original resting value. The first channels to open are the transient outward potassium channels, which repolarise the cell during the early stage of repolarisation. These are followed by the opening of the slow rectifying delayed potassium channels, which are active during the plateau phase of the action potential. The rapid rectifying delayed potassium channels (also known as hERG channels) are responsible for the fast repolarisation of the cell after the plateau phase, and then the inward rectifier potassium current maintains the resting voltage (Nerbonne, 2014).

2.2.3 Calcium subsystem

The long-lasting (otherwise known as L-type) calcium channels are also triggered to open by the increase in membrane voltage during depolarisation. Through these calcium channels, positively charged calcium ions flow into the cell, slowing repolarisation and causing the plateau phase of the action potential (Rose and Backx, 2014).

All muscle cells, including cardiomyocytes, contain a store of calcium ions inside a membrane-bound organelle called the sarcoplasmic reticulum. The membrane of the sarcoplasmic reticulum contains ion channels, called ryanodine receptors or RyR, which are specific for calcium ions. These channels will allow calcium ion release from the sarcoplasmic reticulum only when there is a high local concentration of calcium ions on the cytoplasmic side of the membrane. This mechanism, called “calcium-induced calcium release” (CICR), is what allows the electrical excitation of the cell to be linked to contraction (Valdivia, 2014).

2.2.4 Homeostasis

In a cardiomyocyte, once the membrane voltage has reached its resting value, the outward potassium channels close, leaving only the inward potassium channel active (Nerbonne, 2014). Additionally, in order to maintain the levels of sodium and potassium inside and outside the cell that are necessary for the correct electrochemical gradients to cause ion flow, the sodium-potassium pump in the cell membrane uses ATP to exchange two potassium ions for three sodium ions. This creates a high concentration of sodium outside the cell, and a high concentration of potassium inside the cell.

In pacemaker cells, once the membrane has fully repolarised, the membrane potential slowly rises until it reaches the threshold for the opening of the sodium channels and another action potential is triggered. This slow depolarisation is caused by a mixture of sodium and potassium ions flowing into the cell (the so-called "funny current"), and the resistance of the membrane to potassium ions increasing, stopping the repolarisation (Lakatta et al., 2014).

The sarco/endoplasmic reticulum calcium ATPase (SERCA) is a calcium-specific pump which transports calcium ions back into the sarcoplasmic reticulum after the cell has finished contracting, restoring calcium levels within the sarcoplasmic reticulum, ready for the next contraction (Noble, 2004; Brini and Carafoli, 2014).

2.2.5 Excitation-contraction coupling

The contraction of muscle cells is caused by the action of myosin on long filaments of a protein called actin. Myosin is a motor protein, meaning that it uses ATP to create movement in only one direction. Myosin binds to actin filaments and "walks" along the filament. Actin filaments and myosin heads are arranged in the cell such that the movement of myosin pulls actin filaments towards the centre of the cell, bringing the rest of the cytoskeleton with them, and causing the cell to contract. When a muscle cell is at rest, the myosin-binding sites of the actin filament are obscured by a protein complex called tropomyosin, preventing contraction. The calcium ions released from the sarcoplasmic reticulum in CICR bind to troponin, allowing it to move away from the actin filament's active sites and allowing myosin heads to bind, causing contraction (Bers, 2014).

2.3 History of electrophysiological models

2.3.1 Hodgkin-Huxley squid giant axon model

The original electrophysiological model on which all cardiac models have been built was created in 1952 by Alan Hodgkin and Andrew Huxley (Hodgkin and Huxley, 1952). They described the electrical signal that passes down the giant axon of a squid when it is excited. The giant axon, which is large enough to be manipulated easily, controls the water jet propulsion system of a squid.

The basis of this mathematical model is an understanding of the cellular features as components in an electrical circuit. The membrane of a neuron acts like a capacitor, which means that ions accumulate on one side of the membrane, allowing it to store charge. This makes one side of the membrane more positive than the other side, leading to a potential difference, or voltage, across the membrane.

The flow of ions across the membrane acts as an electrical current. Three types of ionic current are considered in this model: the sodium (Na^+) ions that flow into the cell and cause depolarisation of the membrane, the potassium (K^+) ions that flow out to repolarise the membrane, and the "leak" current (a mixture of ions, including chloride ions), which flows in both directions.

The electrochemical gradients that power the flow of each type of ion are modelled as batteries, and the ion channels that permit ions to pass are represented by variable resistors.

I is the stimulus current that the cell receives from outside.

$\mathrm{I}_{\mathrm{Na}}, \mathrm{I}_{\mathrm{K}}$, and I_{l} are the sodium, potassium and leak currents, respectively.

C_{m} is the capacitance of the membrane (i.e. its ability to store charge).

E is the membrane voltage.

$\mathrm{R}_{\mathrm{Na}}, \mathrm{R}_{\mathrm{K}}$, and R_{l} are the resistance of the membrane to letting each type of ion through. These values are usually quoted in terms of the conductance (g) of the membrane, where $g = \frac{1}{\mathrm{R}}$.

$\mathrm{E}_{\mathrm{Na}}, \mathrm{E}_{\mathrm{K}}$, and E_{l} are the membrane potentials at which the flow of sodium, potassium or leak ions (respectively) through the membrane is zero.

As the current across the capacitor depends on the change in voltage over time and on the capacitance ($\mathrm{I}_{\mathrm{Capacitor}} = \mathrm{C}_{\mathrm{m}} . \frac{\mathrm{dV}}{\mathrm{dt}}$), and the four components of the current (that are wired in

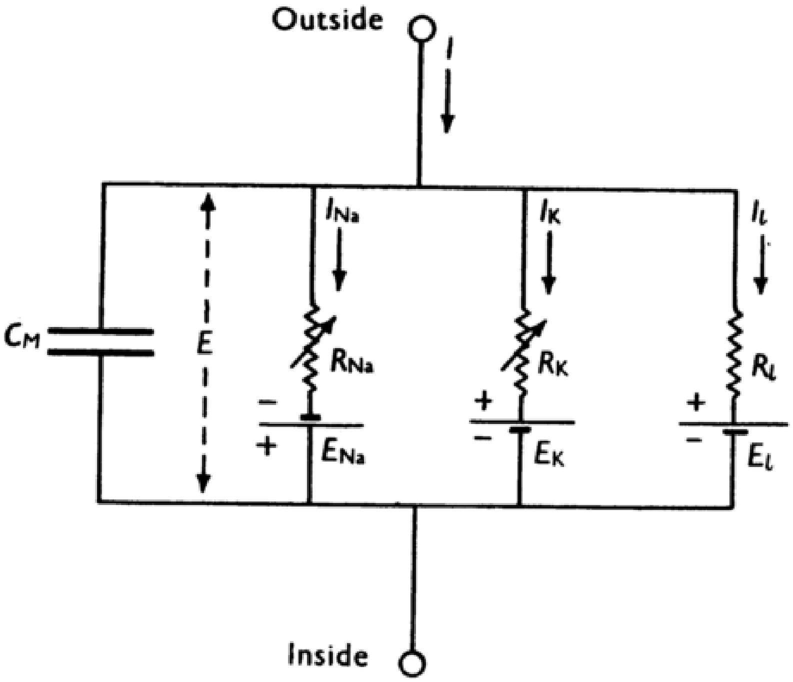

Figure 2.4: Diagram of circuit from Hodgkin & Huxley's paper

parallel) all add up to the stimulus current ($I_{stim} = I_{Capacitor} + I_{Na} + I_K + I_l$), the model's central differential equation,

$$\frac{dV}{dt} = \frac{I_{stim} - I_{Na} - I_K - I_l}{C_m}, \tag{2.1}$$

can be created, where $V = E - E_{resting}$, i.e. the difference between the current membrane voltage and the usual, or "resting" voltage.

One of the most interesting features of Hodgkin & Huxley's 1952 paper are its descriptions of a possible mechanistic basis for the permeability of the cell membrane to ions. This paper was written long before ion channels were discovered and characterised in mammalian cells, so the authors have modelled permeability as a function of charged particles that bind to ions and allow them to move across the membrane.

The opening, closing and inactivation of the ion channels is vital for the characteristic shape of the action potential in a nerve cell, shown in Figure 2.5. The action of the ion channels in nerve cells are different to those in cardiac cells and proceed in the following way:

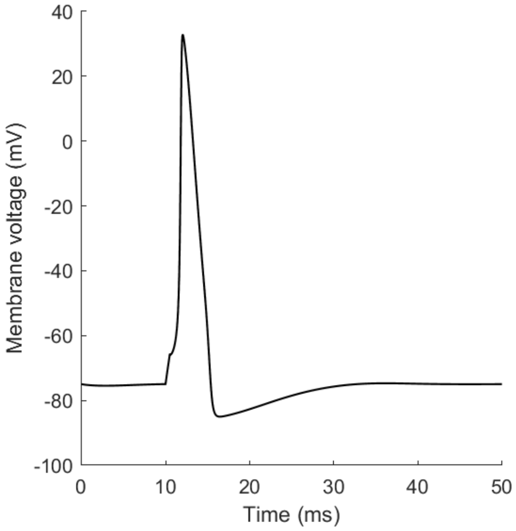

Figure 2.5: Graph of the action potential in a nerve cell (Hodgkin and Huxley, 1952). Simulation performed in OpenCOR using CVODE.

1) Sodium channels open and sodium floods into the cell (g_{Na} increases).

2) Potassium channels open, allowing potassium out of the cell (g_K increases).

3) Sodium channels are inactivated when the membrane voltage is at its highest ($g_{Na} = 0$).

4) Potassium channels close and sodium channels reactivate when the membrane voltage reaches its lowest ($g_K = 0$ and g_{Na} increases).

This means that the sodium and potassium conductances vary in a complicated way with changes in the membrane voltage. The "leak" current $\mathrm{I_l}$ is simply directly proportional to the membrane voltage,

$$\mathrm{I_l} = \bar{g}_l(V - V_l). \tag{2.2}$$

The changes in conductivity for the sodium and potassium channels are modelled as "gates". The gates are represented by a dimensionless variable, which can be between 1 (fully active) and 0 (fully inactive). The rate of change of a gate x with time is defined as

$$\frac{\mathrm{d}x}{\mathrm{d}t} = \alpha_x(1 - x) - \beta_x x, \tag{2.3}$$

where α_x is the rate of the gate transitioning from inactive to active, and β_x is the reverse.

Unlike the rest of the model's features, the gating of the ion channels is not worked out from first principles. Instead, equations were fitted to match empirical data from experiments. Hodgkin and Huxley took measurements of each ionic current separately, while keeping the membrane voltage constant, over a variety of different voltages, and used the data to find α and β expressions for each gate as functions of voltage.

For the potassium channel, there is only one type of gate, called the "n" gate. The permeability of the membrane to potassium varies with the 4th power of n,

$$\mathrm{I_K} = n^4 \bar{g}_K (V - V_K). \tag{2.4}$$

For the sodium channels, there are two types of gate. The m gate being active encourages flow of sodium ions through the membrane, but the h gate being active inactivates the sodium channels. $\mathrm{I_{Na}}$ is calculated

$$\mathrm{I_{Na}} = m^3 h \bar{g}_{Na} (V - V_{Na}). \tag{2.5}$$

With these equations, the characteristic action potential of the nerve cell could be recreated, as in Figure 2.5. The Hodgkin-Huxley model has formed the basis for much of modern computational neuroscience and cardiology (Catterall et al., 2012).

2.3.2 Noble's Purkinje cell model

The seminal Purkinje fibre cardiac cell model was published in 1960 by Denis Noble (Noble, 1960, 1962). A schematic of the model is shown in Figure 2.6. The sodium and leak currents in this model act in much the same way as in the original Hodgkin-Huxley formulation, with different rate constants. The potassium current is split into two components, which are modelled as rectifiers pointing in opposite directions. This means that the potassium ions flow easily into the membrane through the K1-type channels but not in the other direction, and potassium ions flow easily out of the cell through the K2-type channels, but not in the other direction. The two types of channel are active at different points during the cardiac cycle - the K1-type channels instantaneously become less active when the membrane is depolarised, and the K2-type channels become slowly more active when the membrane is depolarised. The K2 equation is gated in a similar way to Hodgkin and Huxley's potassium current n gate.

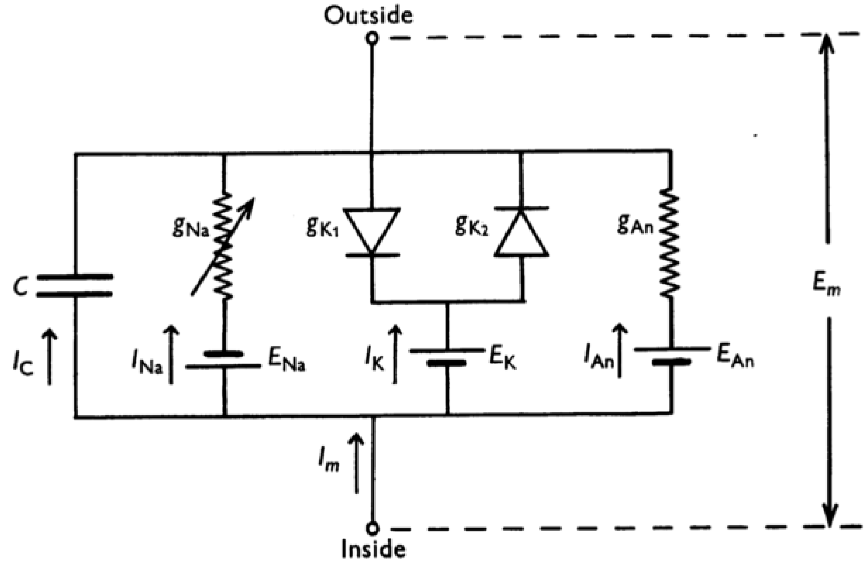

Figure 2.6: Diagram of the circuit from Noble's 1962 paper

The conductance of K1 is given by

$$g_{K_1} = 1.2e^{\frac{-E_m-90}{50}} + 0.0015e^{\frac{E_m+90}{60}}, \tag{2.6}$$

and the conductance of K2 is given by

$$g_{K_2} = 1.2n^4. \tag{2.7}$$

These equations recreated the characteristic action potential of a Purkinje cell, as shown in Figure 2.2.

2.3.3 Subsequent heart cell models

In the years since Noble's initial model was created, over a hundred cardiac cell models have been made, which use similar formulations for the behaviour of cardiac cells. Significant additions to the original model include the addition of the calcium subsystem, which was first introduced in the model created in 1975 by McAllister, Noble and Tsien (McAllister et al., 1975). This model added the calcium current I_{si} in the external membrane of the cell, as well as extra potassium currents.

The first model to allow change in the intracellular and extracellular concentrations of ions was created by DiFrancesco and Noble (1985). This model also included the sodium-calcium and sodium-potassium exchangers on the outer membrane of the cell, and a mixed, two-way current of sodium and potassium ions (the "funny" current, which is responsible for the slow depolarisation of pacemaker cells) (Lakatta et al., 2014). A schematic of this model can be found in Figure 2.7.

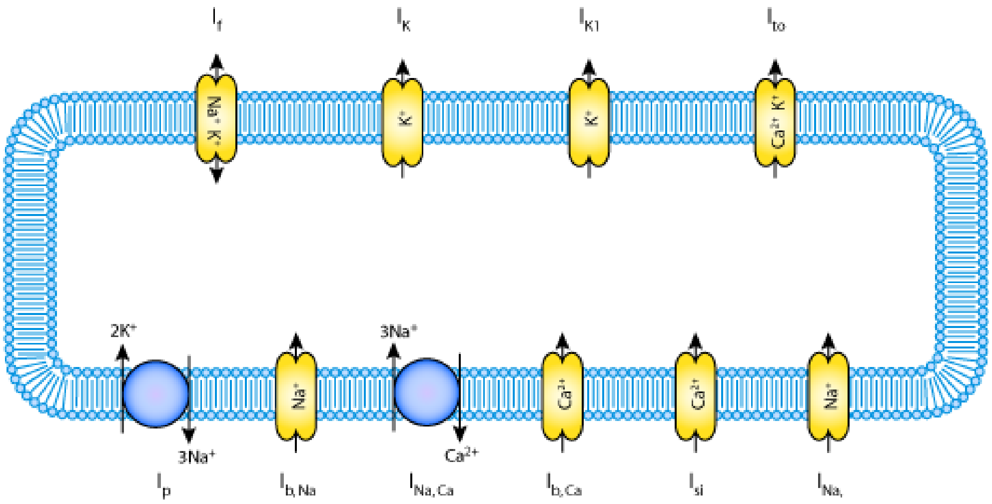

Figure 2.7: Schematic diagram of the DiFrancesco and Noble (1985) model from the CellML model repository. The currents included are the "funny" current I_F, the I_K, I_{K1} and I_{to} potassium currents, the I_{si} and $I_{b,Ca}$ calcium currents, the I_{Na} and $I_{b,Na}$ sodium currents and two exchangers: the sodium-potassium exchanger I_P and the sodium-calcium exchanger $I_{Na,Ca}$.

Recent models have included the calcium subsystem in great detail (including T-tubules, the sarcoplasmic reticulum, RyR, the sarco/endoplasmic reticulum calcium ATPase (SERCA) and calcium-induced calcium release, e.g. Luo and Rudy (1994)), as well as new formulations for ion channel gating based on Markov models, and mechano-electric feedback in the form of stretch-activated current (Weise et al., 2013).

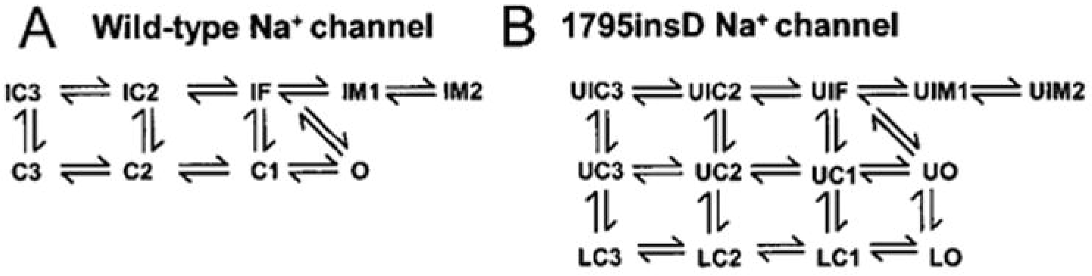

Figure 2.8: Schematic diagram of the Bennett et al. (1995) SCN5A Markov sodium current model. Left: the model for the wild-type current. Right: the modified model for an insertion mutant, 1795insD, which caused a form of LQT3.

In addition to the Hodgkin-Huxley style gating models described above, more recent cardiac cell models have used Markov models to represent ion currents. Bennett et al. (1995) created several Markov models to explain the behaviour caused by a mutation in the SCN5A sodium channel, that was causing a form of LQT3 by leaving a portion of the channels open during the plateau phase of the action potential. Clancy and Rudy (2002) developed the first cardiac cell model that used Markov models for the sodium current.

Since the early days of cardiac modelling, cell models have also been linked together to form 1-dimensional fibre models, and 2-dimensional tissue models, all of which have more recently been linked together to form whole-heart models, and even to extrapolate upwards to the whole human, recreating the signature shape of the electrocardiogram (Noble et al., 2012).

2.3.4 Human cardiac cell models

A number of human-specific electrophysiological cell models have been used for proarrhythmic risk prediction.

An early human cardiac cell model was the Priebe and Beuckelmann (1998) heart failure model.

Ten Tusscher 2006 model

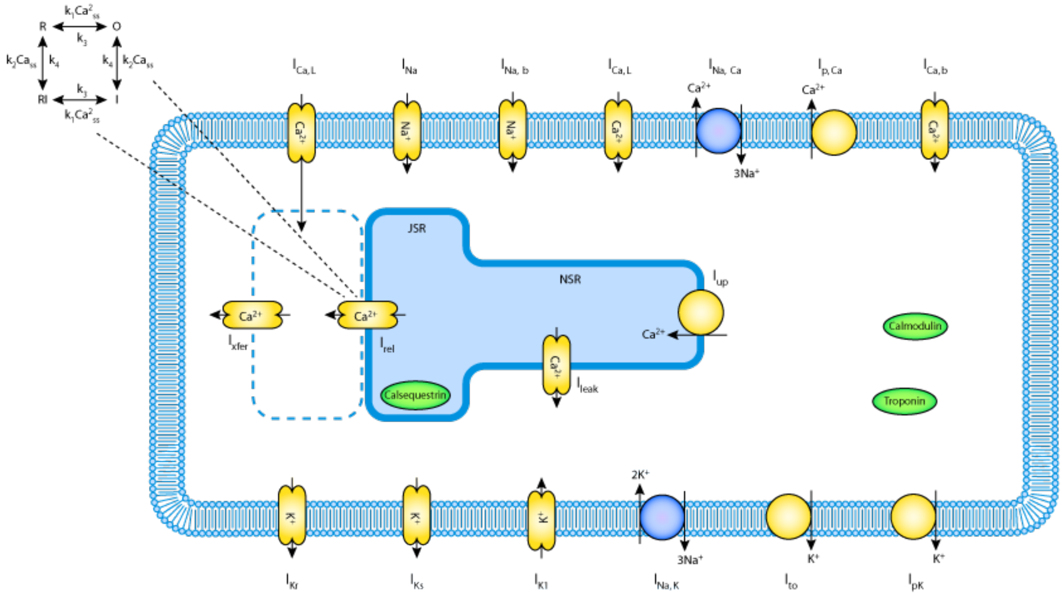

Figure 2.9: Schematic diagram of the ten Tusscher and Panfilov (2006) human ventricular myocyte model from the CellML model repository.

In ten Tusscher and Panfilov (2006), the previous ten Tusscher et al. (2003) model was extended with enhanced calcium dynamics in order to investigate alternans (alternating large and small action potentials) and re-entry. A compartment was added between the sarcoplasmic reticulum and the cell membrane. This diadic subspace is an area where the sarcoplasmic reticulum and cell membrane are particularly close together, meaning that changes in ion concentrations due to ion channels occur more rapidly than in the cell at large. The L-type calcium current was updated to inject calcium into the diadic subspace, and to be inactivated by subspace calcium concentration. The Hodgkin-Huxley style ryanodine receptor model was replaced with a Markov-style model with four states: open, inactivated (closed), resting (closed), and resting and inactivated (closed).

Grandi 2010 model

Grandi et al. (2010) used the structure of the earlier Shannon et al. (2004) rabbit myocyte model, and data from human ventricular myocytes to create a model for the human ventricular

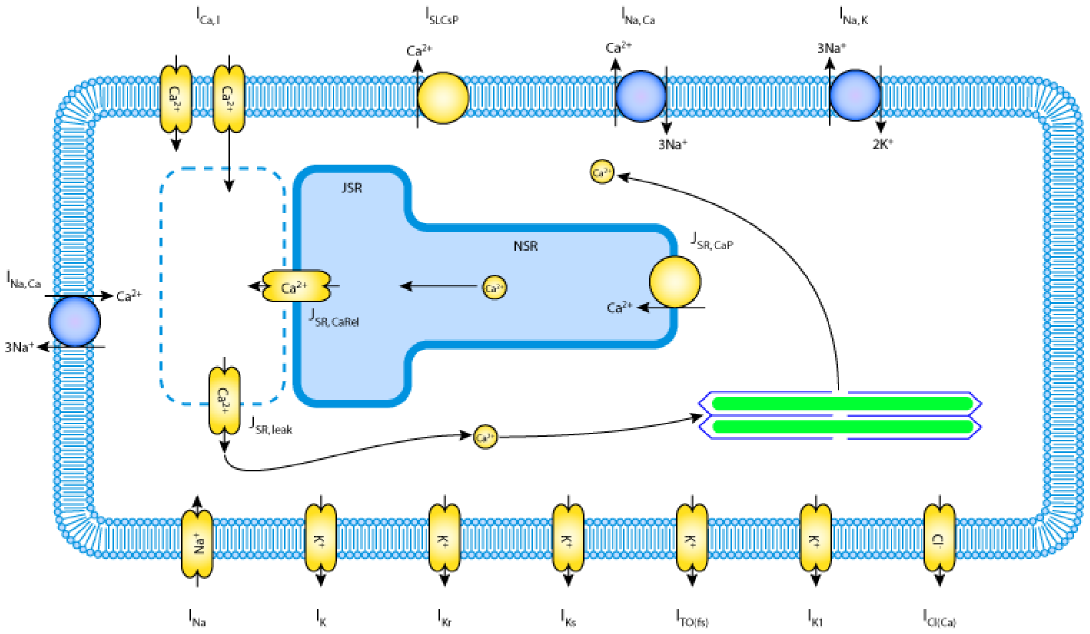

Figure 2.10: Schematic diagram of the Shannon et al. (2004) model from the CellML model repository, which has an identical structure to the Grandi et al. (2010) human ventricular myocyte model, with modified parameters.

myocyte. The Shannon et al. (2004) model structure was preserved, and the parameters were modified. Like the ten Tusscher and Panfilov (2006) model, the Shannon et al. (2004) model includes the sarcoplasmic reticulum, ion concentrations, calcium buffering, and a diadic subspace between the sarcoplasmic reticulum and the cell membrane.

O'Hara 2011 model

The O'Hara et al. (2011) model is a human ventricular myocyte model that is very widely used in proarrhythmia modelling (Cavero and Holzgrefe, 2015). The model is based on electrophysiological measurements from the endocardium of human hearts of both sexes. Epicardial and M cell models were also derived from the fully validated endocardial model, using transmural recordings.

The L-type calcium (I_{CaL}) current formulation was modified in this model to take into account calcium-dependent inactivation, which occurs when calcium ions bind to the protein calmodulin, which is associated with the L-type calcium channel. When four calcium ions bind to calmodulin, the channel is inactivated. The rate of binding of these ions depends on the concentration of calcium ions.

As with the three human models discussed previously, calcium buffering from calmodulin, troponin, and calsequestrin was implemented in this model. In addition, the serine-threonine kinase calmodulin-dependent kinase (CaMK) was simulated. CaMK is part of several signalling pathways, and is essential for rate adaption in the heart (Cavero and Holzgrefe, 2015). In this model, interactions between CaMK and several currents are simulated (See Figure 2.11), including the L-type calcium current, the fast and persistent sodium currents and the transient outward current. The late sodium current, which is of interest in proarrhythmia prediction due to its ability to counter the arrhythmic effects of hERG blockers, is included in this model.

Unlike the previous models, blocking the rapid delayed rectifier potassium current in the O'Hara et al. (2011) model can produce EADs, which matches the behaviour of human ventricular myocytes recorded by Guo et al. (2011).

The O'Hara et al. (2011) model has been used extensively in the prediction of pro-arrhythmic risk (Christophe, 2013; Passini et al., 2017; Li et al., 2020b).

2017 ORd-CiPA model

Dutta et al. (2017) created an updated version of the O'Hara et al. (2011) model in which the parameters were optimised to specifically recreate the effects of channel-blocking compounds on the action potential, based on novel experimental data. This model is known as ORd-CiPA and was developed to improve upon the gold-standard O'Hara et al. (2011) model for arrhythmia prediction. Dutta et al. (2017) is a re-parameterisation of the Li et al. (2017) model, which replaced the O'Hara et al. (2011) $\mathrm{I_{Kr}}$ formulation with a dynamic current that allows for simulation of drug binding kinetics.

The optimised model offered improvements over the original O'Hara et al. (2011) model in simulation of compound effects on action potential. The effects of $\mathrm{I_{CaL}}$ block or $\mathrm{I_{K1}}$ block on the rate dependence of APD were both less accurate in the Li et al. (2017) model than the O'Hara

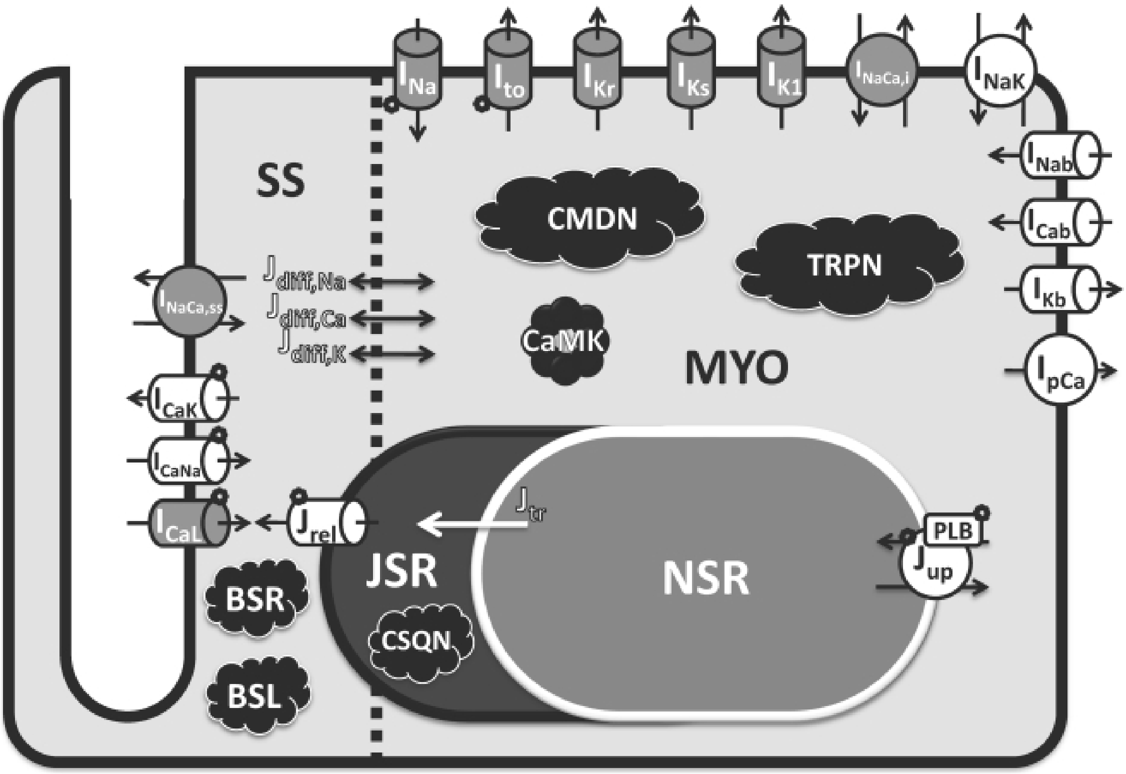

Figure 2.11: Schematic diagram of the O'Hara et al. (2011) model from the original paper. Included are the sarcoplasmic reticulum, a diadic subspace, calcium buffering, calmodulin-dependent kinase (CaMK), and ion currents and pumps. Targets of CaMK are denoted with a little flower.

et al. (2011), but the Dutta et al. (2017) optimised model improves on both of these. Similarly, the effects of $\mathrm{I_{NaL}}$ block or $\mathrm{I_{Kr}}$ block on the rate dependence of APD was more accurate in Dutta et al. (2017) than either O'Hara et al. (2011) or Li et al. (2017). Using the novel qNet metric for the prediction of proarrhythmic risk, the Dutta et al. (2017) model outperformed O'Hara et al. (2011) and Li et al. (2017) for classifying the 12 CiPA training compounds.

Subsequently, this model has been used for proarrhythmic risk prediction by Li et al. (2019) and Christophe and Crumb (2019).

2019 ToR-ORd model

The ToR-ORd model (Tomek et al., 2019) is an updated version of the O'Hara et al. (2011) model, designed and calibrated to overcome some of the discrepancies between the O'Hara et al. (2011) model and human experimental data, particularly in the currents required for excitation-contraction coupling, as well as including some mechanistically updated formulations for cellular components.

In the O'Hara et al. (2011) model, the voltage during the plateau stage of the action potential is higher than the voltage observed in experimental data from human cardiomyocytes. In addition, sodium block increases the amplitude of the calcium transient, in disagreement with experimental data. By simply changing the model's parameters without altering the structure, these discrepancies could not be removed.

In O'Hara et al. (2011), the L-type calcium current formulation uses a linear model for the driving force, based on the reversal potential. In Tomek et al. (2019), this current is updated to use the Goldman-Hodgkin-Katz equation for calculating the driving force and the activation curve. This formulation dynamically changes the driving force during the action potential based on the concentrations of ions on each side of the membrane. In addition, rather than being located entirely in the diadic subspace, 20% of the $\mathrm{I_{CaL}}$ current was moved to the cytosol.

The Hodgkin-Huxley $\mathrm{I_{Kr}}$ formulation from the O'Hara et al. (2011) model was replaced with a Markov model from Lu et al. (2001).

Two chloride currents, $\mathrm{I_{CaCl}}$ and $\mathrm{I_{Clb}}$, were added from the Grandi et al. (2010) human cell model, and the O'Hara et al. (2011) $\mathrm{I_{Na}}$ formulation was replaced by an updated version of the Grandi et al. (2010) I_{Na} formulation. The Carro et al. (2011) I_{K1} model was used to replace the O'Hara et al. (2011) I_{K1} current. The concentrations of intracellular chloride ions and extracellular potassium ions were also modified.

For each structural change to the model, parameter optimisation was performed to calibrate the conductances of the ionic currents and fluxes, the localisation of I_{NaCa}, and the rates of calcium release from the junctional sarcoplasmic reticulum.

Parameters were optimised for a set of criteria including morphology of the action potential and calcium transient, effects of 50% blockade of the I_{Na}, I_{NaL}, I_{ICaL} and I_{K1} currents, effects of rapid pacing, and conduction velocity in 1D fibre simulations.

EADs were induced by reducing I_{Kr} by 85% and pacing slowly at 0.25 Hz. Unlike the O'Hara et al. (2011) model, the Tomek et al. (2019) model displayed EADs with an amplitude and morphology that matched experimental recordings.

In a 1D fibre simulation in which the extracellular potassium concentration was increased to simulate hyperkalemia, the effective refractory period was elongated, the resting membrane potential was raised, and the action potential duration was reduced, in line with experimental data.

The Tomek et al. (2019) was used for torsadogenic risk prediction in Christophe (2022).

2.4 Conclusion

The vital function of the heart relies on the orderly and rhythmic action of electrically active cardiac cells , beginning with the pacemaker cells in the sinoatrial node and passing along through the atria, Bundle of His and Purkinje fibres before reaching the ventricles (Sherwood, 2004). The opening, closing, and inactivation of ion channels in the membranes of cardiomyocytes result in the characteristic voltage oscillations of the action potential - first, a sharp upstroke mediated by the fast sodium current, followed by an initial repolarisation by the transient outward potassium current, a plateau phase maintained by the depolarising L-type calcium and persistent sodium currents, then final repolarisation by the rectifier delayed potassium currents IKs and IKr. The resting membrane potential is then maintained by the inward rectifier potassium current IK1 and ionic concentrations are reset by the sodium potassium pump, sodium-calcium exchanger, and the sarco/endoplasmic reticulum calcium ATPase (Nerbonne, 2014; Rose and Backx, 2014; Noble, 2004; Brini and Carafoli, 2014). Contraction of myocytes is caused by the motor protein myosin walking along the structural actin filaments that traverse the cell, pulling the cytoskeleton towards the centre and shortening the cell. At rest, the binding sites on actin filaments are obscured by tropomyosin, but when calcium binds to this complex, it moves away from the site (Bers, 2014). The increase in intracellular calcium concentration during the action potential triggers calcium-induced calcium release from the sarcoplasmic reticulum, which couples excitation to contraction (Valdivia, 2014).

Modelling of excitable cells began with the Hodgkin and Huxley (1952) squid giant axon model, which included sodium, potassium, and leak currents, and was extended to Purkinje cells by Noble (1960), who split the potassium current into inward (IK1) and outward (IK2) rectifier currents. Subsequent models added calcium currents, (McAllister et al., 1975), ionic concentrations (DiFrancesco and Noble, 1985) and the calcium subsystem (Luo and Rudy, 1994), and there are several models designed specifically to model human cells, including ten Tusscher and Panfilov (2006), Grandi et al. (2010), O'Hara et al. (2011), Dutta et al. (2017), and Tomek et al. (2019). One application of the mathematical modelling of cardiac cells is the prediction of drug-induced arrhythmia based on the effects of ion current block, which is the subject of the next chapter.

Chapter 3

Literature review

Contents

In this chapter, I will describe the mechanisms behind Torsades de Pointes arrhythmia and the role of early afterdepolarisations, as well as the modelling and prediction of pro-arrhythmic risk.

3.1 Torsades de Pointes

First described by Dessertenne (1966), Torsades de Pointes is a particular type of polymorphic ventricular tachycardia, characterised by an unusual electrocardiogram, in which the QRS complex appears to be twisted around the baseline, reminiscent of the twisted columns in classical architectural motifs (Fabiato and Coumel, 1991). Torsades usually spontaneously resolves (Fabiato and Coumel, 1991), sometimes causing syncope, sudden fainting due to a drop in blood pressure, but can also cause cardiac arrest or sudden death (Schwartz et al., 2012).

The Long QT syndromes (LTQS) are all associated with Torsades de Pointes arrhythmias, with sometimes fatal consequences. In LQTS, the interval between the beginning of the Q wave and the end of the T wave on the electrocardiogram is increased. As of 2012, 10% to 12% of LQTS cases first manifested clinically as sudden death (Schwartz et al., 2012). Fatal Torsades can also be caused by various medications (Yap and Camm, 2003), including quinidine, terfenadine, cisapride, and sotalol.

Quinidine is the oldest class I anti-arrhythmic, and is used for preventing atrial and ventricular arrhythmias in various conditions, including Short QT syndrome and Brugada syndrome. Cases of syncope caused by quinidine have been reported since the 1920s, but it was only conclusively shown to cause ventricular tachycardia by Selzer and Wray (1964). Quinidine blocks multiple ion channels, including the sodium channels and the hERG potassium channels (Wu et al., 2008). A number of other anti-arrhythmics, including dofetilide and amiodarone, are also known to cause Torsades.

Terfenadine, a non-sedating anti-histamine, was one of the first non-cardiac drugs to be found to cause Torsades (Woosley et al., 1993). Terfenadine was withdrawn from the market in 1997 after being linked to 41 cases of Torsades, one of which was lethal (for a review, see Bryan (2011)).

Cisapride is a drug that was used for treating gastroesophageal reflux disease (Rampe et al., 1997). After causing 97 cases of Torsades, of which six were fatal, cisapride was withdrawn from the market (Redfern et al., 2003).

Sotalol, a Class III anti-arrhythmic, caused 130 cases of Torsades between 1983 and 1999 (Redfern et al., 2003). However, it is still prescribed today for arrhythmia prevention in patients with structural heart disease (Schleifer et al., 2015).

Drug-induced Torsades is more likely in patients with impaired renal function, congestive heart failure, or sustained ventricular tachycardia (Yap and Camm, 2003). In the case of terfenadine, drugs or other substances (including grapefruit juice) which caused increased blood levels of terfenadine increased Torsades risk (Woosley et al., 1993). Female sex is also a risk factor for the development of drug-induced Torsades: Makkar et al. (1993) examined previous cases of drug-induced Torsades by searching through reports of cases of polymorphic ventricular tachycardia in patients who had taken known torsadogenic drugs (quinidine, procainamide, disopyramide, amiodarone, sotalol, bepridil, and prenylamine). Women comprised 70% of these cases, and thorough examination of the data supported the hypothesis that female sex was a risk factor for developing Torsades when taking drugs which prolong repolarisation.

Although the LQTS all carry an increased risk of Torsades, and drugs which cause Torsades tend to also increase the QT interval, QT prolongation is not necessarily indicative of torsadogenic risk (Sager, 2008). Drugs which block multiple ion channels, such as amiodarone, ranolazine, and sodium pentobarbital, prolong the QT interval, but are not associated with Torsades.

3.2 hERG block: a sensitive but not specific predictor

The human ether-a-go-go-related gene (hERG) is of particular interest in drug-induced Torsades. hERG was first linked to Torsades via LQT2, one of the Long QT syndromes, by Curran et al. (1995). In this paper, the researchers showed that LQT2 was often inherited together with genetic markers found in one location on chromosome 7, indicating that this was LQT2's genetic location (this arduous pre-genomics-era method of locating genes is called "linkage analysis"). The hERG gene had recently been discovered and was thought, based on homology, to encode a potassium channel (Warmke and Ganetzky, 1994). Curran et al. (1995) showed, by fluorescent in situ hybridisation and linkage analysis, that hERG was located at the same place on chromosome 7 as LQT2. In addition to the gene's location, hERG was shown to be highly expressed in the heart in comparison to other tissues. The different hERG mutations found in LQT2 patients were sequenced and analysed. Mutations affected, by truncation and missense mutations, the transmembrane and pore-forming domains of the predicted protein, including one conserved amino acid known to confer potassium sensitivity to the channel.

After this, the hERG channel, and the rapid delayed rectifier potassium current (I_{Kr}) which flows through it, became of interest in the study of drug-induced Torsades. Po et al. (1999) expressed the hERG gene in Xenopus oocytes and mouse cells, and used whole cell patch clamp and the two-electrode voltage clamp to investigate the effect of quinidine on the hERG current. Quinidine was found to strongly block I_{Kr}.

Woosley et al. (1993) set out to establish whether the torsadogenic effects of terfenadine were caused by terfenadine or by its metabolite, terfenadine carboxylate, as adverse events had been reported in patients with high blood levels of terfenadine, either through overdose or from impaired metabolic function. It was established that terfenadine, and not its metabolite, blocked I_{Kr}, and as such was the likely suspect for torsadogenicity.

Rampe et al. (1997) expressed the hERG gene in human embryonic kidney cells and examined the effects of cisapride on its current using whole cell patch clamping. Cisapride was found to block I_{Kr} with high affinity.

Since these discoveries, testing for hERG block has become a mandatory requirement for new pharmaceuticals (European Medicines Agency, 2005). While this measure of torsadogenicity is very sensitive and has prevented torsadogenic drugs from coming onto the market, there are concerns that it lacks specificity, preventing the release of potentially useful drugs. Certain drugs on the market, such as verapamil and ranolazine, block hERG but aren't linked with Torsades (Kramer et al., 2013). As such, elucidation of other causes of Torsades is needed.

3.3 Multi-channel effects and Torsades

Antzelevitch et al. (2004) investigated the anti-anginal drug ranolazine. Ranolazine is particularly interesting in the study of drug-induced Torsades, because it blocks the potassium current carried by hERG, but is not associated with torsadogenic risk. In this paper, ranolazine was not found to cause EADs at any concentration, even when combined with EAD-promoting conditions such as bradycardia and hypokalaemia. Ranolazine was established to block I_{Kr}, late I_{Na} and I_{CaL}, to suppress sotalol-induced afterdepolarizations in canine ventricular myocytes, and to reduce transmural dispersion of repolarisation (TDR). The authors believed late I_{Na} block to be the key to the reduction in TDR, causing differential effects in different cell types depending on the levels of I_{Na} in the cell, thus prolonging epicardial action potentials while reducing those of Purkinje fibres and M cells. Ranolazine had previously been used as an anti-anginal drug, but analysis of its effects in Torsades pointed towards its use as an anti-arrhythmic.

The first human trial of ranolazine as an anti-arrhythmic agent was reported by Scirica et al. (2007), who gave it to a cohort of patients hospitalised with non-ST-elevation acute coronary syndrome – a condition in which reduced blood flow through the coronary arteries prevents part of the heart from functioning, but does not elevate the ST segment of the electrocardiogram. These patients are particularly at risk of cardiac arrhythmias. It was found that ranolazine treatment significantly reduced ventricular tachycardia, supraventricular tachycardia, and atrial fibrillation.

Undrovinas et al. (2006) used a canine model of heart failure to investigate the effects of ranolazine on abnormal repolarization and contraction. Failing hearts are susceptible to Torsades de Pointes arrhythmias, and as such could give mechanistic insight into the onset of drug-induced Torsades. In failing ventricular myocytes, ranolazine reduced APD, beat-to-beat variability, the appearance of EADs, and APD dispersion, and was shown to preferentially block the late portion of the sodium current. Ranolazine also reduced the incidence of small "twitch" contractions.

Another paper to focus on ranolazine is Song et al. (2006), who investigated the effects of late sodium block on the arrhythmogenic effects of hydrogen peroxide (H_2O_2), based on the hypothesis that H_2O_2 acts by increasing the late sodium current. H_2O_2, which is increased during heart failure, is thought to increase intracellular sodium, causing an increase in intracellular calcium by the action of the sodium-calcium exchanger. This calcium overload then causes afterdepolarisations by causing calcium-induced calcium release. Tetrodotoxin, which blocks the sodium current, and ranolazine, which preferentially blocks late sodium, were both shown to suppress H_2O_2-induced EADs in guinea pig and rat isolated ventricular myocytes, and to reduce the increase in intracellular sodium and calcium caused by H_2O_2. Late sodium current was shown to be heightened in cells treated with H_2O_2, giving evidence to support the hypothesis that H_2O_2's mechanism of action is to increase late sodium, thus causing sodium and therefore calcium overload of the cell.

There are several other Long QT syndromes that do not result from mutations that affect

$\mathrm{I_{Kr}}$, such as LQT1 in which the $\mathrm{I_{Ks}}$ current is decreased (Shimizu and Antzelevitch, 1998), or LQT3 in which the late sodium current is increased (Shimizu and Antzelevitch, 1997). These could point to factors other than hERG that are involved in drug-induced Torsades.

Noting that adverse cardiac events such as Torsades in patients with LQT1 were often associated with situations that increased adrenaline, such as physical or emotional stress, Shimizu and Antzelevitch (1998) investigated the effects of β adrenergic agonists, which increase the effect of adrenaline on the heart. LQT1 reduces $\mathrm{I_{Ks}}$, so Chromanol 293B was used to block this current to create a model of LQT1 in the canine ventricular wedge. This increased the action potential duration and QT interval, but didn't cause Torsades or increase the difference between action potential durations across the width of the ventricular wall (this pro-arrhythmic effect is called transmural dispersion of repolarization, or TDR). The addition of isoproterenol, a β adrenergic agonist, caused spontaneous Torsades and increased TDR in this system, showing that increased adrenaline response was torsadogenic. Treatment with propranolol, a β adrenergic antagonist, completely abrogated the effects of isoproterenol.

Shimizu and Antzelevitch (1997) used ATX-II to mimic the plateau phase sodium current of LQT3, in a canine ventricular wedge. The sodium blocker mexiletine was effective at suppressing Torsades in this model. Interestingly, they also created a model of LQT2 by using the hERG blocker sotalol, and found that mexiletine also prevented Torsades in this model, indicating that late sodium block could counteract the effects of hERG block.

Block of the hERG cardiac potassium current (I_{Kr}) has previously been used as a marker for predicting risk of TdP (European Medicines Agency, 2005). The hERG safety factor is calculated using the ratio of hERG $\mathrm{IC_{50}}$ to the effective free therapeutic plasma concentration (EFTPC) ($\log_{10}(\mathrm{hERG\ IC_{50}/EFTPC_{max}})$) (Redfern et al., 2003). However, not all drugs that block hERG - such as verapamil and ranolazine - are linked to TdP, possibly because they also block other ion currents (Milberg and Haverkamp, 2005; Cobbe, 2004). This means that, while hERG block is a very sensitive metric for predicting TdP risk (i.e. it gives very few false negatives), it lacks specificity, meaning that useful drugs may be prevented from making it to the market (Stockbridge et al., 2013).

3.4 Early afterdepolarisations and Torsades

The existence of early afterdepolarisations was first discovered by Segers (1941), who, after studying triggered tachycardia, recorded action potentials from frog ventricles treated with various agents, showing early and delayed afterdepolarisations. Segers used a number of methods for inducing afterdepolarisations, including adding barium, which is now known to act by inhibiting I_{K1} and increasing I_{CaL} (Hiraoka et al., 1980), aconite and veratridine, which both block inactivation of the fast sodium channel (Kelly, 1990; Hiraoka et al., 1992), and strophanthin and digitalis, which inactivate the sodium-potassium exchanger (Stern et al., 1992; Katz, 1985). Afterdepolarisations were suppressed by increasing extracellular potassium concentration or using acetylcholine, which opens the I_{KACh} potassium channels. Segers' recordings were measured using the monophasic action potential, a technique which measures the voltage between two sections of myocardium, one of which has been inactivated with KCl (Patterson et al., 1991). The first recordings of EADs using intracellular action potentials was by W. Trautwein et al. (1954), who subjected canine Purkinje fibres to hypoxic conditions for 45 minutes, then recorded single and double early afterdepolarisations. The term "early afterdepolarisation" was first coined by Cranefield (1977) to describe this phenomenon.

3.4.1 EADs at the tissue level

EADs can be directly observed in human hearts during Torsades de Pointes arrhythmia (Li et al., 2020a), but the mechanisms by which single-cell repolarisation abnormalities are causally linked to heart-level effects are not fully understood. Several mechanisms have been proposed: regional synchronisation of patches of cells causing focal activity; spiral wave break-up caused by EADs; and facilitation of re-entry by EADs. Many factors can affect the way EADs interact with tissue-level phenomena, including the level of heterogeneity between regions, the size of the affected area, and the method by which EADs are provoked.

Synchronisation of patches of EADs

Vandersickel et al. (2016) used the ten Tusscher and Panfilov (2006) human cell model in a 3D model of human ventricles to investigate the effects of the magnitude of the heterogeneity of the tissue on arrhythmic activity. EADs in patches of tissue were provoked by simulating reduced repolarisation reserve by reducing I_{Ks} and I_{Kr}, and increasing in I_{CaL}. When the heterogeneity was large, cells had synchronised EADs, and these caused focal activity. Ectopic sites that arose from different regions which had lower repolarisation reserve could alternate, which caused an ECG that resembled TdP. When the heterogeneity was small, the EADs instead facilitated re-entry.

Synchronisation of EADs in whole rabbit ventricles was investigated by Sato et al. (2009), using the Mahajan et al. (2008) rabbit cell model. EADs were provoked by simulating application of H_2O_2. The EADs that were provoked were found to synchronise with neighbouring tissue in small patches, but as the size of the tissue increased, a gradient in action potential duration developed and the EADs no longer synchronised. This regional synchronisation in the chaotic EADs led to re-entry, causing premature ventricular contractions (PVCs). Shifting in the PVCs caused polymorphic tachycardia and fibrillation.

Huffaker et al. (2007) found that in homogeneous tissue, heterogeneity in repolarisation reserve was created by re-entry. They performed simulations in 1D, 2D and 3D, using a modified version of the Luo-Rudy guinea pig model, with increased probability of sarcoplasmic reticulum calcium release. This heterogeneity led to the formation of regions of synchronised EADs. These regions created new single or double wavefronts, causing rapid relocation of rotors, which can replicate the ECG patterns seen in Torsades de Pointes. EADs also caused spiral wave breakup and focal activity.

The Mahajan et al. (2008) model was used by Xie et al. (2010) to study the effects of fibrosis and reduced conduction velocity on the number of synchronised cells having EADs required to cause automaticity. The model was modified to add a Markov model of I_{CaL} to simulate the effects of isoproterenol, as well as increasing I_{NaL}, increasing sarcoplasmic reticulum calcium uptake, and increasing the I_{NaK} current. The number of synchronised cells required for focal activity increased with dimension, and decreased when fibrosis, heart failure, reduced repolarisation reserve, or poor coupling were added.

Effect of type of EADs on tissue-level behaviour

Vandersickel et al. (2014) investigated the effects of EADs on 2D spatial patterns in human cardiac tissue, and found that EADs could occur during normal wave propagation without the need for tissue heterogeneity. The ten Tusscher and Panfilov (2006) model was modified to show reduced repolarisation reserve by reducing $\mathrm{I_{Kr}}$ and increasing $\mathrm{I_{CaL}}$, and the parameter regions that caused EADs were found. At a combination of lower values of $\mathrm{I_{Kr}}$ and higher values of $\mathrm{I_{CaL}}$, single or multiple EADs were seen. At the lowest values of $\mathrm{I_{Kr}}$ and highest values of $\mathrm{I_{CaL}}$, oscillating EADs were seen. Reactivation of $\mathrm{I_{CaL}}$ was found to be the mechanism by which EADs occurred. Waves of excitation were induced using initial point stimulation and an S1S2 protocol. The different types of EADs found were associated with different 2D patterns at the tissue level - cells showing oscillating EADs caused oscillatory waves in the tissue, and cells showing single or few EADs caused spiral wave breaks. Oscillatory patterns were mediated by calcium waves. There were two types of spiral waves observed. Type A spiral waves appeared small and chaotic, occurred in the same parameter regions where single or multiple EADs can be seen in single cells, and were mediated by calcium waves. Type B spiral waves were only provoked by the S1S2 stimulation protocol, occurred in the parameter region at the boundary between single cells experiencing EADs and not, and were mediated by sodium waves. In Van Nieuwenhuyse et al. (2017), the ten Tusscher and Panfilov (2006) model was used in a homogeneous 3D model of the human ventricles. As in the 2D model, EADs induced by simulating reduced repolarisation reserve caused spiral wave break-up or oscillatory patterns, corresponding in the same way to the types of EADs seen in single cells. However, when ECGs from these patterns were analysed, TdP style patterns were not seen - rather, the A type spiral waves showed ECG activity similar to ventricular fibrillation, and the B type showed ventricular tachycardia. The oscillatory behaviour led to an ECG pattern that did not resemble reality. A meandering spiral pattern followed by spiral wave break-up was seen when using the S1S2 protocol with a modest level of reduced repolarisation reserve. This pattern did cause a TdP-like ECG.

Dutta et al. (2016) used a human cell model (ten Tusscher and Panfilov, 2006) to construct a model of the human ventricle with an ischaemic region. They were able to show that EADs can be triggered by an injury current flowing from the border zone of the ischaemic region, as long as the cells were in a state of reduced repolarisation reserve caused by 50% block of $\mathrm{I_{Kr}}$. However, reducing $\mathrm{I_{Kr}}$ by 30% inhibited re-entry. When ectopic stimulation was applied, the presence of electrotonically-triggered EADs caused the wave of excitation to re-enter transmurally.

In de Lange et al. (2012), the modified Mahajan et al. (2008) model was used in heterogeneous 1D and 2D tissue to investigate the effects of different types of EADs on tissue-level behaviour. Phase 2 EADs were found to be unable to propagate in normal, well-coupled tissue - however, patches of cells were able to synchronise and cause dispersion of refractoriness across the tissue. Phase 3 EADs could both propagate and synchronise. EADs propagated via reactivation of either I_{CaL} or I_{Na}. The presence of chaotic EADs forming in heterogeneous tissue caused multiple shifting foci of premature ventricular complexes, which could spontaneously terminate or promote re-entry.

Tissue from rat hearts was used alongside *in silico* simulation of the Mahajan et al. (2008) model in Chang et al. (2012) to investigate the propagation of EADs in 2D tissue. Propagation mediated by reactivation of both I_{CaL} and I_{Na} could be seen in the same tissue, and the PVCs thus caused in the simulation led to an ECG that resembled TdP.

In conclusion, large patches of cells with severely reduced repolarisation reserve compared to the surrounding tissue have been shown in the above simulation studies to synchronise and cause focal activity. However, smaller patches of cells, or simulations with smaller heterogeneity between the regions, are not able to cause focal activity, and instead promote re-entry. EAD propagation can also be seen in homogeneous tissue with reduced repolarisation reserve, where oscillating EADs cause oscillating waves. Single or multiple EADs induced in homogeneous tissue can cause spiral wave breakup. In hearts with an ischaemic region, an injury current flowing into the border zone can cause EADs, which then promote transmural re-entry.

3.4.2 Ionic mechanisms which cause EADs

There are several different ionic mechanisms found to be the cause of early afterdepolarisations in ventricular myocytes. While many different cellular conditions can provoke EADs, the appearance of a second spike in the action potential fundamentally requires a sufficient net flow of positive ions into the cell. Broadly, reactivation of either the L-type calcium or sodium channels, or the sodium-calcium exchanger have all been found to be responsible for the formation of EADs, sometimes in combination with calcium release from the sarcoplasmic reticulum or reduced repolarisation reserve (Wit, 2018). Repolarisation reserve is a term that refers to the balance of inward and outward currents during the cardiac cycle (Roden, 1998; Roden Dan M., 2008; Roden and Abraham, 2011). Without sufficient repolarising currents during the plateau phase, only a small increase in depolarising currents is required to cause an EAD. As such, in cells with reduced repolarisation reserve - which can be due to mutations in ion channel genes, ion channel density, ionic imbalances, or drug effects - EADs can be induced more easily.

January and Riddle (1989) gave two key insights into the cellular mechanism behind EADs: firstly, that EADs were dependent on a transient inward current, and secondly, that this current was carried through the L-type calcium channels. They used Bay K 8644, a calcium channel agonist and structural analogue of the calcium channel blocker nifedipine (Thomas et al., 1985) to examine the formation of EADs in sheep Purkinje fibres. They used two voltage protocols: one which elicited EADs, and one which elicited an inward current transient. Both protocols began with a depolarizing step from the resting potential, and then a conditioning step to voltages near the plateau voltage. For the EAD experiments, the voltage clamp was then released, so that an EAD could form. For the inward current transient experiments, a second depolarizing step was applied, and the current was measured. The length and voltage of the conditioning step was varied, and it was found that the conditioning time and voltages necessary to produce EADs were highly correlated with those required for production of the inward current transient, and moreover that the amplitude of both EADs and the current transient were related to conditioning time and voltage in the same way. The authors concluded that this was sufficient evidence to support the hypothesis that a transient inward current is necessary for EAD induction. To investigate the constitution of the inward current transient, tetrodotoxin was used to block the sodium channels. This had very little effect on the inward transient current produced under the 2-step voltage protocol. However, when nitrendipine, the calcium channel blocker, was applied, the inward current transient was completely abolished, leaving only outward currents. This rules out the sodium channels as carriers of the inward current transient. To rule out the Na-Ca exchanger, the cells were placed in a sodium-free environment, meaning that the exchanger could not function, and this did not affect the inward current transient. These results, taken together, show that the L-type calcium channels are the carriers of this transient inward current. This paper has been cited by several other of the most influential papers about EADs, including in Curran et al. (1995), in which it is used to support the conclusion that delayed repolarisation due to hERG mutations could cause EADs by allowing the L-type calcium channels to reactivate. Key papers about the action of terfenadine (Woosley et al., 1993) and the cellular basis for LQT3 (Shimizu and Antzelevitch, 1998) also build on this important paper.

Sicouri and Antzelevitch (1991) discuss a putative population of subepicardial cells from the canine ventricle, termed M-cells, which the authors considered to have distinct electrophysiological characteristics from epi- and endocardial cells. The repolarization of these cells was thought to be particularly dependent on I_{Kr}, and EADs were elicited using relatively low concentrations of the potassium channel blockers quinidine, clofilium, cesium, 4-AP, and amiloride. Antzelevitch was also an author of two influential papers: Antzelevitch et al. (2004), and Shimizu and Antzelevitch (1997), which investigate the anti-arrhythmic properties of ranolazine and mexiletine, respectively. In both of these papers, the effects of these drugs on M cells is discussed as an important factor in the onset of ventricular arrhythmias. However, there remains controversy over whether M cells are present or important in the human myocardium (Janse et al., 2011).

There are several examples of L-type calcium reactivation causing EADs in *in vitro* models. Liu et al. (2012) found that in Langendorff perfused whole heart, isolated ventricular myocytes from rabbit models of LQT1, and the Luo and Rudy (1994) computational model, EADs that were initiated by isoprenaline were associated with an increase in L-type calcium current activation speed. Zhao et al. (2012) also used *in vitro* isolated ventricular rabbit myocytes to show that EADs induced by oxidative stress are caused by the same mechanism. Similarly, Chang et al. (2013) showed that block of the apamin-sensitive potassium current in *in vitro* Langendorff perfused hearts from rabbit models of heart failure causes EADs that can be abrogated by using the calcium current blocker nifedipine. These experimental studies show that the L-type calcium current can be the ultimate mechanistic basis for EADs caused by multiple different provocation methods.

Fomby and Cherlin (2011) investigated the late sodium current in ventricular myocytes from human and canine failing hearts. In comparison to non-failing hearts, myocytes from failing hearts showed more EADs, and had higher levels of late sodium, which caused a larger total sodium influx into the cell. Reducing the late sodium current or addition of an opposite current eliminated the afterdepolarisations. This implies that increased late sodium current is a cause of EADs in failing hearts.

In Aiba et al. (2009), a dog model of dyssynchronous heart failure was created using ablation. This increased EADs in isolated ventricular myocytes from these animals. The dogs then underwent cardiac resynchronisation therapy, in which both ventricles are paced at the same rate, and this decreased EADs. The calcium transient was prolonged in the heart failure model, and reduced by resynchronisation. Potassium currents were also downregulated in the heart failure model. $\mathrm{I_{Ks}}$, $\mathrm{I_{Kr}}$ and $\mathrm{I_{K1}}$ were partially restored by resynchronisation, but $\mathrm{I_{to}}$ was not.

After the work of Song et al. (2006), Xie et al. (2009) used rabbit ventricular myocytes to investigate the effects of H_2O_2 on EAD formation. In addition to the increase in $\mathrm{I_{NaL}}$ that has been noted previously, the L-type calcium current was increased, and its inactivation was impaired. Block of CAMKII delayed the appearance of EADs, suggesting that CAMKII was one mechanism by which $\mathrm{I_{CaL}}$ and $\mathrm{I_{NaL}}$ were increased.

L-type calcium reactivation has also found to be the cause of EADs in *in silico* studies. Sridhar et al. (2017) coupled a human ventricular myocyte model (ten Tusscher and Panfilov, 2006) to simulated fibroblasts, and used a combination of L-type calcium current conductance increase and hERG potassium current block to induce EADs. In Kurata et al. (2017) and Kurata et al. (2020), various human ventricular myocyte models (including O'Hara et al. (2011), Grandi et al. (2010), and variations on ten Tusscher and Panfilov (2006)) were modified to simulate LQT1 and LQT2. EADs induced in the LQT1 model by simulating beta-adrenergic stimulation were driven by the L-type calcium current. By simulating human hypertrophic cardiomyopathy in a population of human ventricular myocyte models, Passini et al. (2016) were able to determine that L-type calcium current reactivation was the main driver for EADs caused by these changes.

Failure of deactivation, rather than aberrant reactivation, of the L-type calcium current was found by Yamada et al. (2008) to be an important cause of EADs provoked by $\mathrm{I_{Ks}}$ and $\mathrm{I_{Kr}}$ blockers in isolated rabbit ventricular cells.

Reactivation of the sodium channels has also been implicated in EAD formation. In Sato et al. (2017), direct initiation of EADs by reactivation of the fast sodium current was found in an *in silico* rabbit ventricular myocyte model when the activation and inactivation curves of the fast sodium current were changed to increase the window current. In a Langendorff perfused whole heart *in vitro* rabbit model of atrioventricular block, Farkas et al. (2009) found that drugs such as lidocaine, which blocks the fast sodium current, and verapamil, which blocks the

L-type calcium current, could prevent TdP provoked by blocking the hERG potassium current. Van Nieuwenhuyse et al. (2017) performed a whole-ventricle simulation using a human ventricular myocyte model (ten Tusscher and Panfilov, 2006) and found that EADs provoked by a combination of L-type calcium conductance increase and hERG potassium current block were caused by combinations of sodium and calcium current reactivation.

Release of calcium from the sarcoplasmic reticulum is also known to trigger EADs. One hypothesised mechanism for this process is that the sodium-calcium exchanger $\mathrm{I_{NCX}}$ is reactivated by the increased calcium concentration in the cell (Zhao et al., 2012). Zhao et al. (2012) caused calcium overload in isolated ventricular rabbit myocytes by treating them with Bay K, a calcium channel agonist, and isoproterinol, a beta-adrenergic agonist. Unlike EADs precipitated by oxidative stress, EADs provoked by calcium overload were attenuated by ryanodine receptor block, showing that calcium release from the sarcoplasmic reticulum was a key mechanism for EAD formation. In Kurata et al. (2020), spontaneous sarcoplasmic reticulum calcium release-induced EADs that involved reactivation of the sodium-calcium exchanger were observed when the human ventricular single cell ten Tusscher and Panfilov (2006) *in silico* model was modified to increase calcium uptake into the sarcoplasmic reticulum.

Patterson et al. (2006) proposed a mechanism for EADs in pulmonary veins which doesn't involve $\mathrm{I_{CaL}}$ reactivation. The atrial myocardium extends into the pulmonary veins (PVs) and vice versa, and atrial fibrillation can be initiated by focal excitation in these PV myocytes. This focal activity was thought to be caused by EADs. PV myocytes have a particularly short action potential duration, suggesting that EAD formation must have a different mechanism in these cells than in those with prolonged action potentials, like those studied by January and Riddle (1989). Experiments using canine PVs showed that enhancing the inwards action of the sodium-calcium exchanger (NCX) increased the incidence of EADs, and that adding ryanodine prevented EADs. The suggested mechanism for EADs in PV myocytes was that the normal transient occurs later in the action potential, due to the short APD. This increases the intracellular calcium concentration, which activates the inward mode of NCX, which depolarises the cell.

As well as mathematical models, stem cell models of EADs are also available, which can be used to elucidate the mechanisms behind drug-induced Torsades. Liang et al. (2013) used human induced pluripotent stem cell-derived cardiomyocytes to model several disease states for the purposes of drug testing: LQT1, hypertrophic cardiomyopathy (HCM), and familial dilated cardiomyopathy (DCM). These patient-specific cells were used to screen a library of compounds with known torsadogenic risk: cisapride, nicorandil, alfuzosin and verapamil. APD prolongation and EADs were measured using whole-cell patch clamp. Cisapride, a particularly torsadogenic drug, prolonged the action potentials and caused EADs in all cell lines. The threshold concentration of cisapride necessary for these effects was lower in the LQT1 and HCM cell lines than in the control. However, the threshold was not lower for the DCM cells. LQT1 and HCM cells showed some EADs and delayed afterdepolarisations (DADs) even with no intervention, and DCM cells did not, suggesting that this difference is due to cisapride aggravating an existing arrhythmia. Nicorandil, which is a potassium channel agonist, decreased APDs in all cell lines. In the LQT1 cell line, nicorandil abolished spontaneous EADs. All cell lines showed QT shortening on treatment with nicorandil. Verapamil and alfuzosin were only used on the control cells, and each caused APD prolongation but not EADs.

Previous studies have investigated the formation of EADs in stem cell-derived cardiomyocytes as a measure of how adult-like the cells are. He et al. (2003) used action potential recordings to classify the types of cardiomyocytes that form beating populations of cells in embryonic stem cell preparations, into nodal-like, ventricular-like, and atrial-like. E-4031, which blocks the hERG potassium channels, was used to elicit EADs in these cells. The onset of afterdepolarisations, the authors argue, requires the presence of the full set of ion channels and the calcium subsystem of adult cardiomyocytes. Ma et al. (2011) developed a high-throughput method for producing human-induced pluripotent stem cell-derived cardiomyocytes (hiPSC-CMs) in large numbers, and present in their paper an analysis of the electrophysiological characteristics of these cells, as observed using high-throughput automated patch-clamping. In response to I_{Kr} block using E4031, the cells displayed EADs that resembled those of canine Purkinje fibres.

In conclusion, several ionic mechanisms for the appearance for EADs have been presented in the literature. 1) The L-type calcium current is reactivated without SR calcium release. 2) The fast sodium current is reactivated, often in combination with the L-type calcium current. 3) Release of calcium from the sarcoplasmic reticulum causes reactivation of the sodium-calcium exchanger, L-type calcium current, or transient inward current.

3.4.3 Dynamical systems analysis of EADs

In dynamical systems analysis, the behaviour of a complex system - such as the systems of ODEs that comprise cardiac cell models - is analysed in response to changes in chosen input parameters (for an excellent overview, see Kurata et al. (2005) and Qu et al. (2013)). Features of the behaviour, such as bifurcations (qualitative changes in output based on input parameters), limit cycles (oscillatory behaviour), and equilibrium (steady-state) points, can then be discovered and attributed to regions in input parameter values. Hopf bifurcations, in which steady states become limit cycles, and homoclinic bifurcations, in which limit cycles turn into steady states, are commonly seen in the initiation and termination of EADs. Dynamical chaos, where small changes in input parameters cause large changes in the behaviour of the system, is also a feature of EADs.

Two principal methods have been used to analyse the provenance of EADs as a feature of dynamical systems: using a simplified version of a cell model with enormously reduced parameters, such as in Tran et al. (2009); or using an existing biophysically detailed cell model as in Kurata et al. (2020).

A simplified version of the Luo and Rudy (1994) model was developed by Tran et al. (2009) to study the dynamical mechanisms underlying the genesis and chaotic nature of EADs. In this model, the I_{Na} current was disregarded, as it is not active during the plateau phase. The calcium current I_{si} and the potassium current I_K were separated for slow-fast subsystem analysis, because they operate at different time scales. The conductance of the I_{si} current was increased to make EADs more likely. The gating variable of the I_K current (x) was set to different values, and the effect on the behaviour of the faster calcium subsystem was analysed. When x is small, i.e. when the I_K current is mostly inactive, the calcium subsystem has three steady states. As x increases, the upper steady state undergoes a Hopf bifurcation, and a limit cycle appears. When the time constants for the two I_{si} current gating variables are large (i.e. when activation and inactivation are slow), EADs are seen in the whole system, as the voltage and x values for the Hopf bifurcation are reached during the action potential. Conversely, when these time constants are small, no Hopf bifurcation is seen and EADs do not occur. Therefore, the authors concluded that a Hopf bifurcation is a necessary condition for the formation of EADs.

In real terms, this means that the system must go from a steady state to an oscillatory state. After further increasing x, the limit cycle is terminated with a homoclinic bifurcation, whereby the limit cycle becomes a steady state.

Tran et al. (2009) found that the initial value of x (x_0) at the beginning of the action potential has a strong effect on the action potential duration. APD for different values of x_0 are discontinuous depending on whether an EAD is formed, meaning that small changes in x_0 can cause very large changes in APD, i.e. that the system exhibits dynamical chaos. Different pacing cycle lengths can lead to different values of x_0, meaning that dynamical chaos can be induced.

Qu et al. (2013) used non-linear dynamical theory to explore why not all conditions and drugs that promote action potential duration prolongation cause EADs, by examining the relationship between a theoretical current I and the membrane voltage V. The authors discussed the need for a quasi-equilibrium state (called the p-state) for the current at the plateau voltage - i.e. $I = 0$ at a voltage other than at the resting membrane potential of the cell. Qu et al. (2013) looked at the quasi-steady states of the inward and outward currents as a whole at different values of x.

This means that if the membrane potential is close to the p-state - within an area called the "window region" - the membrane potential will oscillate around the p-state voltage rather than returning to the resting potential, causing EADs. In addition to a quasi-equilibrium state, the current in question must be active when the voltage is in the window region. This means that any "gates" on the current must not be closed or inactivated during the time when the voltage reaches the window region. The speed at which gates open and close is also vital to the production of EADs. A current with a steep steady-state activation curve will make oscillations around the p-state, and thus EADs, more probable. Increasing the window current of the L-type calcium channel (i.e. the overlap between the steady-state activation and inactivation curves) was found to promote quasi-equilibrium states, and thus EADs, at the plateau voltage. Similarly, reducing the window current eliminated EADs. $\mathrm{I_{Kr}}$ prevented EADs by opposing steady-state inward currents and preventing a quasi-equilibrium state at the plateau voltage. However, since $\mathrm{I_{Kr}}$ has a steeply sloped steady state activation curve, it may make the p-state less stable, increasing the probability that EADs will occur in the case of a prolonged action potential. In cell models with EADs, there exist the above three equilibrium values where the inward and outward currents are balanced, i.e. when there is a net membrane current of zero. When a Hopf bifurcation does not exist, e.g. when the highest equilibrium state is above the plateau voltage, the cell experiences APD prolongation, but not EADs.

In Kurata et al. (2005), a human ventricular myocyte model was created in order to examine the dynamical mechanisms of induced pacemaker activity. Tsumoto et al. (2017) discovered a bi-stable state when the $\mathrm{I_{Kr}}$ current conductance was reduced, depending on the intracellular sodium concentration, which varies during the action potential. This implies that within cells in tissue with homogeneously reduced $\mathrm{I_{Kr}}$ conductance, heterogeneities in the action potential can be created by time-dependent intracellular concentrations of ions.

Kurata et al. (2017) used both the Kurata et al. (2005) model and the O'Hara et al. (2011) model to attempt to replicate spontaneous sarcoplasmic reticulum calcium release-induced EADs. Neither model was able to replicate this phenomenon. However, in Kurata et al. (2020), the ten Tusscher and Panfilov (2006) model was able to show this type of EAD.

Kurata et al. (2020) used the ten Tusscher and Panfilov (2006) human ventricular myocyte model to investigate the dynamical mechanisms of EAD formation in LQT1 and LQT2, in particular the effects of spontaneous calcium release from the sarcoplasmic reticulum. Varying parameters such as $\mathrm{I_{CaL}}$ and $\mathrm{I_{Kr}}$ caused qualitative changes in the behaviour of the overall system - i.e. a Hopf bifurcation, a change in plateau membrane voltage from the steady state (normal action potentials) to an oscillatory state (EADs). Non-paced simulations were performed to investigate the formation of automaticity mediated by spontaneous calcium release. In the parameter space where repolarisation failure was found in the paced model, spontaneous voltage oscillations were seen in the non-paced model. This suggests that spontaneous calcium release from the sarcoplasmic reticulum can sustain EADs to cause spontaneous oscillation.

There are several different types of dynamical behaviour that can precipitate the formation and termination of EADs, but the most common form is a Hopf bifurcation, in which a steady state moves to an oscillatory state. Dynamical systems analysis of EADs has also shown that variation in intracellular ion concentrations and open states of ion currents over the course of the action potential can allow dynamical chaos to occur. This underlines the need in torsadogenic risk prediction for simulation of electrophysiological systems rather than just statistical methods based on drug-channel interactions, as the chaotic nature of these systems can lead to large changes in outputs caused by small changes in input parameters.

3.5 Prediction of drug-induced Torsades

The Comprehensive in-vitro Pro-arrhythmia Assay (CiPA) initiative aims to use screening for multi-ion channel effects in combination with the computational modelling of drug effects on myocytes to create an integrated method for specifically predicting TdP (Sager et al., 2014). In Li et al. (2020b) the state of the art in the CiPA initiative *in silico* field was described, and the principles of the framework were laid out.

- Principle 1: A defined end point consistent with the context of use. There are many different risk categorisation systems, and researchers should choose the system appropriate for the context. For example, QT prolongation prediction requires a different risk categorisation system than TdP prediction.

- Principle 2: An unambiguous algorithm. Experimental protocols and code must be explicit and published.

- Principle 3: A defined domain of applicability. The experimental protocols used to obtain data for model training should also be used for testing new compounds, and models should only be used to infer outcomes in a similar patient population to the one that the parameters were sourced from.

- Principle 4: A stringent strategy and predefined criteria to assess predictivity. The CiPA framework includes 12 training drugs and 16 validation drugs, and the predictivity of different approaches can be compared by calculating the accuracy of classification for the validation drugs when the training drugs are used to construct the model.

- Principle 5: A mechanistic interpretation rather than using machine learning or statistical models that go straight from drug parameters to risk categories. This gives more information as to likely mechanisms, increases trust in the model, and can be more useful in drug design.

- Principle 6: Appropriate uncertainty quantification. Sources of uncertainty include experimental measurements and inter-personal variability, and the way that this uncertainty propagates through models should be quantified.

Several different *in silico* metrics for the prediction of drug-induced pro-arrhythmic risk have been suggested. These metrics have ranged in scale from single cell to whole torso models, and have used model outputs including action potential duration, the presence or absence of repolarisation abnormalities such as EADs or repolarisation failure, the magnitude of currents during the action potential, and ionic concentrations. Input parameters into these simulations include drug block data in the form of IC50s and Hill coefficients, drug concentration measurements, and in some cases the dynamics of drug binding to the hERG channel.

In Mirams et al. (2011), the effects of multi-ion current block were simulated in human ventricular myocyte models and the action potential duration was used to separate drugs into discrete risk categories based on TdP incidence in humans. This method has also been used to accurately predict the results of the Thorough QT study and rabbit wedge experiments (Mirams et al., 2014; Beattie et al., 2013). In Christophe (2013), the drug concentration required to cause an EAD in a simulated cardiac cell was used as a risk indicator for TdP. Lancaster and Sobie (2016) developed a two-dimensional binary classification metric based on simulating both the APD50 and the diastolic calcium concentration, which was chosen by using principal component analysis to investigate a large number of biomarkers drawn from different models. Passini et al. (2017) used a population of models approach to represent the variability between humans, allowing for diversity in conductance parameters while maintaining a normal action potential, and variability in ion channel block measurements was also represented. For each compound, a “TdP score” was calculated from the proportion of the cell models in the population that showed repolarisation abnormalities such as early afterdepolarisations and failure to repolarise, proportional to the concentration of the drug relative to the $EFTPC_{max}$. This metric was able to predict TdP risk with very high accuracy. In Tomek et al. (2019), torsadogenic drug safety prediction was performed using a population of models approach as in Passini et al. (2017). The ToR-ORd model was less accurate and sensitive than the original ORd model, but it had higher specificity. Unlike the original ORd model, the ToR-ORd model correctly classified mexiletine as a non-torsadogenic drug. Mexiletine blocks sodium currents, and the authors concluded that this improvement in prediction was due to the improved representation of sodium blockers in this model.

Using the 12 drugs chosen as CiPA training compounds, Li et al. (2017) developed the cqInward metric, which is calculated using the total L-type calcium current and persistent sodium current during a single action potential. Li et al. (2017) updated the O'Hara Rudy (ORd) model to include a dynamic Markov model for the hERG (I_{Kr}) current rather than a Hodgkin-Huxley type model, allowing for enhanced representation of drug binding mechanisms and kinetics. Instead of using only the IC_{50} measurements for drugs of interest, in this model the more complex drug-channel interactions such as time-dependent and state-dependent dynamics of binding, can be investigated for their effects on torsadogenic risk. The parameters of the model were further optimised in Dutta et al. (2017) by scaling multiple ionic current conductances to reflect experimental results for APD rate dependence under conditions of ion channel block. In addition to model optimisation, the cqInward metric was also improved in this paper by including potassium currents into its calculation, creating the new qNet metric. In Li et al. (2019), the qNet metric was assessed using the 16 CiPA validation compounds, and found to be more accurate than the Mirams et al. (2011) APD90 metric or the Lancaster and Sobie (2016) APD50 and diastolic calcium concentration metric.

In Christophe and Crumb (2019), disease states including hypertrophic cardiomyopathy, heart failure, and cardiac pause were used in combination with increased drug concentration to elicit EADs for the prediction of arrhythmic risk, using the Dutta et al. (2017) model. The minimum change in voltage at the EAD take-off potential was used to predict the arrhythmic risk of compounds. The presence of a concomitant cardiac risk factor increased the probability of EADs occurring when torsadogenic drugs were applied to the cell model, and improved the accuracy of prediction. Subsequently, the Tomek et al. (2019) model was used by Christophe (2022) to predict torsadogenic risk by increasing drug concentration until an EAD was detected, and using this threshold to categorise 109 drugs by risk. Both the healthy and hypertrophic cardiomyopathy (HCM) variants of the model were used, and the HCM variant was found to be more accurate for risk prediction. Combining the EAD thresholds with the amplitude of calcium release from the junctional SR ($\mathrm{J_{rel}}$) at the EAD take-off voltage also improved the accuracy of the metric.

3.5.1 Methods for inducing EADs

Some biomarkers used as prediction metrics, such as APD90, can be calculated using the usual concentration of drugs (Mirams et al., 2011; Lancaster and Sobie, 2016; Li et al., 2019). However, for metrics which use the presence or absence of repolarisation abnormalities such as EADs as a predictive tool, EADs often cannot be elicited at this concentration. A popular method is to increase the concentration of the drug beyond the $\mathrm{EFTPC_{max}}$, up to 100-fold (Christophe, 2013; Passini et al., 2017). In this way, the effects of the drug on multiple ion currents are amplified, which mimics the effects of overdose or metabolic variability. Increased drug concentration can be combined with disease states in order to produce EADs, as in Christophe and Crumb (2019), or used with a heterogeneous population of cells as in Passini et al. (2017).

In order to provoke EADs in cardiac cell models at physiological concentrations of drugs, a further insult must be applied to the system. EADs can be produced by increasing the L-type calcium current, as in LQT8 or under the effect of calcium channel agonists (Kang et al., 2010), or by reducing the conductance of the $\mathrm{I_{Kr}}$ current, as in LQT2 or under the effect of medications (Curran et al., 1995).

Hearts with an ischaemic region are more prone to arrhythmias. A driving factor for arrhythmogenesis in this region is an injury current flowing from an ischaemic region to the border (Janse and Wit, 1989). This current has been shown to cause afterdepolarisations in adjacent cells (Verkerk et al., 2000). In Dutta et al. (2016), models of human ventricles with ischaemic regions were used to investigate the mechanism of re-entrant arrhythmia in the acute ischaemic heart. Block of hERG induced EADs and transmural re-entry. In the ischaemic region border zone, transmural re-entry was sustained by EADs triggered by electrotonic current. A prolonged low-amplitude current applied to ventricular cell models during the repolarisation phase was sufficient to induce reactivation of the L-type calcium current and the formation of EADs. Therefore, EAD thresholds for an injury current could be used as a proarrhythmic risk metric, as they would be based on a realistic mechanism for arrhythmia formation in tissue. This can be implemented as an alternative pacing protocol, with a prolonged low-amplitude stimulus current.

3.5.2 Classification and machine learning

There are two types of classification problem in machine learning: supervised and unsupervised (Aggarwal, 2015). The prediction of proarrhythmic risk in this context is a supervised task, because data on risk class for each drug are available. However, unsupervised methods can be of use in finding similarity between different drugs.

The performance of a classification technique can be analysed by looking at its bias and variance. A technique with high variance will give very different results if small changes are made to the dataset, whereas a technique with high bias will suffer from over-simplification. When a dataset contains a relatively small number of observations, machine learning classification techniques with a low variance are preferable, even if they have a higher bias than alternative methods (James, 2021). Supervised classification techniques include linear discriminant analysis (LDA) and support vector machines (SVM). LDA is effective when data are normally distributed within categories. When this assumption is true, LDA is the preferred method for multi-class classification problems with small datasets (James, 2021). LDA is a global method which considers all data points when assigning category boundaries. In Mirams et al. (2011), LDA was used to separate drugs into four risk categories. Conversely, SVM considers only the data points closest to the margins. In SVM, no assumptions are made about the distribution of the data. Instead, the optimal separation is calculated by minimising the distance of overlapping points from the decision boundary. (Hastie, 2009) SVM was used by Lancaster and Sobie (2016) to find the optimal thresholds for classification into two categories.

By choosing these two very different methods, we can account for differences in data distribution within classes, and for the importance of the whole dataset vs. only the points on the margins.

Alternative supervised classification methods include logistic regression, K-nearest-neighbours and naïve Bayes. Logistic regression is a similar technique to LDA, but does away with the requirement for the data to be normally distributed within the groups. This leads to higher variance in cases when the normal distribution assumption holds. Therefore, LDA is preferable to logistic regression when this assumption holds (Hastie, 2009). K-nearest-neighbours is most effective for large datasets with highly non-linear boundaries between categories. While it has a low bias, it has a high variance (Aggarwal, 2015). Naïve Bayes relies on the assumption that different predictors for the same observation are independent of each other (James, 2021). Most of the classifications in this work make use of a single predictor, i.e. the threshold value found by a particular intervention. However, in some of these analyses we have used two or more predictors. In these cases, it is likely that the predictors will be correlated with each other, meaning that the assumption of independence does not hold and therefore, naïve Bayes is inappropriate.

3.5.3 Measuring accuracy

In order to compare torsadogenicity metrics to one another, their accuracy in predicting risk must be assessed. In addition to the CiPA method, in which 12 drugs were selected for training data and a further 16 drugs were selected for validation data, there are a wide variety of ways in which metrics have been assessed in the literature. Drug data sets vary greatly in both the number of drugs considered (from 12 (Dutta et al., 2017) to 372 (Beattie et al., 2013)), and the number of risk categories they are split into: four (Mirams et al., 2011; Christophe, 2013; McMillan et al., 2017a; Passini et al., 2017; Christophe, 2022), three (Dutta et al., 2016; Li et al., 2017; Dutta et al., 2017), and two (Beattie et al., 2013; Mirams et al., 2014; Lancaster and Sobie, 2016).

Leave-one-out cross-validation is a technique wherein one drug is removed from the dataset and the boundaries are re-calculated based on the remaining data points. The mean accuracy of categorisation when this is repeated for every drug in the dataset can be used as a measurement of the accuracy and robustness of the metric (Hastie, 2009). This technique has the benefit of making use of a small dataset by using each data point for both training and validation, and it is commonly used, including by Mirams et al. (2011), Lancaster and Sobie (2016), and Li et al. (2019).

When a binary classification system is used, i.e. when compounds are assigned either ”torsadogenic” or ”non-torsadogenic” status, rather than any intermediate states, sensitivity and specificity can be calculated. Sensitivity is defined as the probability that a positive value will be categorised correctly, and specificity is defined as the probability that a negative value will be categorised correctly (Aggarwal, 2015). Accuracy can also be calculated by finding the fraction

Table 3.1: Table of possible values for a binary classifier. From this you can calculate sensitivity ($\frac{TP}{TP+FN}$), specificity ($\frac{TN}{TN+FP}$), and accuracy ($\frac{TP+TN}{TP+FP+TN+FN}$).

	Predicted class	
Real class	TdP+	TdP-
TdP+	True Positive (TP)	False negative (FN)
TdP-	False positive (FP)	True negative (TN)

of all predictions which were accurate (i.e. true positives and true negatives). Table 3.1 shows how true and false positives and negatives are defined, and how sensitivity, specificity, and accuracy can be calculated. Receiver operator characteristic (ROC) curves can be used to visualise the trade-off between sensitivity and specificity for continuous classifiers. Sensitivity is plotted against specificity for each possible separating threshold between the classes, and the area under the curve can be used to compare classifiers (Hastie, 2009; Li et al., 2019).

For multi-class problems, binary methods can be used if the problem is split into several binary classes (Aggarwal, 2015). Additionally, comparing only the most and least torsadogenic drugs and omitting the intermediate risk categories entirely is frequently used alongside multi-class classification, to assess the classifier's performance in the most extreme cases (Passini et al., 2017; Li et al., 2019; Christophe, 2022).

Looking at individual mis-classifications can also be instructive for comparing the suitability of different metrics and models to different types of drug. For example, in Tomek et al. (2019), the ToR-ORd model correctly classified the sodium current blocker mexiletine as non-torsadogenic using the Passini et al. (2017) metric, whereas the original ORd model led to mis-classification of this compound, which may indicate that the improved representation of sodium blockers in the ToR-ORd model makes this model more appropriate for predicting the risk of this kind of drug. Similarly, the optimisation of the Li et al. (2017) model by Dutta et al. (2017) improved the prediction of mexiletine's risk category.

There is an inherent circularity in the process of choosing a TdP risk metric based on its accuracy - it is possible to overfit the model to the data, or to focus on a predictive parameter that in reality bears little correspondence to the clinical risk other than a spurious correlation. There are two main ways to overcome this: by strict separation of training and validation data as in Li et al. (2019), and also by ensuring that the proposed metrics have a mechanistic basis in biological reality. In these ways, the dangers of overfitting and spurious correlations can be reduced.

3.6 Conclusion

Torsades de Pointes arrhythmia is a form of polymorphic ventricular tachycardia, which can be caused by medications, and can lead to sudden death (Yap and Camm, 2003). Drug interactions with the hERG cardiac potassium channel, which carries the $\mathrm{I_{Kr}}$ current, are linked to Torsades, and hERG block testing is mandatory for new drugs (European Medicines Agency, 2005; Redfern et al., 2003). However, not all drugs which block hERG are known to cause Torsades, which means that hERG block may lack specificity as a predictor of arrhythmic risk (Kramer et al., 2013). Some compounds, such as ranolazine, which block multiple ion currents in addition to hERG have lower arrhythmic risk (Antzelevitch et al., 2004). Multi-ion current block has been investigated as a predictor for arrhythmic risk, both alone (Kramer et al., 2013), and in combination with simulation of QT prolongation in electrophysiological models (Mirams et al., 2014). However, as QT prolongation does not always lead to Torsades (Sager, 2008), approaches which offer a mechanistic link between drug action and Torsades are needed.

Early afterdepolarisations (EADs) are a cell-level repolarisation abnormality, in which the cell depolarises a second time before the resting voltage has been reached (Segers, 1941). During Torsades de Points arrhythmia, EADs can be directly observed in human hearts (Li et al., 2020a). The mechanism by which EADs lead to Torsades is not fully understood, but likely candidates include synchronisation of patches of cells (Vandersickel et al., 2016), breaking up of spiral waves (Van Nieuwenhuyse et al., 2017), and facilitation of re-entry (Dutta et al., 2016). At the cell level, ionic mechanisms which cause EADs include reactivation of the L-type calcium (Sridhar et al., 2017) and fast sodium (Sato et al., 2017) currents, and release of calcium from the sarcoplasmic reticulum and subsequent reactivation of the sodium-calcium exchanger (Kurata et al., 2020). From a dynamical systems analysis perspective, for a system to show EADs, a Hopf bifurcation (in which a steady state moves to an oscillatory state as an input parameter is varied) is necessary (Tran et al., 2009).

Predictive metrics based on EADs have generally used an increase in drug concentration up to 100 times the usual concentration to provoke EADs, sometimes in combination with variability and disease states (Christophe and Crumb, 2019; Passini et al., 2017). Machine learning techniques such as linear discriminant analysis (Mirams et al., 2011) and support vector machines (Lancaster and Sobie, 2016) have been used to determine boundaries between risk categories. Methods for assessing the accuracy of metrics have included calculations of sensitivity and specificity (Passini et al., 2017; Li et al., 2019; Christophe, 2022), and leave-one-out cross-validation (Mirams et al., 2011; Lancaster and Sobie, 2016; Li et al., 2019).

In our work, we have created a novel predictor using pathogenic interventions to induce EADs in cardiac cell models in combination with normal physiological drug concentrations.

Chapter 4

Computational Methods

Contents

4.1 Introduction

As discussed in the previous chapter, early afterdepolarisations are important in drug-induced Torsades de Pointes.

In the first section, I report our methods for a systematic search of the literature for ion channel block data for 41 drugs, the simulation of ion channel block in a cell model, and the simulation of EADs. In the second section, I report the methods for calculating other proarrhythmic risk prediction metrics from the recent literature. In the third section, I report our methods for classifying drugs based on the metrics discussed in the previous two sections using linear discriminant analysis and support vector machines. The fourth section shows the methods for investigating the effects of cycle length, extracellular potassium concentration, drug concentration, and epi- or endo-cardial model choice on the accuracy of prediction.

4.2 Methods

4.2.1 EAD thresholds

We selected 41 drugs of known torsadogenic risk, and simulated their ion channel blocking effects in the O'Hara et al. (2011) human ventricular cell model. Using a range of interventions, we determined the threshold of intervention at which an EAD could be provoked in the cell model, i.e. the lowest level of intervention that was necessary to cause an EAD. The differences in 'threshold for EAD' between different drugs were used to classify drugs by arrhythmic risk. These steps are detailed below.

Drug inclusion criteria

To select drugs to use as a training set, we used three criteria based on the amount of data available on both the pro-arrhythmic risk of the compound and its effect on ion currents in cardiac cells.

1. As a starting point, we included drugs that were previously studied in Mirams et al. (2011).

2. Additional drugs were then included in our study if they had been included in five or more of the papers analysing TdP risk discussed in a recent summary paper (Wiśniowska and Polak, 2017) and if over 70% of studies agreed on high or low TdP risk.

3. Drugs that are on the CiPA list (Sager et al., 2014) were automatically included if ion current block data were available for three or more channels of interest (even if they had been in fewer than five studies or had poor agreement in risk category between studies).

If there was disagreement in risk class using the above sources, the default category was the one used in Mirams et al. (2011), and if not listed there then the one used in Redfern et al. (2003).

To be included in our dataset, the drugs were also required to have IC_{50} values available in the literature for three or more of the ionic currents of interest, found by manual patch clamp. The

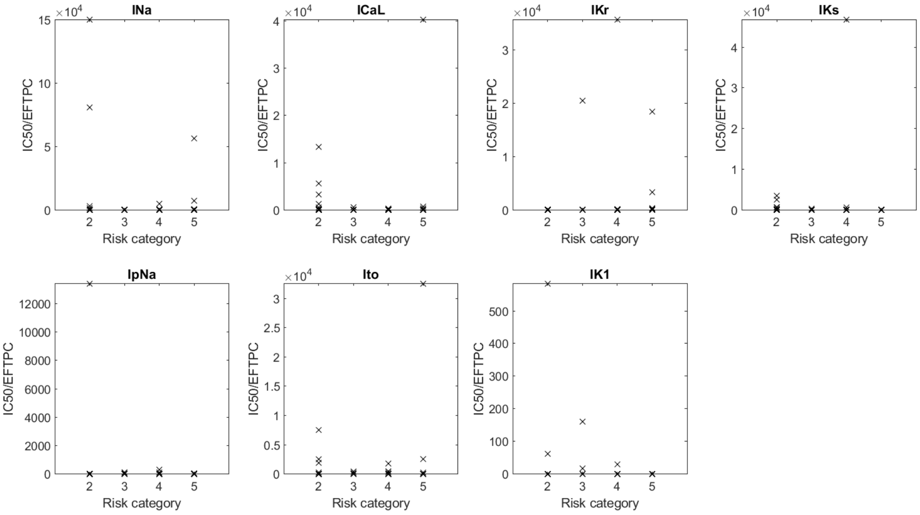

Figure 4.1: Block of each current for each drug in the dataset, plotted against risk category. Block is represented as IC50/EFTPC.

ionic currents of interest were: the fast and late/persistent sodium currents, the L-type calcium current, the rapid and slow delayed rectifier potassium currents, the transient outward current, and the inward rectifier potassium current. The IC_{50} values we used are given in Table 4.1, and the references for these can be found in the supplementary material. IC_{50}s are represented as pIC_{50}s, which is the negative log of the IC_{50} in molars, to make them more readable. Where there were multiple IC_{50} values available, preference was given to those from human cells at body temperature (37°C) and to the most recent study.

Stratification into 4 risk categories was taken from the Mirams et al. (2011) paper where available, and the Redfern et al. (2003) paper otherwise. We pooled risk categories 1 and 2 together, as they represent the same risk level for different drug classes, leaving classes 2–5 (Mirams et al., 2011; Redfern et al., 2003). The only compounds in the dataset not covered by this metric were: (i) ranolazine, which was assigned to Category 4, i.e. the drug has isolated reports of TdP in humans; and (ii) cibenzoline, which was assigned to Category 5 based on Lawrence et al. (2006), i.e. there are no reports of TdP in humans with this drug (Liu et al., 2013; Mittal, 2014).

Table 4.1: pIC_{50} values for each compound in the dataset (shown as log M) for the fast sodium (I_{Na}), L-type calcium (I_{CaL}), rapid delayed rectifier potassium (hERG or I_{Kr}), slow delayed rectifier potassium (I_{Ks}), persistent sodium (I_{pNa}), transient outward (I_{to}) and inward rectifier potassium (I_{K1}) currents, maximum effective free therapeutic plasma concentration ($EFTPC_{max}$ or C_{max}) (nM), and the risk category. For references, please see the supplementary materials.

Compound	pIC_{50} (log M)							C_{max}	Risk
	I_{Na}	I_{CaL}	hERG	I_{Ks}	I_{pNa}	I_{to}	I_{K1}	(nM)	category
ajmaline	5.0862	4.1487	5.983			5.5751		17103	2
amiodarone	4.3936	6.5686	7.5229	5.7595	5.1739	5.425		0.5	2
amitriptyline	4.699	4.9355	5.4841	5.5627	5.3533	5		41	4
azimilide	4.7212	4.7496	7	5.8539				70	2
bepridil	5.4318	6.6757	6.2218	5	5.7414	5.1805		33	3
chlorpromazine	5.5528	5.5229	5.8297		5.341	4.7959	5.2147	38	3
cibenzoline	5.1079	4.5229	4.6459	4.9101	4.3318			976	5
cisapride	4.8327	4.7959	8.1871	5.4698		5.0301		4.9	2
clozapine			5.6021					1603	4
desipramine	5.8182	5.7673	5.857					108	4
diltiazem	4.8477	7.2676	5.1314			4.5346		122	5
disopyramide			5.7447	4.091		4.6799		742	2
dl-sotalol			3.556					14733	2
dofetilide	3.5229	4.5735	8.301					2	2
flecainide	5.1871	4.5918	5.7959		5.4685	5.1079		753	3
fluvoxamine	4.4045	5.3098	5.4202					264	4
halofantrine			7.6655					0.5	3
imipramine	5.4437	5.0915	5.4685			4.301		106	4
loratadine			5.0809					0.45	5
methadone	4.9508	4.5735	5.3188					507	2
mexiletine	4.3665	4	4.301		4.7545			4129	4
mibefradil	6.0088	6.8069	5.7447		5.4403			12	4
nifedipine	4.4318	7.2218	3.5607	3.4437		4.8633		7.7	4
nitrendipine	4.6655	7.6021	5			5.1135		3.02	5
ondansetron	4.0531	4.6468	6.0915		4.7171			899.88	2
pentamidine			3.6882				6.7696	10	3
phenytoin	4.3098	3.9872	4					7000	5
pimozide	7.2676	6.6198	7.8239					0.43	3
prenylamine	5.5986	5.9066	7.1871					17	2
propafenone	5.9245	5.7447	6.3565		5.394	5.3188	5.1487	241	4
propranolol	5.6778	4.7447	5.5485					26	5
quetiapine	4.7721	4.983	5.2392					33	5
quinidine	4.7799	4.8069	6.5229	5.3099		3.058	3.699	3237	2
ranolazine	3.5317	3.5287	4.9393	2.7212	5.1871			3200	4
risperidone	3.9914	4.1367	6.2218					1.81	5
sertindole	5.6383	5.0506	7.8539	6.0555		5.3979		1.59	2
tedisamil	4.699		5.6021			5.3565		85	2
terfenadine	6.0128	6.426	8.0506	5.699				9	2
terodiline		4.8182	8.3979	4.5229			5.1549	12	2
thioridazine	5.7375	5.8861	7.4815	4.8539				979	3
verapamil	4.382	7	6.8447			2.5796		81	5

Action potential and drug block models

We used a human ventricular myocyte electrophysiology model based on human datasets, the O'Hara et al. (2011) endocardial cell model. The O'Hara et al. (2011) model is used very frequently in proarrhythmia modelling (Cavero and Holzgrefe, 2015). Unlike some previous models, blocking the hERG potassium current in the O'Hara et al. (2011) model is sufficient to produce an EAD, just like in human ventricular myocytes. The model also includes the persistent sodium current, which is considered to be important in suppression of arrhythmias. The endocardial variant of this model was chosen for these simulations as the model was based on experiments performed on endocardial cells, and the epicardial model is a modified version of the endocardial model. The Grandi et al. (2010) model was used to calculate some of the APD metrics. Drug block of ion channels was modelled as a reduction in channel conductance as a function of the concentration of the compound, $[D]$, and the IC_{50} value (Bottino et al., 2006). The change in maximum conductance for a channel j was described by a Hill equation:

$$g_j = \bar{g}_j \left[1 + \left(\frac{[D]}{[IC_{50}]} \right) \right]^{-1}, \tag{4.1}$$

where g_j is the maximum conductance of the drug-blocked channel, and $\bar{g}_j$ is the conductance of the channel when there is no compound present. The Hill coefficient here is set to 1, as in Mirams et al. (2011) and Whittaker et al. (2021) as the variability in experimentally-inferred Hill coefficients from patch clamp can be so high that using 1 as the Hill coefficient may reduce error (Elkins et al., 2013).

Drug concentrations were set to the maximum effective free therapeutic plasma concentrations (EFTPC) for each individual drug, to provide a realistic estimate of ion channel block *in vivo*. For a list of EFTPCs, see Table 4.1.

Detecting afterdepolarisations

The appearance of early afterdepolarisations (EADs) in a simulation was determined by the slope of the voltage trace between adjacent time points. The voltage trace from a simulation was extracted and the difference between adjacent time points was calculated for the whole trace. Whenever the slope was greater than $+1\,\mathrm{mVms}^{-1}$, a depolarisation was reported. To

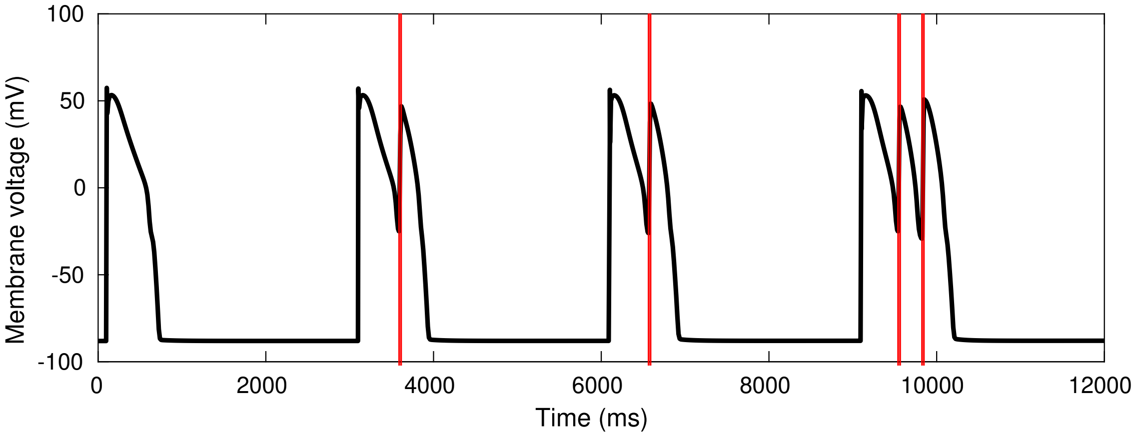

Figure 4.2: Examples of EADs detected with the afterdepolarisation detection algorithm. The red lines show where an EAD was detected.

remove depolarisations caused by the stimulus, depolarisations that occurred between 50 ms before and 100 ms after each stimulus were disregarded. An example of some EADs detected by the algorithm can be seen in Figure 4.2. The red lines show where an afterdepolarisation was detected. From manual examination of voltage traces aligned with AD detection, this algorithm was able to detect all afterdepolarisations that were visible to the eye. For the full algorithm, see the `DetectAfterDepolarisations` class in the code repository (see “Numerical methods and simulation procedure”).

Provoking afterdepolarisations

The failure of hERG block alone to predict torsadogenic risk suggests that drug-induced TdP is mediated by more than one ionic mechanism. We hypothesise that the interaction of certain disease states with torsadogenic drugs could lead to greater susceptibility to TdP. We propose to look at the single-cell phenomenon of EADs, as studies suggest TdP and EADs are intrinsically linked (Habbab and El-Sherif, 1990; El-Sherif et al., 1988; Choi et al., 2002; Roden, 1993; Volders et al., 2000). Spatial differences in ion channel expression throughout cardiac tissue would alter the susceptibility of each cell to EADs, meaning that some regions would have EADs while others did not, increasing the probability of re-entrant waves. However, we have constrained this study to look at the initiation of EADs in a single cell as an initiation event.

To simulate disease states after drug block was applied, EADs were provoked using three interventions mimicking disease states discussed in the introduction:

- conductance of the L-type calcium current was increased by a scaling factor to simulate a gain-of-function mutation which causes LQT8, or the effect of calcium agonists (Kang et al., 2010). Increasing ICaL has been used to provoke EADs in cardiac systems since the first description of EADs by Segers (1941), usually in combination with hERG block to further reduce repolarisation reserve (Vandersickel et al., 2016). Here, we have considered increased ICaL and reduced IKr separately.
- conductance of the rapid delayed rectifier current I_{Kr} (hERG) was decreased by a scaling factor to simulate the effect of LQT2 mutations (Curran et al., 1995).
- A stimulus current of between 0 and -1 $\mu A \mu F^{-1}$ was applied to the cell model in addition to the regular pacing stimulus to mimic the effects of an ischaemic injury current, as in Dutta et al. (2016).

Although LQT1 (caused by a decrease in I_{Ks}) and LQT3 (caused by an increase in I_{pNa}) are both common causes of Torsades de Pointes, we have not investigated them in this study, because we were unable to produce EADs in the O'Hara et al. (2011) model with either block of I_{Ks} or increase in I_{pNa} at any level.

The O'Hara et al. (2011) model was used for these EAD simulations, as it includes all of the currents of interest, and has been recommended for CiPA-related proarrythmic risk prediction. (Sager et al., 2014). We used a slow pacing interval of 3 seconds because bradycardia is also known to facilitate onset of EADs and TdP (El-Sherif et al., 1988). The effect of using different cycle lengths is discussed in Section 4.2.4.

In order to check that there was only one EAD threshold for each intervention, i.e. that at increasing intervention levels the simulations switched from showing no EADs to showing EADs without then switching back again, intervention profiles were produced for each intervention and drug. In Figure 4.3 the intervention profile for the fast sodium inactivation curve shift intervention can be seen for the control model (i.e. without drug block applied), and for two drugs, cisapride and nitrendipine. For low levels of inactivation curve shift, no EAD is seen, then for higher levels EADs are detected. After the threshold, EADs are found for each simulation, indicating that interval-bisection-based threshold finding methods will find one true threshold.

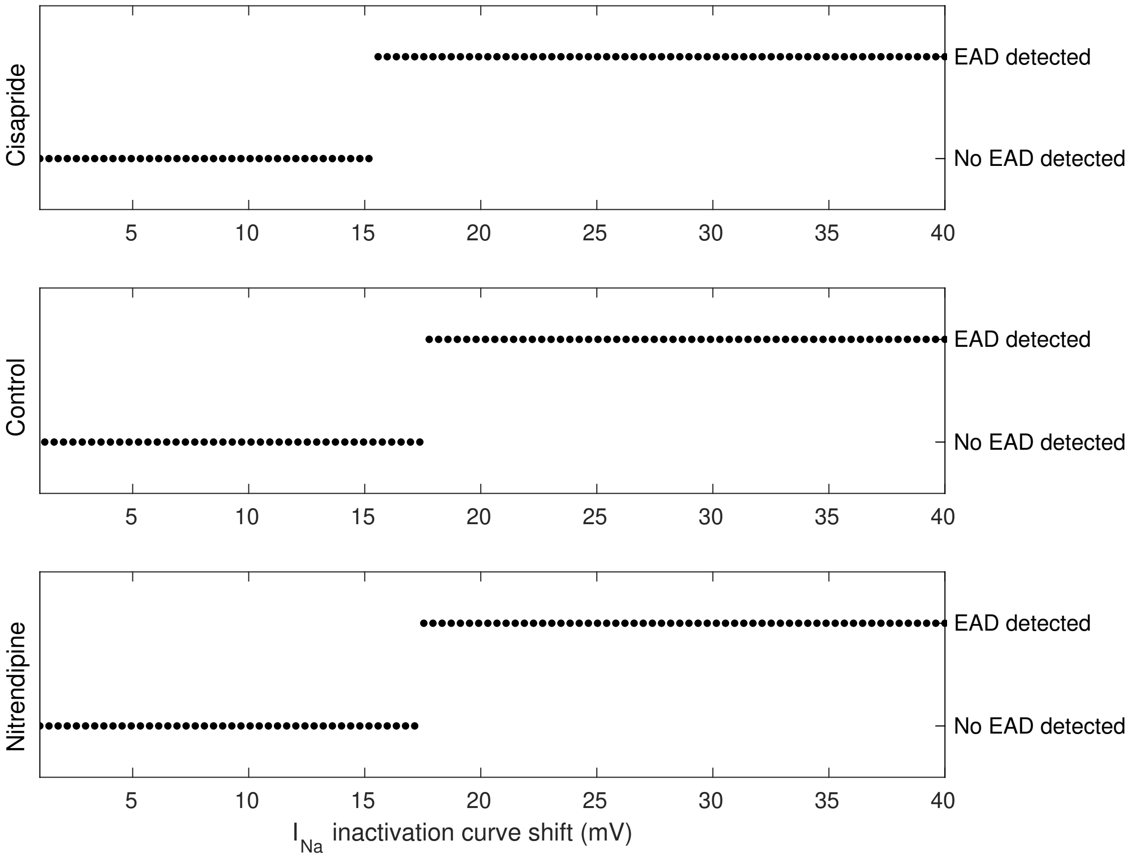

Figure 4.3: Profile of fast sodium inactivation shift intervention, showing that only one threshold can be found in the range tested.

Numerical methods and simulation procedure

Simulations were run using the Chaste C++ framework (Mirams et al., 2013; Cooper et al., 2015) with custom written code. Cell models and initial conditions were imported from CellML (Cuellar et al., 2003) files using PyCML (Cooper et al., 2006).

The adaptive timestep solver CVODE (Cohen and Hindmarsh, 1996) was used to solve the model's differential equations, with a relative tolerance of 10^{-5} and absolute tolerance of 10^{-7}. The output timestep was 0.1 ms and a stimulus current was applied every 3 s for 3 ms with a magnitude of -25.5 $\mu A \mu F^{-1}$.

The procedure we used is outlined in Algorithm 1. First, drug block was applied to the model by modifying the conductance parameters for the appropriate channels, using Equation (4.1) to calculate updated conductances. The model was then run to steady state using the pacing protocol above. Steady state was reached when the norm of the change in the model's state variables was less than 10^{-6} between paces. This generally took 1,000–10,000 paces. By first stabilising the model under drug action, and then applying the EAD-inducing interventions for a brief time period, the drug actions at physiological concentrations are firmly established, and then only enough pathological provocation is applied to elicit a response. This has the benefit of efficiency - as the slow steady-state part of the simulation only needs to be run once for each drug - and also means that the drug effects are given precedence over the parameter changes of the intervention. Changes in open and closed states of ion currents over sequential beats have been shown to contribute to the dynamical chaos that is a feature of EAD genesis (Tran et al., 2009; Kurata et al., 2005), so the simulation is run for four paces rather than one pace to allow for this effect.

EAD-provoking interventions were applied by modifying either the $\mathrm{I_{CaL}}$ conductance, or the $\mathrm{I_{Kr}}$ conductance. After setting the intervention parameter, the simulation was run for 12 s, and the presence or absence of EADs was detected. Interval bisection was used to find the threshold of intervention that was necessary to cause any EADs. We started with interval ranges of: $[1, 80]$ for the $\mathrm{I_{CaL}}$ conductance scaling; and $[0, 1]$ for the $\mathrm{I_{Kr}}$ conductance scaling. The large interval range used for the L-type calcium current conductance is necessary to accommodate the drug diltiazem, which is a major outlier for this intervention. Most threshold values fall between 1-30x gCaL. Interval bisection was set to terminate when consecutive values were less than 10^{-4} units apart. EAD simulations for a single compound can be run in less than 10 minutes, and many compounds can be run in parallel. All the code is available to download from github at `https://github.com/teraspawn/EadPredict`.

Effect of timing and duration of injury current

In order to maximise the accuracy of prediction of this method for EAD provocation, both the timing and the duration of the injury current were varied. Thresholds were obtained as above, and used to classify drugs into risk categories. The accuracy of this classification was used to establish which timing-duration combination was the most effective for proarrhythmic risk prediction. First, a wide grid of values were used: EC durations of 50, 100, 150, or 200 ms,

Algorithm 1 procedure to find the EAD threshold.

```
Set ion channel conductances in cell model to new values based on drug block.
Run cell model to steady state and then save this state to reset to later.
Set upper and lower limits $\alpha, \beta$ for intervention value.
repeat
    Reset cell model to earlier state.
    Set intervention to $(\alpha + \beta) \div 2$ (e.g. multiply $\mathrm{I}_{\mathrm{CaL}}$ conductance by this factor).
    Run model for $12\,\mathrm{s}$.
    Check for Early afterdepolarisation (upwards trajectory after initial depolarisation).
    Adjust $\alpha$ or $\beta$ using interval bisection.
until $|\alpha - \beta| < 10^{-4}$
```

beginning when the membrane voltage reached 0, -20, -40, or -60 mV during the repolarisation phase of the action potential.

The timing of the injury current was then further refined to 5mV, then 1mV intervals.

4.2.2 Previously suggested measures

The Redfern et al. (2003) safety margin was calculated for each drug using the hERG IC_{50} divided by the $\mathrm{EFTPC}_{\mathrm{max}}$, to give a dimensionless measure that represents the fold increase in drug concentration above $\mathrm{EFTPC}_{\mathrm{max}}$ required to block the hERG current by 50%.

The APD90 metric was calculated using the `ApPredict` bolt-on project (Williams and Mirams, 2015) and the Chaste C++ framework (Mirams et al., 2013; Cooper et al., 2015). As in Section 4.2.1, the ion current conductances were modified to simulate drug block and the model was run to steady state. The maximum and minimum voltages reached during the action potential were recorded from two simulated paces. The threshold voltage for APD90 was defined as 10% of the distance from the lowest to the highest voltage. The time between the voltage reaching this value on the upstroke and the voltage reaching this value during repolarisation was recorded as APD90. The endocardial variant of the O'Hara et al. (2011) model was used for this calculation as the cells used for data in the O'Hara et al. (2011) model were endocardial cells, and the epicardial and M cell models were extensions to the original endocardial model.

APD50 for the Lancaster and Sobie (2016) metric was calculated in the same way, except that the threshold value was defined as 50% between the lowest and highest voltage. The epicardial O'Hara et al. (2011) model was used for this metric to match the metric used in the Lancaster and Sobie (2016) paper. The diastolic calcium concentration was calculated by running the cell model for a single pace after running to steady state, and extracting the intracellular calcium concentration at a time point 1 ms before the end of the simulation, i.e. during the diastolic period.

The cqInward metric from Li et al. (2017) was calculated by finding the total L-type calcium current and persistent sodium current during a single action potential in the O'Hara et al. (2011) model. As with the other metrics, the conductances of the model were modified to simulate the effects of the drugs and then the model was run to steady state. The area under curve (AUC) for the L-type calcium current and the persistent sodium current were calculated using the trapezium rule, which for a current I can be expressed as

$$I_{AUC} = \sum_{k=1}^{N} \frac{I(t_k) + I(t_{k+1})}{2} \Delta t_k, \tag{4.2}$$

where the time period $[a, b]$ is split into N discrete segments of size Δt_k. The total current between t_k and the next time point, t_{k+1}, is approximated as a trapezium. In this way, the area under curve for the whole current can be approximated as a series of trapeziums. The cqInward metric is defined as

$$cqInward = \left(\frac{INaL_{AUC,drug}}{INaL_{AUC,control}} + \frac{ICaL_{AUC,drug}}{ICaL_{AUC,control}} \right) \times 0.5, \tag{4.3}$$

where $INaL_{AUC}$ and $ICaL_{AUC}$ are the areas under curve for the persistent sodium and L-type calcium currents, respectively. The AUCs were calculated for the simulations both with drug effects applied and without drug effects applied (control), then normalised and combined. The cqInward metric without compound is defined as 1. cqInward was calculated at drug concentrations at 1-25 ×EFTPC$_{\text{max}}$ for each drug in the test set using the O'Hara cell model. The Grandi model could not be used for this metric, as it does not include persistent sodium.

The qNet metric from Dutta et al. (2017) is an extension of the cqInward metric that considers total currents that are active during the action potential, without normalising by the drug-free model. qNet is calculate as the area under the curve for INet, where INet is calculated as:

$$INet = ICaL + INaL + IKr + IKs + IK1 + Ito. \tag{4.4}$$

At faster pacing rates, cqInward was found to be less accurate than qNet, so we have calculated cqInward at a cycle length of 3000 ms, and qNet at a cycle length of 2000 ms.

4.2.3 Classification

After calculating proarrhythmic risk predictor metrics, it is then imperative that there be some method of using the metrics to assess the risk of the compound, by assigning it to a risk category or by comparing it to other drugs of known risk. As there is a great deal of overlap in the categories, as we have shown graphically in Figure 4.1, and the data do not seem to follow an obvious parametric distribution, machine learning techniques are necessary.

In this section, we use linear discriminant analysis and support vector machines to classify drugs into discrete risk categories, and then assess the accuracy of each classification system.

Pro-arrhythmic risk classification

As in Mirams et al. (2011), risk categories were based on the Redfern et al. (2003) classes (with Category 1 and Category 2 pooled, as they represent equivalent levels of risk for different drug classes):

- Category 2: Either Class Ia and III antiarrhythmics, or drugs that have been withdrawn from market due to TdP.
- Category 3: drugs with a measurable incidence or numerous reports of TdP in humans.
- Category 4: drugs with isolated reports of TdP in humans.
- Category 5: drugs with no reports of TdP in humans.

We tested two classification methods: linear discriminant analysis (LDA), and support vector machines (SVM).

Linear Discriminant Analysis

In LDA, the metrics in categories are assumed to follow a Normal distribution, and the points where the inferred distributions overlap are used as the category boundaries (Tarca et al., 2007). An example for a 1D dataset is plotted in Figure 4.4. Three groups of data were produced from random normal distributions. The different groups are denoted by marker colour and shape. The data points are plotted at the top of the figure. Below are plotted the probability density functions for each group, which are derived by calculating the mean and standard deviation of each data group. Given a new data point, it can be placed into one of the groups based on which probability density function is greatest at that point.

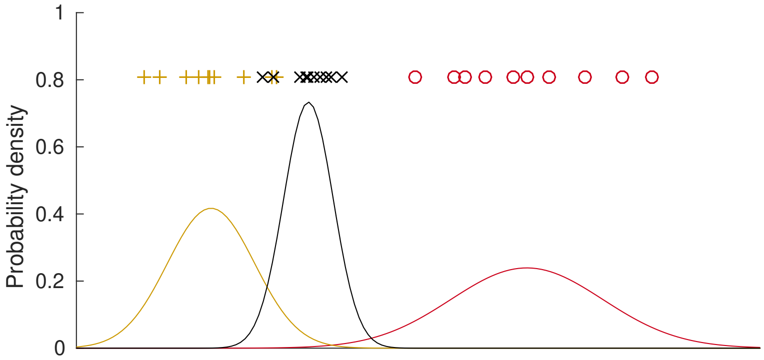

Figure 4.4: Linear Discriminant Analysis example for a one dimensional dataset. The data points are plotted at the top, denoted by marker colour and shape. Below are plotted the probability density distributions for the data.

Support Vector Machines

In SVM, a hyperplane is used to separate the data points, and the optimal hyperplane is found by maximising the distance between the hyperplane and the closest points to it (Cristianini and Shawe-Taylor, 2000). In the case when the groups are not separable (i.e. when points in each group overlap with the others), a loss function is introduced based on the distance between points on the wrong side of the margin and the margin, and the loss function is minimised. Examples of SVM classification on a separable (top) and non-separable (bottom) dataset are shown in Figure 4.5. The data are plotted in the centre of each plot, and below are plotted the support vectors. These are vectors between the closest points in the two groups to each other and the classification boundary. For separable datasets, these vectors are maximised to find the boundary. For non-separable datasets, vectors between points that lie on the wrong side of the boundary and the boundary are minimised using a loss function. These vectors are plotted above the dataset.

SVM and LDA will often give different boundaries between each category.

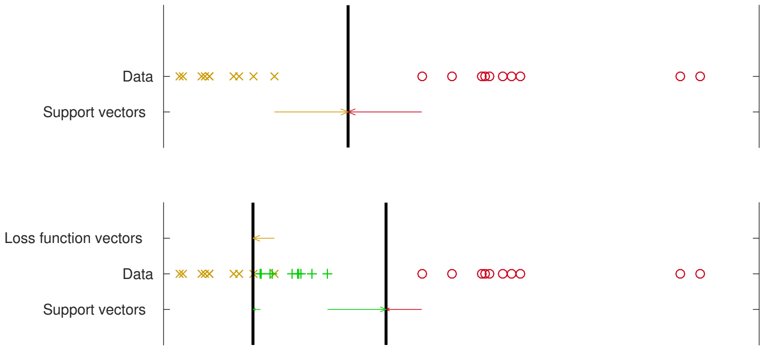

Figure 4.5: Support Vector Machines example for a one dimensional dataset. Top plot: a separable dataset with a hard boundary and no loss function. Bottom plot: an inseparable dataset with a soft boundary and a loss function. The data points are plotted in the centre of each plot, denoted by marker colour and shape. Below are plotted the support vectors, and above are plotted the vectors used by the loss function.

Errors

In leave-one-out cross-validation one drug was removed from the dataset and the boundaries were re-calculated. The left-out drug was then placed into a risk category based on these new boundaries. 5-group cross-validation was also used: drugs were randomly assigned to five groups, and then each group was removed from the dataset and the classification boundaries were re-calculated. The drugs in the removed group were then classified into a risk category based on these new boundaries, and accuracy was calculated.

Leave-one-out cross-validation and five-group cross-validation were used to check the robustness and accuracy of both the classifiers. We evaluated performance by calculating the errors in classification (how many risk classes away from the correct class a drug was classified as), and comparing these means of absolute error, E:

$$E = \frac{1}{N} \sum_{j=1}^{N} |a_j - c_j|, \tag{4.5}$$

where a is the actual category (i.e. the real risk category for the drug), c is the category assigned using the classification method, and N is the number of drugs in the dataset.

Binary classifications

To assess the effectiveness of each metric for classifying the most extreme examples - i.e. the most (group 2) and least (group 5) torsadogenic drugs - sensitivity and specificity were calculated for each possible value of boundary between TdP+ and TdP- groups. The area under the receiver operator characteristic curve was then calculated.

This approach was also applied to a binary classification involving all of the drugs, where groups 2 and 3 were assigned to the TdP+ group, and groups 4 and 5 were assigned to the TdP- group.

4.2.4 Modulators of arrhythmic risk

We hypothesise that the accuracy of classification using EAD metrics could be further improved by combining the EAD-provoking interventions with other features which are known to affect the formation of EADs. The difference between risk categories could be increased by different drugs having different responses to pro- and anti-arrhythmic modifications to the simulation parameters.

Effect of cycle length

In our earlier EAD simulations, we have used a slow pacing interval of 3 seconds, because bradycardia is known to facilitate the onset of EADs and TdP (El-Sherif et al., 1988). However, this is a very slow pacing rate for a human ventricular myocyte. We have also simulated the EAD metrics at cycle lengths of 500, 1000, and 2000 ms, and compared them to the results at our original cycle length.

Effect of extracellular potassium concentration

A reduction in potassium levels, hypokalaemia, is known to be a risk factor for Torsades de Pointes (Trinkley et al., 2013). During high intensity exercise, blood potassium levels have been shown to double, and then reduce to three-quarters of the original level (Medbø and Sejersted, 1990).

EAD thresholds were obtained by simulating disease states in the O'Hara et al. (2011) human ventricular cell model, as described in Section 4.2.1, but the extracellular potassium concentration was set at the same time as the drug ion current effects, to either 0.75× or 2× the original extracellular potassium concentration.

Effect of drug concentration

The concentration of compounds found in the blood varies from patient to patient due to differences in dosage, body mass and clearance rate (Urso et al., 2002). Certain drug interactions can reduce the clearance and metabolism of a particular drug in the body. For example, the concentration of terfenadine, a Group 2 drug which has been withdrawn from the market due to torsadogenic risk, increases when patients drink grapefruit juice, due to reduced conversion of terfenadine into its safer metabolite (Rau et al., 1997). Patients can also, intentionally or otherwise, overdose on medications. For example, the concentration of risperidone after an intentional overdose was found to be nearly 400 × the maximum therapeutic concentration of the drug (Nishikage et al., 2002). Concentration is considered to be a key factor in the onset of TdP.

EAD thresholds were obtained by simulating disease states in the O'Hara et al. (2011) human ventricular cell model, as described in Section 4.2.1. Instead of using the $\text{EFTPC}_{\text{max}}$, the reductions in ion current conductances to simulate ion channel block were calculated using $\text{EFTPC}_{\text{min}}$ or $10 \times \text{EFTPC}_{\text{max}}$ as the drug concentration.

Effect of endo- or epicardial model

The O'Hara et al. (2011) model is based on data from human endocardial myocytes. However, the authors of the paper extended the model to also simulate an epicardial myocyte. We used the endocardial variant of the model to run the EAD-inducing interventions described previously. We investigated the difference in EAD thresholds between the endo- and epicardial cell models.

EAD thresholds were obtained by simulating disease states in the O'Hara et al. (2011) human ventricular cell model, as described in Section 4.2.1, but using the epicardial rather than endocardial cell variant.

Chapter 5

Results

Contents

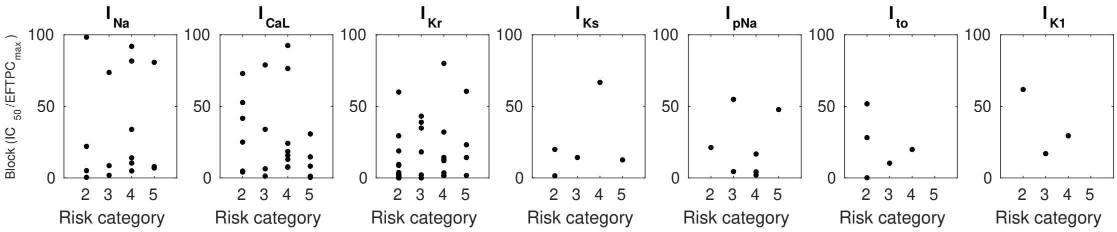

Figure 5.1: Ion channel block compared to risk category. Ion channel block (Y axes) is reported as $IC_{50}/EFTPC_{max}$ (dimensionless). A higher value of $IC_{50}/EFTPC_{max}$ corresponds to a weaker block.

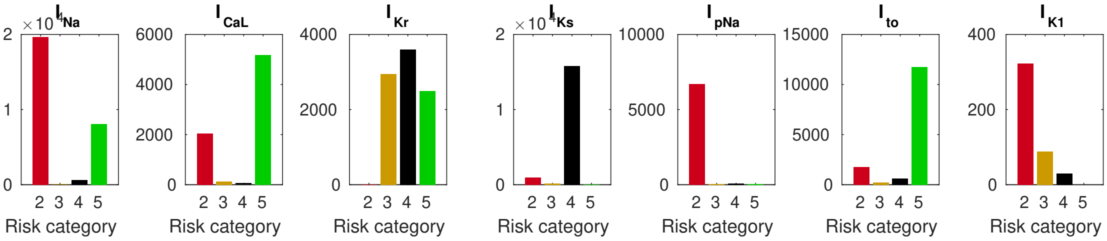

Figure 5.2: Means of ion channel block within each risk category. Ion channel block (Y axes) is reported as $IC_{50}/EFTPC_{max}$ (dimensionless). A higher value of $IC_{50}/EFTPC_{max}$ corresponds to a weaker block.

5.1 EAD thresholds

5.1.1 Drug data

The *in vitro* ion block action of each drug was calculated as the IC_{50} divided by the maximum effective therapeutic plasma concentration of the drug, i.e. how many multiples of the usual concentration would be required in humans to cause 50% block of the ion channel. Plots of ion current block against risk category are shown in Figure 5.1. Values of $IC_{50}/EFTPC_{max}$ over 100 are not shown.

No clear trend can be seen in the ion channel block data between the different risk categories for any of the ion currents of interest.

The average ion current block, reported as $IC_{50}/EFTPC_{max}$ (dimensionless), for each risk category is plotted in Figure 5.2. There is no clear trend in mean current block between risk categories, except for block of I_{K1}. However, I_{K1} IC_{50} values were only found for four compounds, so this may not be an overall trend.

This indicates that, in order to predict pro-arrhythmic risk from ion current block, ion currents must be combined in some way, such as the EAD threshold metric we present in this section.

5.1.2 Ionic mechanisms of provoked EADs

Increasing the conductance of the L-type calcium current by a factor of 24.1268, decreasing the conductance of the hERG potassium current by 84.6985%, or adding an injury current of -0.614075 uA/uF were sufficient to provoke an EAD.

Figure 5.3 shows the ionic currents and voltage traces for the L-type calcium increase, hERG block, and repolarisation phase injury current EAD interventions. When the L-type calcium current conductance was increased by a factor of 24.1268 (left), the ICaL current had both an increased amplitude and a second peak, reactivating during the repolarisation phase to cause an EAD. In addition, during the initial peak of the action potential, there is a reverse current through ICaL, presumably due to the increased concentration of calcium ions. This is a known limitation of the O'Hara et al. (2011) model, as discussed in Tomek et al. (2019). The persistent sodium current was reduced during the repolarisation phase, showing that it was not the main driver of the EADs, but it was active for longer and showed a small second peak towards the end of the EAD. The initial repolarisation before the EAD was slower than the control, and the IKr current activated later, and then activated a second time to repolarise the cell after the EAD. The IKs current was greatly increased, showing a small peak during the initial repolarisation, and then a larger peak during the final repolarisation.

Block of the hERG potassium current by 84.6985% (middle) prevented the participation of the IKr current in the process of repolarisation. Instead, the IKs current was increased.During each EAD peak, the ICaL current reactivated. The persistent sodium current remained active for longer during the action potential, but did not show peaks at the same times that the EADs were occurring, so although the increase in depolarising current during the plateau phase would have contributed to the overall depolarising factors in the cell, it was not the direct driver of the EADs.

The addition of the injury current (right) caused the persistent sodium current to remain active for longer during the action potential without reducing its initial peak, but the strongest driver of the EAD was the ICaL current. The second peak of the ICaL current was a near-perfect mirror image of the shape of the EAD. After the initial depolarisation, the IKr current does not deactivate as usual, but remains active and opposes the depolarising currents during the EAD. Unlike the other two interventions, the IKs current is not enormously increased, and instead shows only a small second peak during the EAD.

The EADs produced by all three interventions were driven by reactivation of the ICaL current. The fast sodium current does not reactivate for any of these interventions.

In the case of the ICaL conductance increase intervention, the large increase in depolarising current overwhelms the ability of IKr to repolarise the cell, and the IKs increase compensates for this. In the case of the hERG block intervention, the large reduction in repolarising current causes prolongation of the action potential and allows ICaL to reactivate, before the other repolarising currents are able to remedy the situation. Injury current during the repolarisation phase prompts the ICaL current to reactivate, but isn't accompanied by a reduction in IKr, meaning that IKr can remain the key current in the repolarisation process.

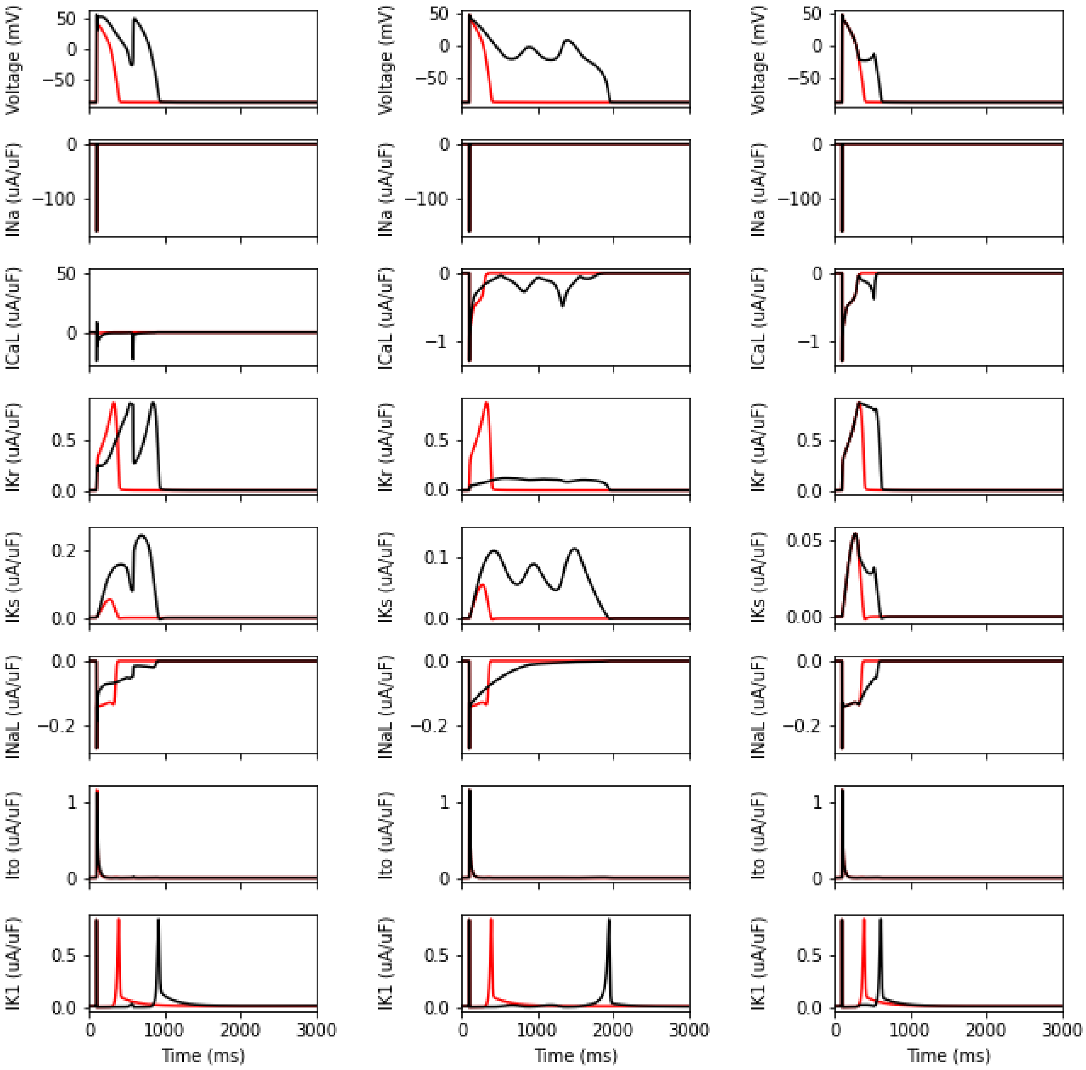

Figure 5.3: Reactivation of currents during EADs caused by each of the interventions. The O'Hara 2011 cell model was paced at a cycle length of 3000 ms until it reached steady state, and then the intervention was applied. The red line shows the current activity without intervention at this pacing rate. Left: EADs provoked by increasing the L-type calcium current conductance 25x. Middle: EADs provoked by 86% reduction of the hERG current conductance. Right: EADs provoked by an added stimulus current of -0.63 uA/uF for 200 ms when the membrane voltage reached -20 mV.

5.1.3 EAD thresholds compared to risk category

In general, more torsadogenic drugs caused a decrease in the threshold of intervention required to provoke an EAD, i.e. they made the electrophysiology models more vulnerable to EADs.

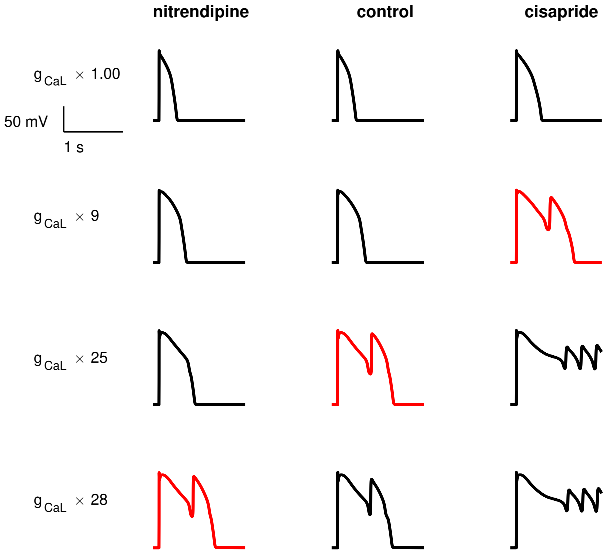

Figure 5.4: Some examples of EADs provoked using the L-type calcium increase protocol, as described in the methods section. The first EAD caused by the increasing intervention for each drug is highlighted in red. The less torsadogenic drug (nitrendipine) requires more provocation than the control to cause an EAD (i.e. its EAD threshold is higher), and the more torsadogenic drug (cisapride) requires less provocation (i.e. its EAD threshold is lower).

Some examples of EADs induced by the I_{CaL} increase protocol are shown in Figure 5.4. The low risk drug, nitrendipine, required a greater increase in I_{CaL} conductance (27.23×) than the control (24.13×) to induce an EAD. Conversely, the high risk drug cisapride required a much smaller increase (8.23×) to induce an EAD.

The means of EAD thresholds in each category are plotted in Figure 5.5. In contrast to the ion current block data, for all of the EAD metrics, the average threshold increases with decreasing risk, i.e. for lower risk drugs the cells are less susceptible to EADs, and for higher risk drugs, the cells are more susceptible to EADs.

Three drugs (ajmaline, quinidine, and thioridazine) produced EADs without any intervention required. All three of these drugs strongly block several currents, including INa, ICaL and hERG. In addition, ajmaline strongly blocks Ito, and quinidine and thioridazine both block IKs.

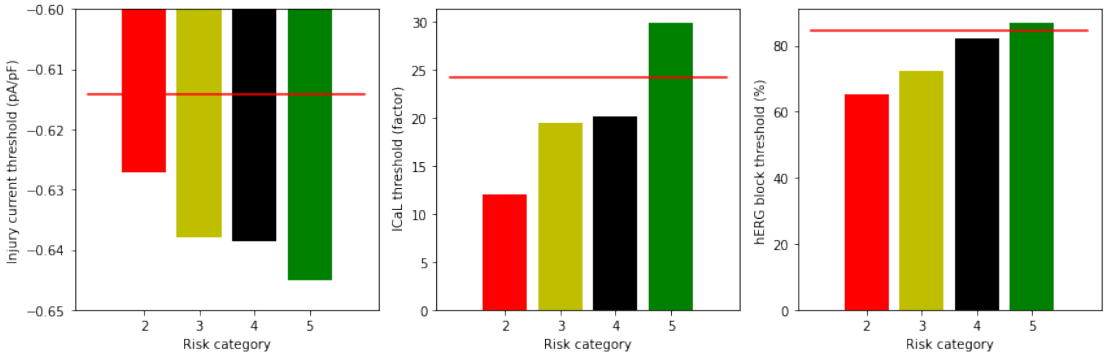

Figure 5.5: The average EAD threshold in each risk categories for the EAD-inducing interventions.

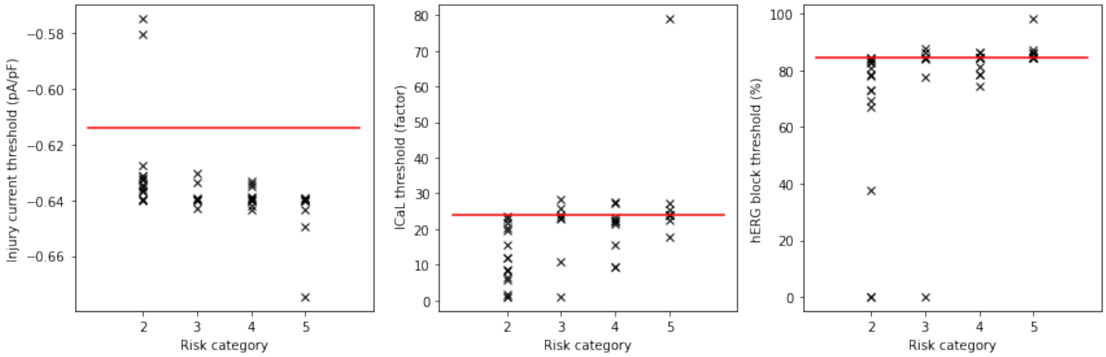

Figure 5.6: Threshold values required to produce an EAD in cell models treated with drugs from each of the four risk categories. Drugs in Category 2 are the most dangerous, and drugs in Category 5 are the least dangerous.

In terms of IC50/Cmax, these are the three strongest hERG blockers in the dataset, and the reactivation of currents shown in Figure 5.7 is, unsurprisingly, broadly the same as the hERG block EAD intervention shown in Figure 5.3 for the first beat - the reduction in the repolarising IKr current leads to slower repolarisation, driven by increased IKs, which allows the ICaL current to reactivate during the plateau phase. The drug effects are applied before the model is run to steady state, meaning that the hERG block is in effect for longer than during the EAD-provoking intervention.

The steady state runner stops either when each pace is identical, or after 10,000 paces if steady state is never reached - in these cases, steady state is never reached, but the simulation begins to show an alternating pattern, with one beat which fails to repolarise followed by a second

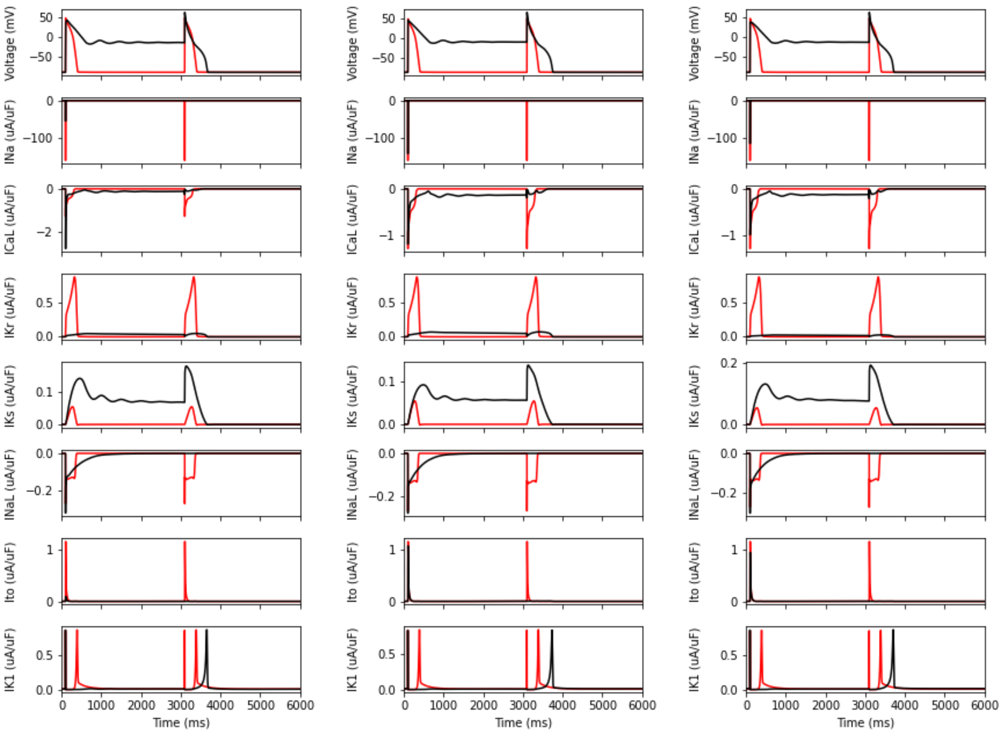

Figure 5.7: Voltage and current graphs for ajmaline (left), quinidine (centre), and thioridazine (right) for two paces, after running to steady state with the Cmax concentration at a cycle length of 3000 ms. The results for the control (un-drugged) model are shown in red.

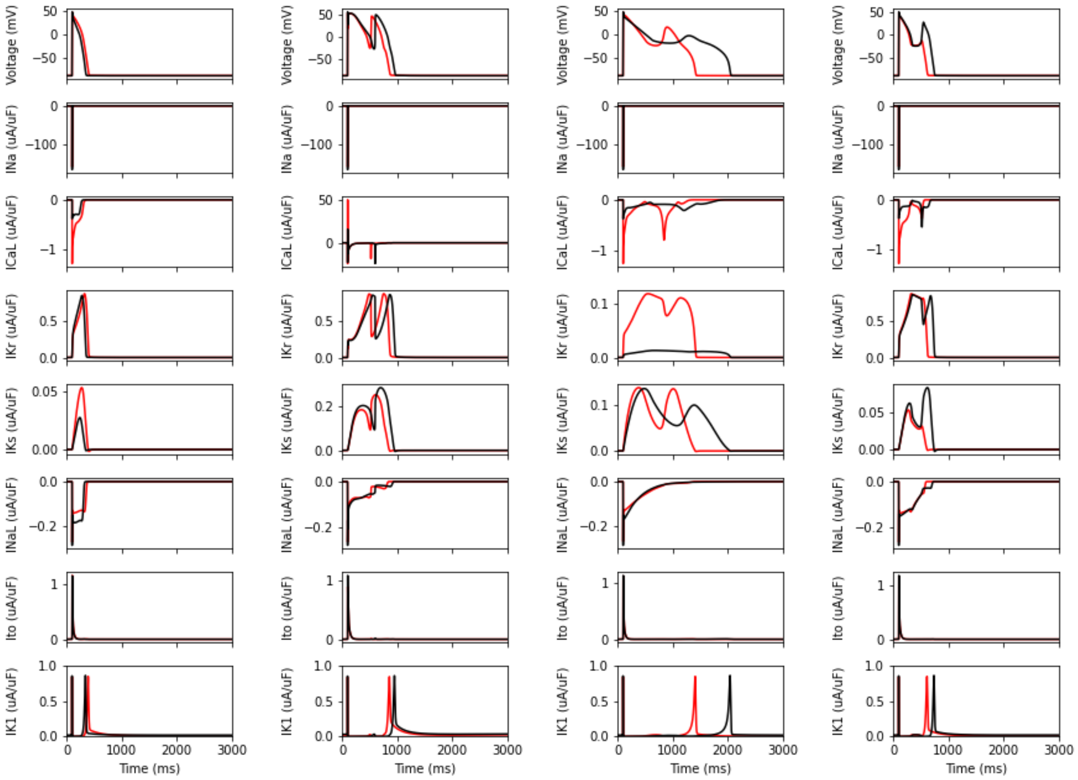

Figure 5.8: Effect of diltiazem on a normal action potential (left), an EAD induced by the L-type calcium increase protocol (middle left), an EAD produced by the hERG block protocol (middle right), and an EAD produced by the injury current intervention (right).

beat with a higher peak and faster IKs-mediated initial repolarisation. INa does not activate during the second beat, and the peak of the action potential is solely driven by the stimulus current and the small increase in ICaL.

Ajmaline is a very strong blocker of Ito, and unlike for the other two drugs, this current barely activates during the first pace. ICaL is greatly increased over control in the first pace for this drug, unlike the other two drugs, despite ajmaline's fairly strong ICaL block activity.

With the exception of thioridazine (Category 3), all of these drugs are in the highest risk Category 2.

After those three drugs, all three of the EAD metrics consistently had the lowest thresholds for the following drugs: azimilide, cisapride, ondansetron, terfenadine, and terodiline. All five of these drugs are in the most dangerous category, Category 2.

Diltiazem is a persistent outlier in all EAD threshold metrics, showing a protective effect against a variety of provocation methods. Figure 5.8 shows a comparison between the EADs provoked in the un-drugged model (red), and EADs provoked when the cell was first treated with diltiazem. Also shown is the effect on diltiazem on a cell with no intervention applied (left). As well as the expected effect on the L-type calcium current, treatment with diltiazem reduced IKs, despite no IKs block being simulated for this drug. The persistent sodium current is increased, and the action potential duration is slightly reduced.

For the ICaL increase EAD metric, diltiazem required an increase of 78.9644x, compared to the control value of 24.1268x. Given that it is the strongest ICaL blocker in the dataset, this is not particularly surprising. However, it also an outlier in the hERG block EAD metric (requiring 98% block, compared to the control threshold of 85%), and the injury current intervention (requiring an injury current of -0.674744 uA/uF, compared to the control value of -0.614075 uA/uF).

While the ICaL EADs show a similar amplitude of ICaL reactivation for both diltiazem and drug-free states, the diltiazem hERG block EADs have only a small amount of L-type calcium current active during the plateau phase, meaning that there needs to be a large reduction in the repolarisation action of hERG in order for the tiny depolarising force of the reduced ICaL current to be able to cause an EAD.

During the injury current intervention, the EAD for diltiazem appears later than for the undrugged cell, and shows a greater level of ICaL reactivation during the EAD, with a concomitant increase in the IKs and IKr currents during the repolarisation phase.

A table of EAD thresholds and other metrics can be found in the supplementary materials.

5.2 Previously suggested metrics

5.2.1 Comparison with risk category

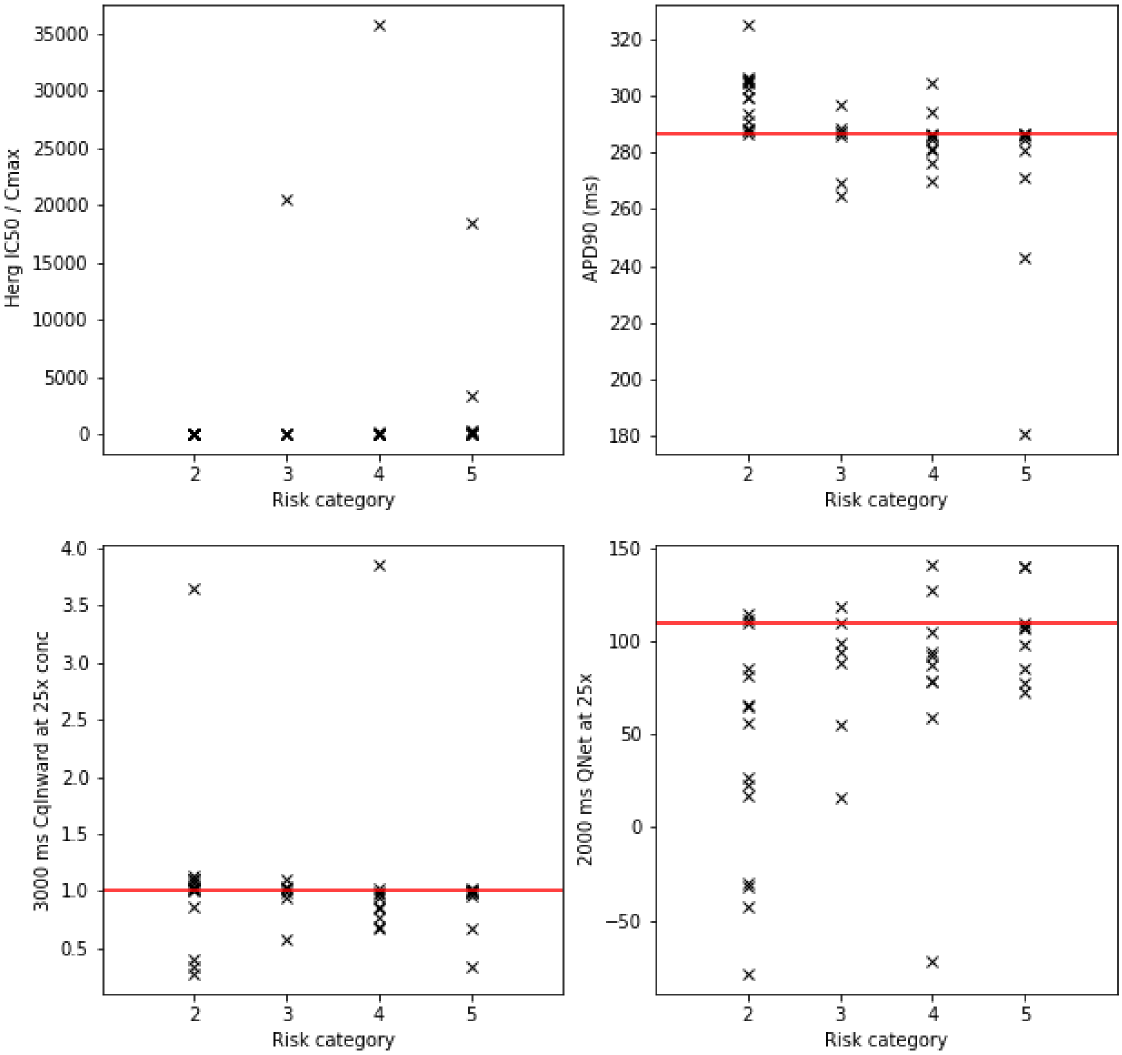

Figure 5.9: Values of 1-dimensional non-EAD based metrics for each drug. The control value is shown as a red horizontal line. Top left: the hERG IC50/Cmax safety margin. Top right: APD90. Bottom left: CqInward calculated at a cycle length of 3000 ms. Bottom right: qNet calculated at a cycle length of 2000 ms.

We calculated the hERG safety margin, APD90, Lancaster-Sobie, qNet and cqInward metrics to compare them to our EAD-based metrics.

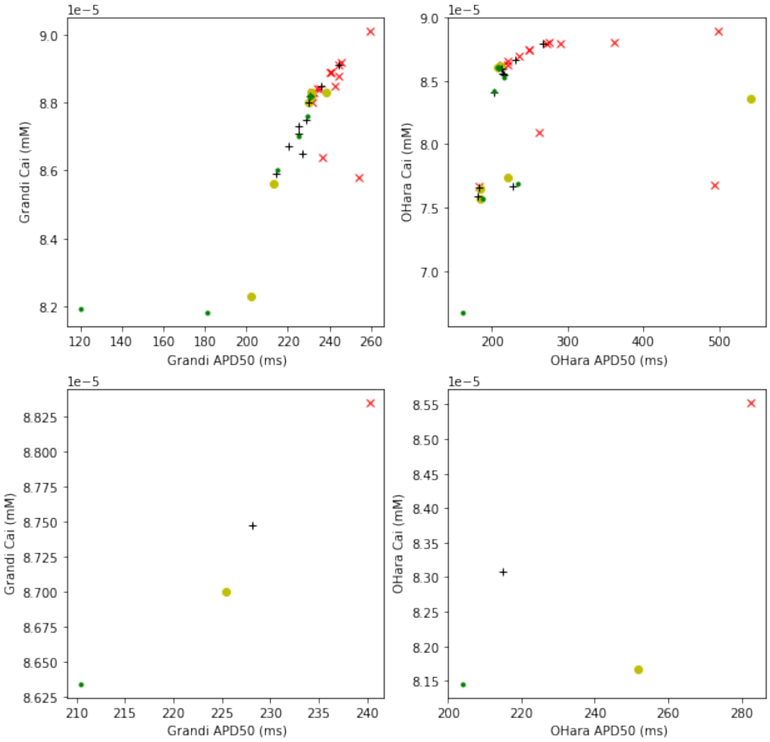

Figure 5.10: Two-dimensional plots of Lancaster and Sobie (2016) metrics in the Grandi (left) and O'Hara (right) models. The APD50 is plotted on the x axis and the diastolic intracellular calcium concentration (Cai) is plotted on the y axis. Risk category is denoted by marker and colour, as shown in the legend: Category 2 is shown by red crosses, Category 3 is shown by yellow circles, Category 4 is shown by black pluses, and Category 5 is shown by green dots. The top row shows all of the drug values, and the bottom row shows the means for each category.

The proposed one-dimensional metrics are plotted in Figure 5.9, and the two-dimensional Lancaster-Sobie metrics are shown in Figure 5.10.

Using our drug dataset, the qNet and cqInward metrics performed much worse than in the original papers, even accounting for the lack of dynamic hERG simulation. The effects of the differences in the input dataset are discussed in Section 6.3.

As with the EAD metrics, no clear separation can be seen between the risk categories for each metric, as shown in Figure 5.9 and Figure 5.10. Unlike the EAD metrics, the means within each group do not change monotonically with risk, as shown in Figure 5.11 and 5.10.

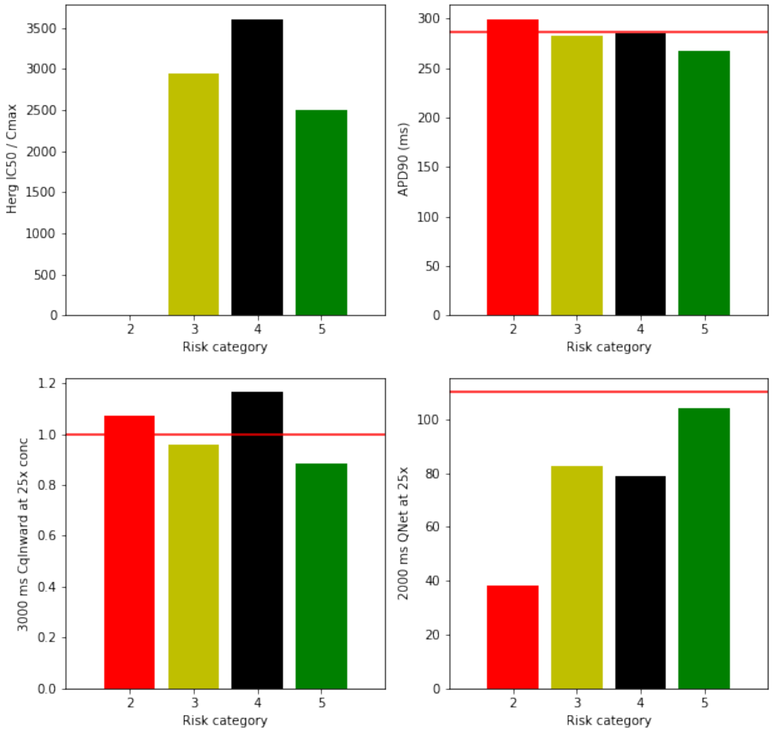

Figure 5.11: Averages of 1-dimensional non-EAD based metrics for each risk category. The control value is shown as a red horizontal line. Top left: the hERG IC50/Cmax safety margin. Top right: APD90. Bottom left: CqInward calculated at a cycle length of 3000 ms. Bottom right: qNet calculated at a cycle length of 2000 ms.

Metric	LDA	SVM
APD90 (ms)	0.82927	0.73171
Combination: Injury current at -20 mV and APD90 (ms)	1.17073	0.78049
Combination: ICaL (factor) and APD90 (ms)	0.95122	0.82927
Combination: hERG block (%) and APD90 (ms)	1.07317	0.85366
ICaL (factor)	0.90244	1.24390
hERG block (%)	0.92683	1.51220
Injury current at -20 mV	0.92683	1.02439
Combination: 2000 ms QNet at 25x and APD90 (ms)	0.97561	1.07317
Herg IC50 / Cmax	0.97561	1.29268
Combination: Grandi APD50 (ms) and Grandi Cai (mM)	1.14634	0.97561
Combination: ICaL (factor) and 3000 ms CqInward at 25x conc	1.07317	1.00000
Combination: ICaL (factor) and 2000 ms QNet at 25x	1.12195	1.02439
3000 ms CqInward at 25x conc	1.04878	1.36585
Combination: Injury current at -20 mV and ICaL (factor)	1.21951	1.04878
Combination: Injury current at -20 mV and 2000 ms QNet at 25x	1.17073	1.04878
2000 ms QNet at 25x	1.07317	1.24390
Combination: Injury current at -20 mV and hERG block (%)	1.09756	1.31707
Combination: 3000 ms CqInward at 25x conc and APD90 (ms)	1.17073	1.26829
Combination: hERG block (%) and ICaL (factor)	1.17073	1.46341
Combination: hERG block (%) and 2000 ms QNet at 25x	1.17073	1.17073
Combination: hERG block (%) and 3000 ms CqInward at 25x conc	1.17073	1.36585
Combination: Injury current at -20 mV and 3000 ms CqInward at 25x conc	1.17073	1.31707
Combination: OHara APD50 (ms) and OHara Cai (mM)	1.21951	1.21951

Table 5.1: Absolute mean error calculated using leave-one-out cross-validation for metrics and combinations of metrics, when the boundaries between categories are chosen by linear discriminant analysis (LDA) or support vector machines (SVM).

5.3 Classification

5.3.1 Comparison between machine learning classification techniques

Calculation of boundaries between categories using linear discriminant analysis (LDA) rather than support vector machines (SVM) produced different levels of accuracy for different types of intervention, as shown in Table 5.1. Broadly, any metric or combination that included APD90 was better classified using SVM, and metrics that solely involved EAD provocation were better classified by LDA.

A persistent problem with classifying EAD metrics by SVM was that the classifier would often only use two groups - the overlap between the moderate-risk categories was too great to be discerned without the extra data and assumptions used in LDA. LDA is a global method, which means it considers all of the dataset when assigning category boundaries, whereas SVM only considers the data points that are the closest to the margins (Hastie, 2009). LDA also makes the assumption that the data within each group are normally distributed. These two features of this classification method mean that boundaries can be found within overlapping data in a way that reflects the underlying distribution of all of the data within each group, rather than just the outliers. However, for a metric or combination of metrics with less overlap, SVM can more cleanly find the boundaries without relying on these assumptions.

Figure 5.12 shows a comparison between the categorisation of APD90 and ICaL EADs by LDA and SVM. The class is chosen for a data point in LDA by choosing the probability density distribution with the highest value at that point. When APD90 is classified using SVM, a good separation between the most and least torsadogenic drugs is possible, allowing for drugs of intermediate risk to be correctly classified. The most dangerous drugs are all correctly classified by this method. However, when LDA is used for classification, the intermediate risk categories are over-represented, and the most dangerous drugs are more often mis-classified as intermediate risk. When the ICaL EAD threshold metric is classified using LDA, the added information provided by considering the overall distribution of each group allows for intermediate risk drugs to be sorted into intermediate categories. However, when the ICaL EAD metric is classified using SVM (right), the boundaries between the most and least dangerous drugs are very close together, so drugs tend to only be sorted into these two categories.

5.3.2 Combinations of metrics

Combining metrics often increased the accuracy of classification over each metric individually. Some combinations of metrics are shown in Figure 5.13, and a greater separation is seen for combinations of metrics than for metrics alone. When combined with APD90, the EAD metrics classified drugs into their risk categories with lower error than when used in isolation.

In terms of mechanisms, combining metrics has the advantage of covering several different use cases. The qNet and CqInward metrics both rely on an increase in drug concentration to 25x Cmax, whereas the APD90 and EAD metrics both use the Cmax concentration. The APD, qNet and CqInward metrics require no modification to the cell model at all other than the application of drug effects, meaning that it reflects the use case of a patient with no underlying abnormality

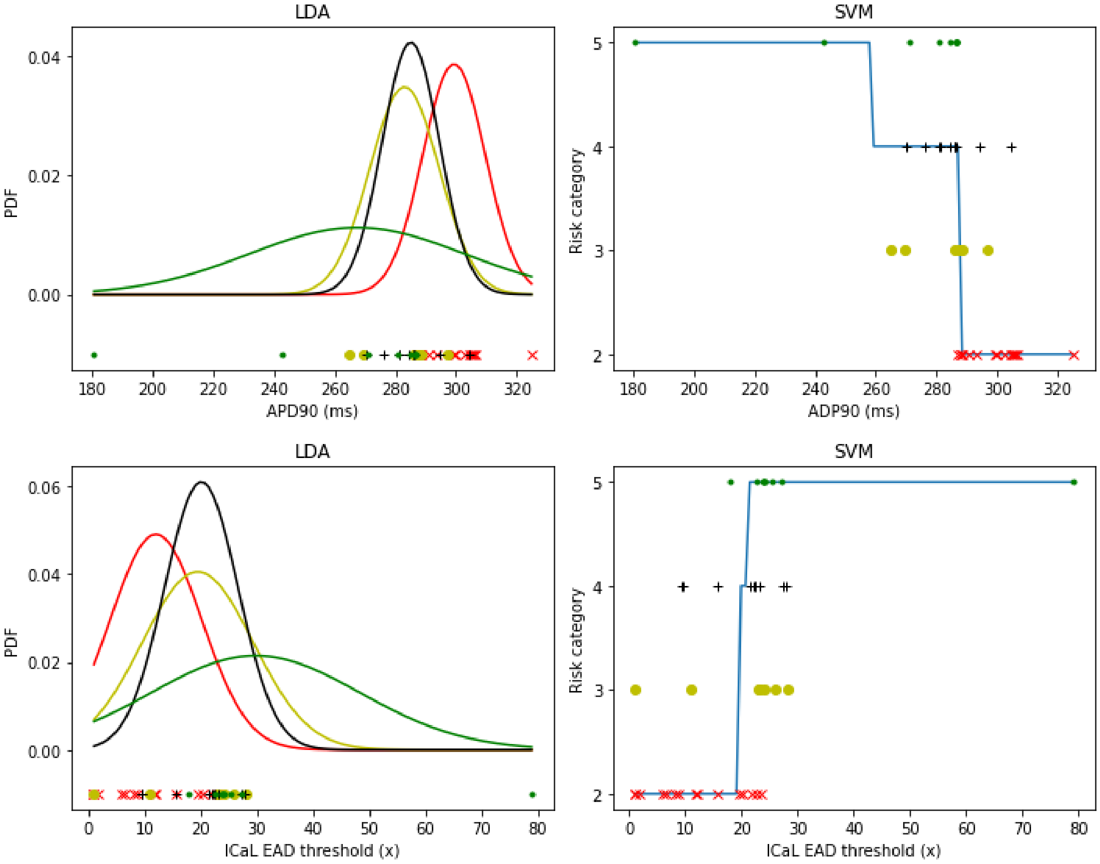

Figure 5.12: Left: probability density distributions assigned by linear discriminant analysis for each risk category for APD90 (top) and the ICaL EAD metric (bottom). The probability density distributions are coloured by risk category: red for category 2, yellow for category 3, black for category 4, and green for category 5. Below the PDFs are plotted the APD or threshold values, also coloured by risk category. Right: the categories calculated using support vector machines for APD90 (top) and ICaL EAD thresholds (bottom). The metric values are plotted against their risk category, and the category assigned by the classifier for each possible value is shown in blue.

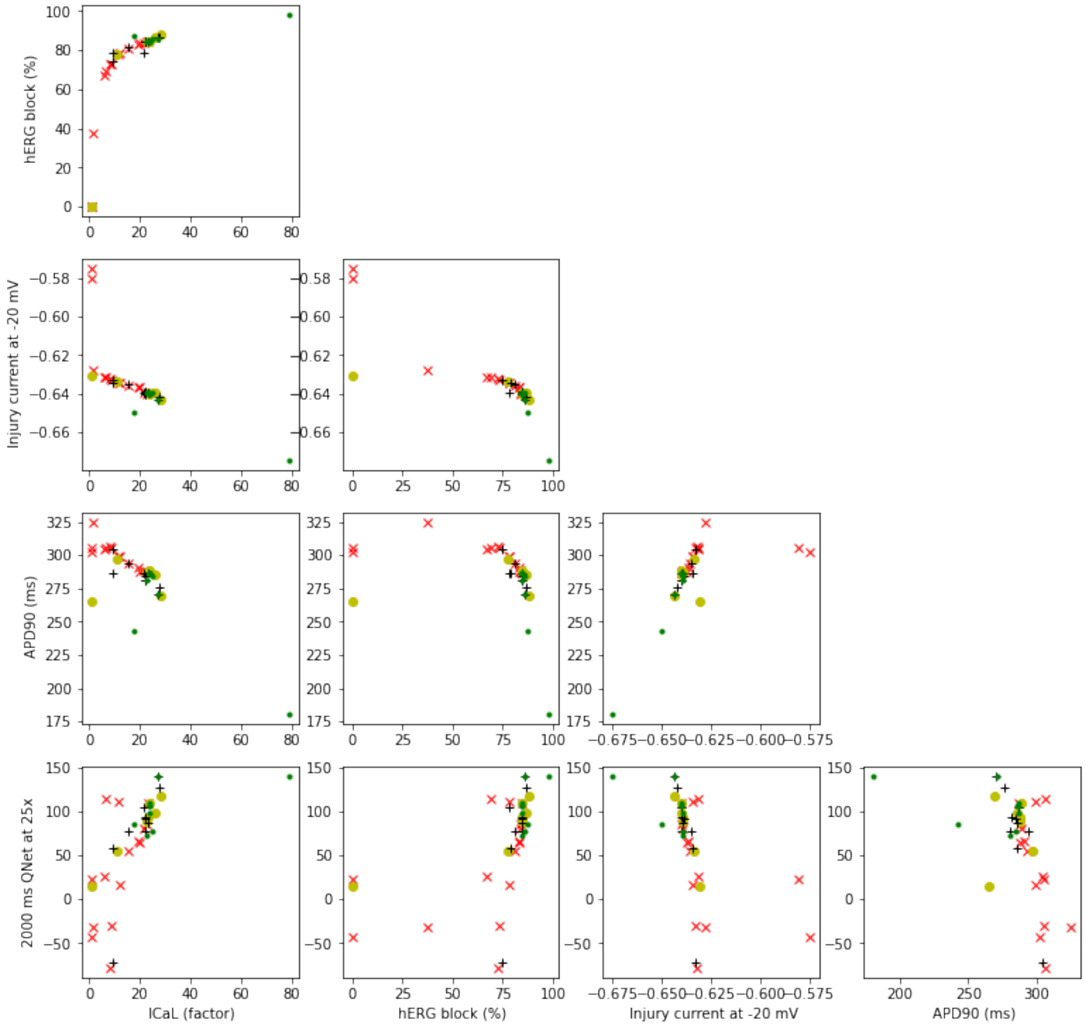

Figure 5.13: A selection of 1-dimensional arrhythmic risk metrics plotted against each other. The risk categories are denoted by marker shape and colour: group 2 (most dangerous) are red ”x”s, group 3 are yellow ”o”s, group 4 are black ”+”s, and group 5 are green dots.

taking a normal dose of the drug. The EAD based metrics simulate pathological states and are explicitly based on repolarisation abnormalities, rather than a surrogate marker such as APD. Therefore, combinations of metrics can cover both normal and abnormal underlying patient physiology, and normal and abnormal drug concentrations. Given the heterogeneity of incidence data used to assign risk categories for medications, with various different patient subgroups and concentrations as part of the input, combining several different possible mechanisms seems like

Metric	Extreme AUC	All AUC
APD90 (ms)	1.00000	0.84211
hERG block (%)	1.00000	0.80861
Injury current at -20 mV	0.93333	0.78947
Herg IC50 / Cmax	0.90370	0.75120
ICaL (factor)	0.94815	0.74641
3000 ms CqInward at 25x conc	0.72593	0.69856
2000 ms QNet at 25x	0.81481	0.69617

Table 5.2: Table of area under curve (AUC) calculations for receiver operator characteristics (ROC) using binary categorisation. "Extreme AUC" are the values calculated categorising only most and least dangerous drugs, whereas "All AUC" show the results from categorising all drugs into either TdP+ (groups 2 and 3) or TdP- (groups 4 and 5)

a logical way to predict the outcomes for the population as a whole.

When the EAD thresholds are plotted against APD90 (Figure 5.13), what can be seen is a greater separation between the most dangerous drugs compared with APD90 alone, particularly for the hERG block EAD protocol.

5.3.3 Binary classification

When the drugs are assigned to two risk categories rather than four, the receiver operator characteristic can be used to assess each metric. There are two ways to reduce the number of risk categories: either by looking at only the most and least dangerous drugs (groups 2 and 5), or by assigning the intermediate risk drugs to the higher and lower groups, so groups 2 and 3 are combined to make the high risk group, and groups 4 and 5 are combined to make the low risk group.

The calculated area under curve (AUC) values are shown in Table 5.2. A perfect classifier would have an AUC of 1, i.e. there would be some value of the metric which would give perfect sensitivity and specificity. Sensitivity is defined as the probability that a TdP+ (dangerous) drug will be classified correctly, and specificity is the probability that a TdP- (safe) drug will be classified correctly. A completely random classifier would be expected to have an AUC of 0.5 (Hastie, 2009).

All metrics are better at classifying only the most and least dangerous drugs, as this is an easier problem. The ROC curves for this classification problem are shown in Figure 5.14. The hERG block EAD thresholds intervention and APD90 are both perfect metrics in this respect,

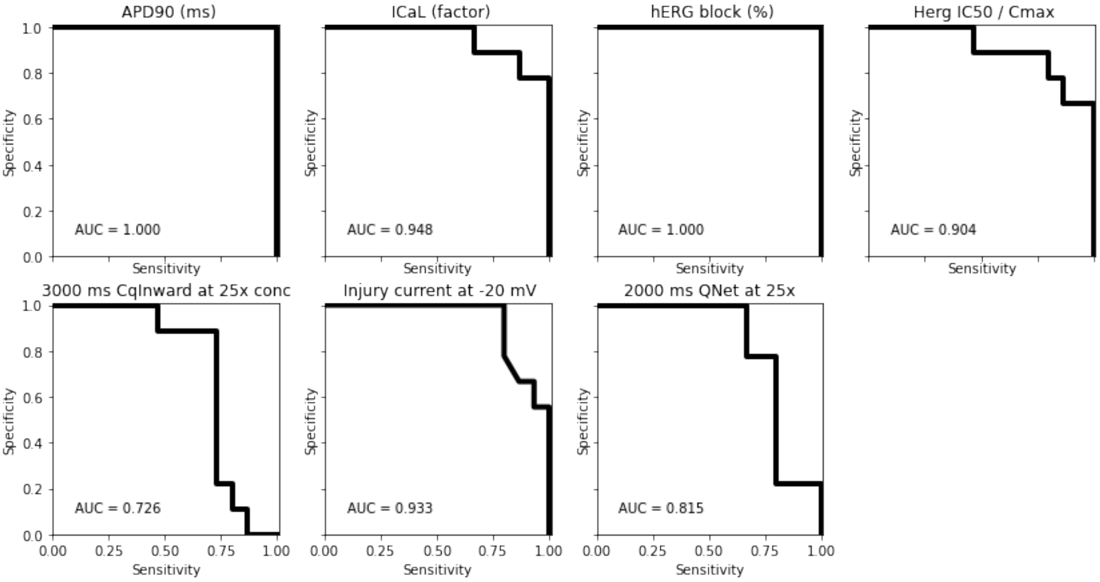

Figure 5.14: Receiver operator characteristic (ROC) curves for proarrhythmic risk metrics, considering only the most dangerous (group 2) and least dangerous (group 5) drugs.

i.e. they have an AUC of 1.

No metrics perform perfectly when separating all of the drugs. The ROC curves for this problem are shown in Figure 5.15. The EAD metrics all consistently preform better than the cqInward and qNet metrics for both types of binary categorisation.

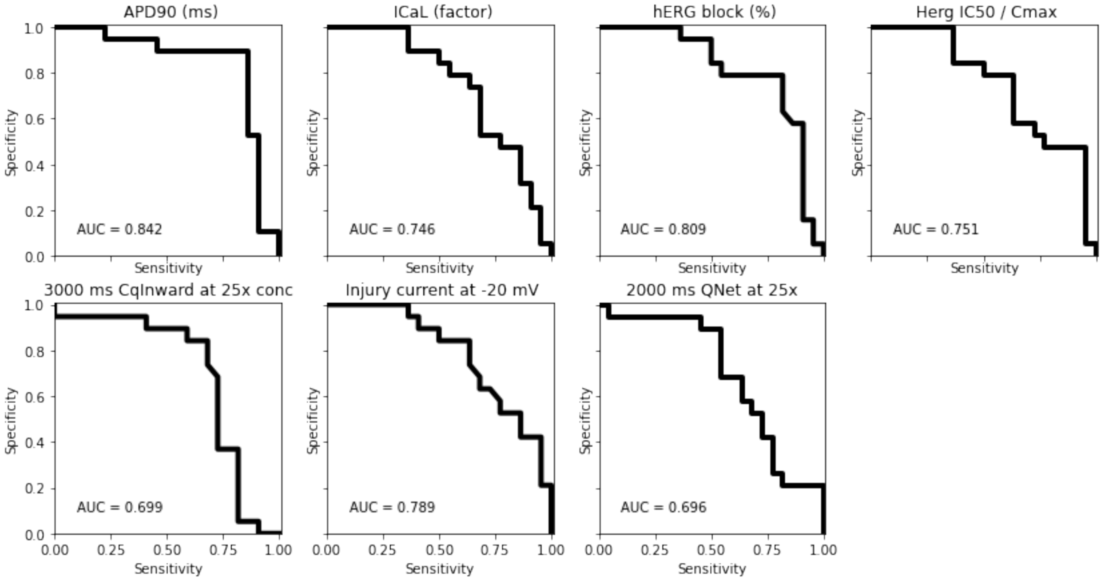

Figure 5.15: Receiver operator characteristic (ROC) curves for proarrhythmic risk metrics, sorting all drugs into two risk categories: TdP+ (groups 2 & 3), and TdP- (groups 4 and 5)

5.4 Modulators of arrhythmic risk

To see whether separation of drugs into risk categories using EAD metrics could be further improved by simulation of pro- and anti-arrhythmic states, we investigated the effects of cycle length, extracellular potassium concentration, drug concentration, and the epi- or endocardial model variants. If drugs in different risk categories respond differently to these modifications, this could improve the classification accuracy.

5.4.1 Effect of cycle length

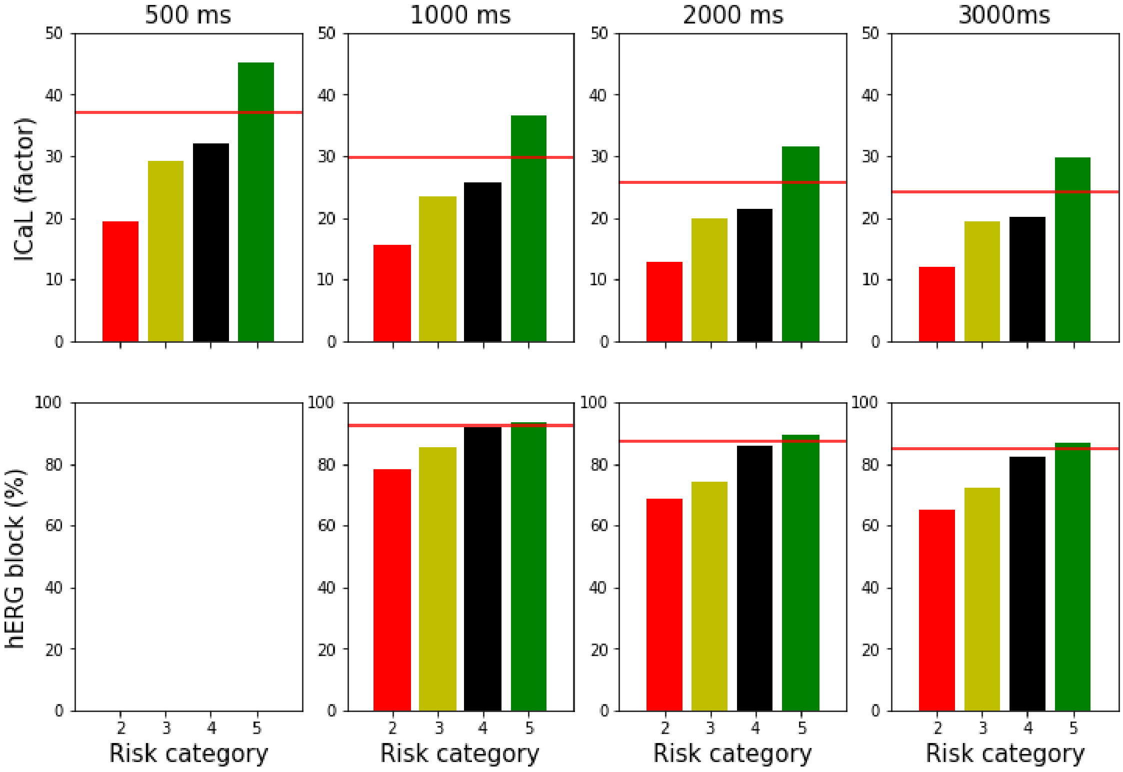

Figure 5.16: Average EAD threshold within each category at 500, 1000, 2000, and 3000 ms cycle lengths. The top row shows the average L-type calcium EAD thresholds (factors), and the bottom row shows the hERG block EAD thresholds (%). No EADs could be provoked using the hERG block EAD protocol at a 500 ms pacing rate. The horizontal red lines show the control value for each pacing rate and intervention.

The average EAD thresholds for each risk category at each cycle length are shown in Figure 5.16. No EADs could be produced from the hERG block EAD protocol with a cycle length

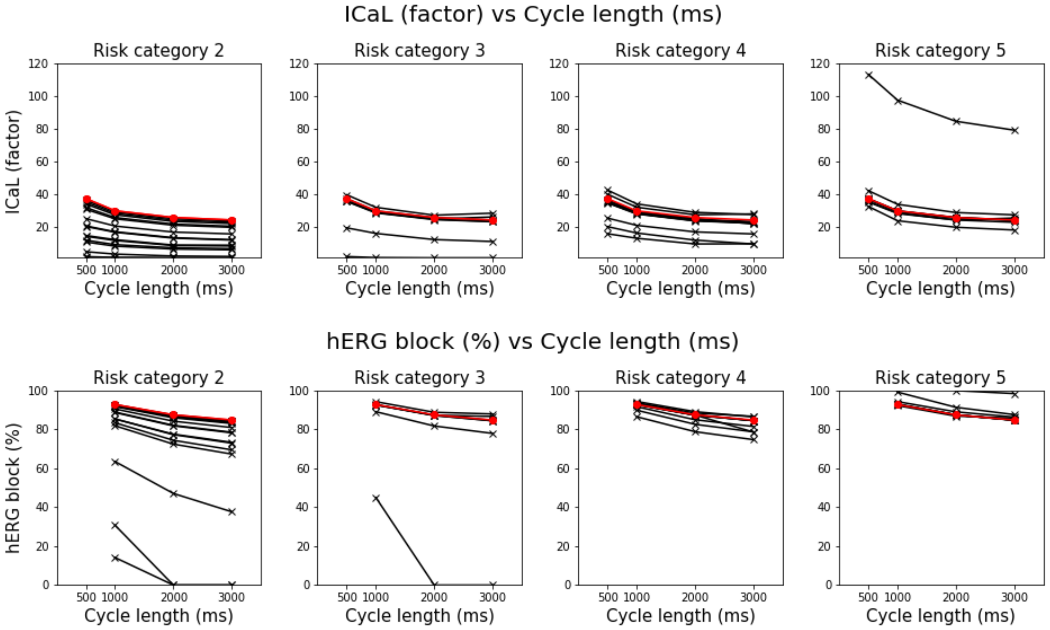

Figure 5.17: EAD thresholds for the four risk categories plotted separately against cycle length. The top row shows the L-type calcium EAD thresholds (factors), and the bottom row shows the hERG block EAD thresholds (percent). The risk categories are shown in order of decreasing risk from left to right.

of 500 ms.

In Figure 5.17, the EAD thresholds for the four risk categories are plotted separately against cycle length. As expected, thresholds generally decreased with increasing cycle length, i.e. at slower pacing rates, the cells are more susceptible to EADs.

The effect of decreasing cycle length on a normal action potential is shown in Figure 5.18. At faster pacing rates, APD is shorter, IKs has a greater role in repolarisation, and INa, INaL, and Ito are decreased.

EAD thresholds for ICaL decreased with cycle length: 37.2x for 500 ms, 29.7x for 1000 ms, 25.6x for 2000 ms, and 24.13x for 3000 ms. The same was true with the hERG block EAD protocol: 92.7% block was required at a cycle length of 1000 ms, 87.4% at 2000 ms, and 84.7% at 3000 ms. For comparison, EADs are plotted at intervention values just above the threshold for each cycle length, compared to the 3000 ms cycle length, in Figures 5.19 and 5.20.

When the cycle length was increased from 2000 to 3000 ms, the leave-one-out cross-validation

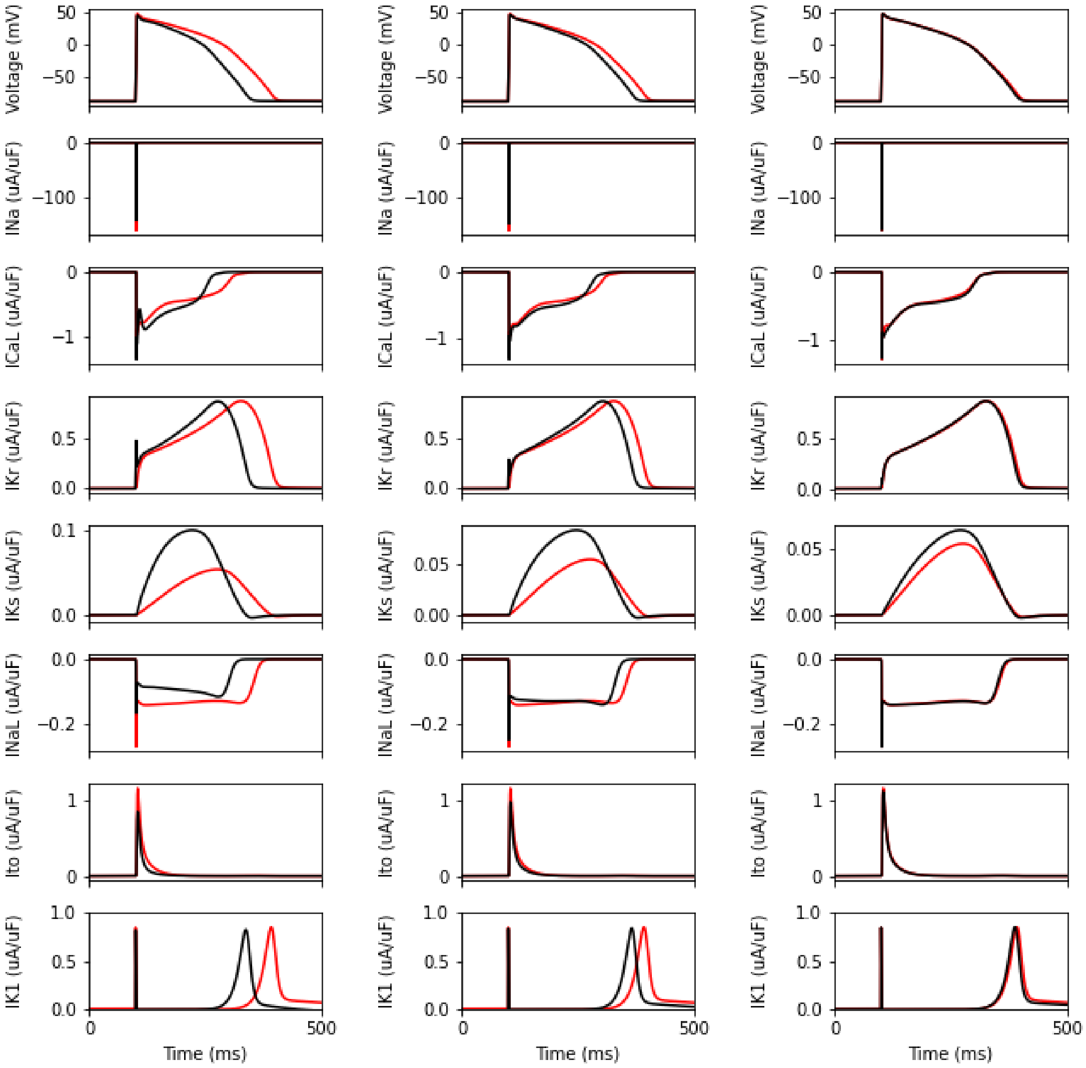

Figure 5.18: Effect on membrane voltage and current reactivation of pacing to steady state at a cycle length of 500 ms (left), 1000 ms (middle) and 2000 ms (right). The pacing rate of 3000 ms is shown on each figure in red.

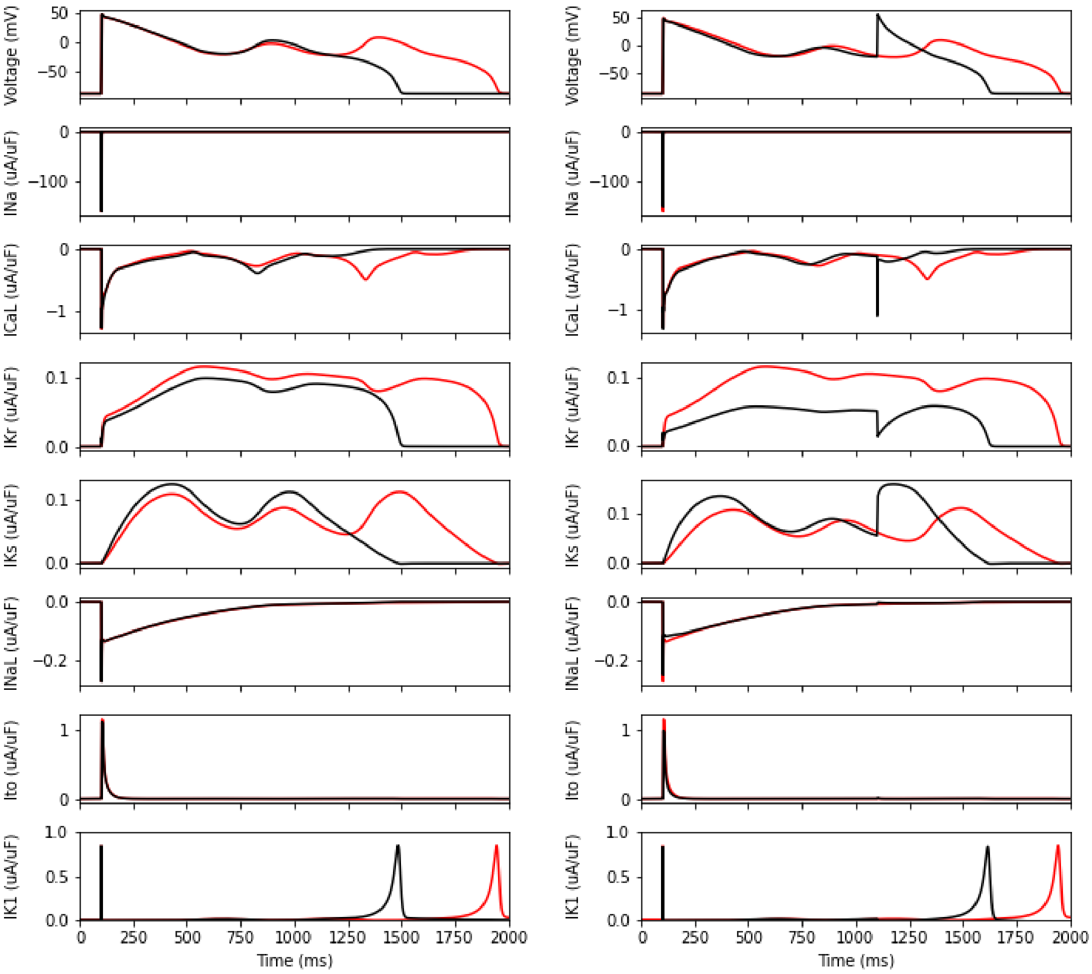

Figure 5.19: EADs caused by block of the hERG potassium current at cycle lengths of 2000 ms (left) and 1000 ms (right). EADs at a cycle length of 3000 ms are shown in red.

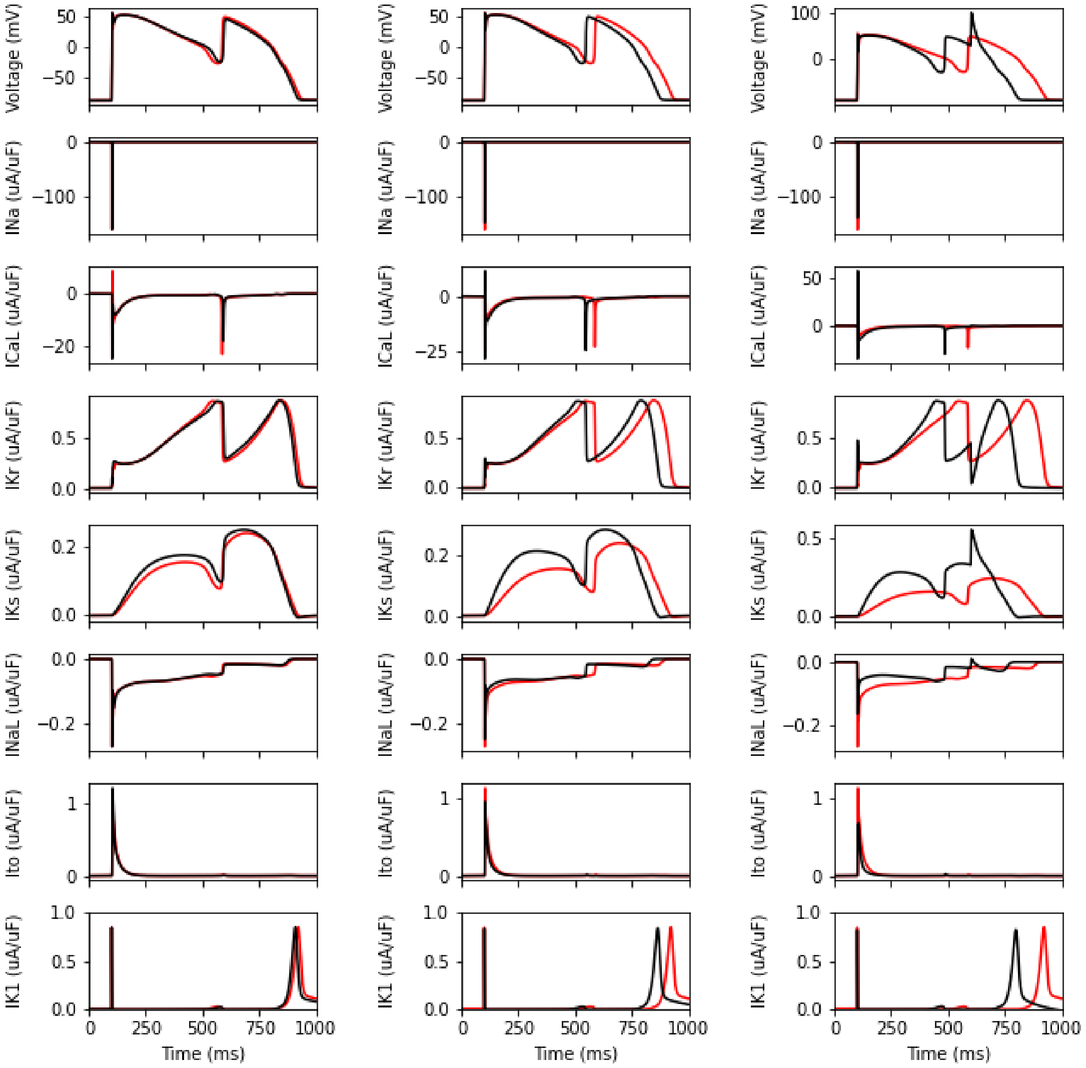

Figure 5.20: EADs caused by increase in ICaL conductance at cycle lengths of 2000 ms (left), 1000 ms (middle), and 500 ms (right).

Cycle length	Metric	LDA error	SVM error
500 ms	ICaL (factor)	0.82927	1.19512
1000 ms	ICaL (factor)	0.80488	1.07317
2000 ms	ICaL (factor)	0.80488	1.19512
3000 ms	ICaL (factor)	0.90244	1.24390
1000 ms	hERG block (%)	1.14634	1.47500
2000 ms	hERG block (%)	0.92683	1.48780
3000 ms	hERG block (%)	0.92683	1.51220

Table 5.3: Leave-one-out cross-validation error measurements for the hERG block and ICaL EAD metrics at cycle lengths of 500, 1000, 2000, and 3000 ms.

results for the ICaL EAD threshold metric changed the classification of mibefradil, nifedipine, and ranolazine to more dangerous classes.

The leave-one-out classification accuracy using LDA and SVM are shown in Table 5.3. The difference in classification between these two methods for the ICaL EAD metric is an interesting example of the suitability of classification methods for different types of problems. Figure 5.21 shows the probability distributions for linear discriminant analysis of the ICaL EAD metric at cycle lengths of 1000 (top) and 3000 (bottom). When LDA is applied to the whole dataset without leave-one-out cross-validation, the distributions for each cycle length tested are functionally identical, leading to precisely the same classification for each cycle length. Leave-one-out cross-validation changes the classification of a few drugs, namely mibefradil, nifedipine, and ranolazine. These are all in the intermediate risk category 4. Conversely, the margins found between groups using SVM are very different depending on cycle length. Linear discriminant analysis is more robust against these small changes around the margins of the risk categories than support vector machines. The difference in classification accuracy at different cycle lengths when leave-one-out cross-validation is applied shows that the distributions within each group for the ICaL metric are less robust to small perturbations when the cycle length is very long than at cycle lengths of 1000 ms and 2000 ms.

LDA is also a more accurate classifier than SVM for the hERG block EAD intervention. There is a greater change in classification accuracy for different cycle lengths in the hERG block EAD protocol. EADs induced by hERG block involve an extreme prolongation of the action potential duration. At shorter cycle lengths, this prolongation is disrupted by the next stimulus, as shown in Figure 5.19, so the cell fails to repolarise.

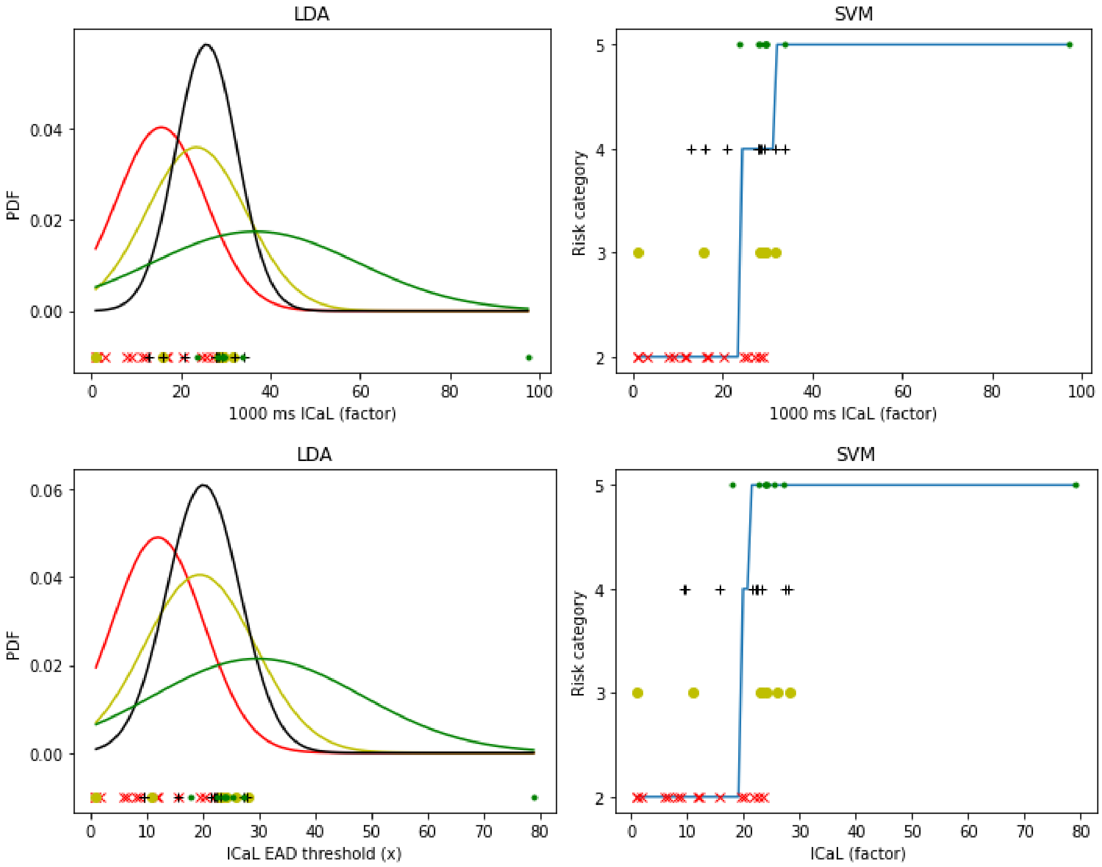

Figure 5.21: Left: probability density distributions assigned by linear discriminant analysis for each risk category for the ICaL metric with a cycle length of 1000 ms (top) and 3000 ms (bottom). The probability density distributions are coloured by risk category: red for category 2, yellow for category 3, black for category 4, and green for category 5. Below the PDFs are plotted the threshold values, also coloured by risk category. Right: the categories calculated using support vector machines for the ICaL EAD metric at a cycle length of 1000 ms (top) and 3000 ms (bottom). The metric values are plotted against their risk category, and the category assigned by the classifier for each possible value is shown in blue.

5.4.2 Effect of extracellular potassium concentration

Hypokalaemia increases action potential duration and lowers the resting membrane voltage whereas hyperkalaemia decreases action potential duration and raises the resting membrane voltage, as shown in Figure 5.22. Hyperkalemia also reduces the peak of the action potential. When extracellular potassium concentration is reduced, the peak of the ICaL current is reduced, IK1 and INa are increased, and the persistent sodium current is increased during the plateau. When extracellular potassium concentration is increased, the INa, Ito, IKs and INaL currents are decreased, and the L-type calcium current is increased. The INa current is much smaller, and the initial depolarisation is instead mediated by ICaL, INa, and the stimulus current, and balanced by the reduction in Ito.

Hyperkalemia had a protective effect against EADs provoked by increasing the L-type calcium current conductance, and a greater increase in conductance was required (28.6842x rather than 24.1268x). Conversely, hypokalemia had the opposite effect, requiring only an increase of 21.2137x to cause an EAD. EADs provoked by this method at different Ko concentrations are shown in Figure 5.23.

The current activation features of the EADs are similar across each value of Ko - ICaL shows a negative current during the initial peak and then reactivates for each EAD, INaL remains active during the prolonged plateau phase, and repolarisation is mediated by activation of IKr, a large increase in IKs, and then a delayed activation of IK1.

During hypokalemia, the magnitude of ICaL activation during the initial depolarisation was smaller, but there was more ICaL during the EADs compared to higher Ko. Conversely, during hyperkalemia, the initial ICaL activation was greater, but it was smaller for the EAD - with normal Ko, the ICaL peaks are about the same as each other.

As with the ICaL conductance increase intervention, an increase in Ko was protective against EADs for the hERG conductance block intervention. During hypokalemia, only a 80.3711% block was required to produce an EAD, compared to 84.6985% for normal Ko, and 91.82739% for double Ko. Unlike in the ICaL increase EAD protocol, the extra peaks of ICaL during the EADs are of similar sizes for each value of Ko, despite the difference during the initial peak. This suggests that the differences in thresholds across extracellular potassium concentrations for the

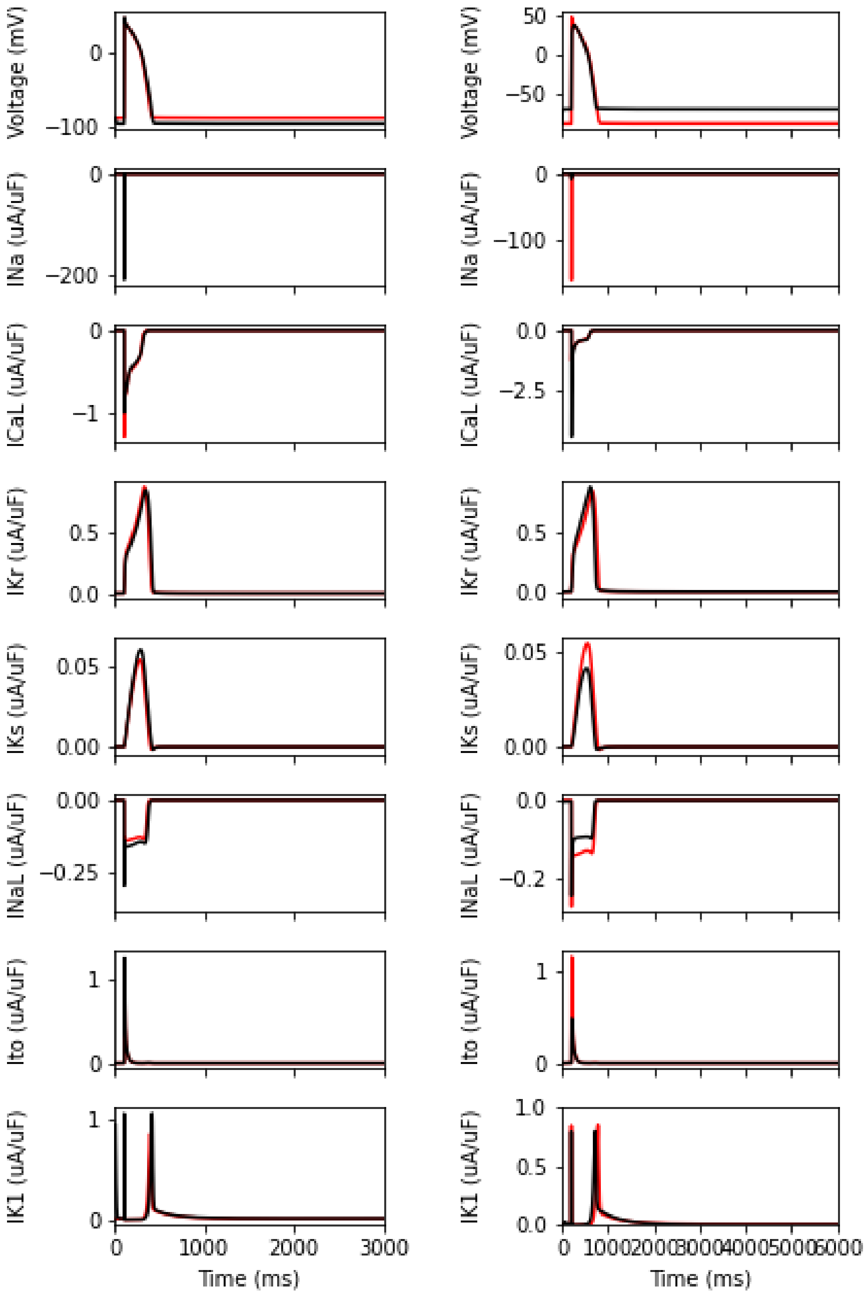

Figure 5.22: Left: effect of reducing extracellular potassium concentration to 75%. Right: effect of increasing extracellular potassium concentration to 200%, both after pacing to steady state with normal Ko and a cycle length of 3000 ms. The control trace is shown in red.

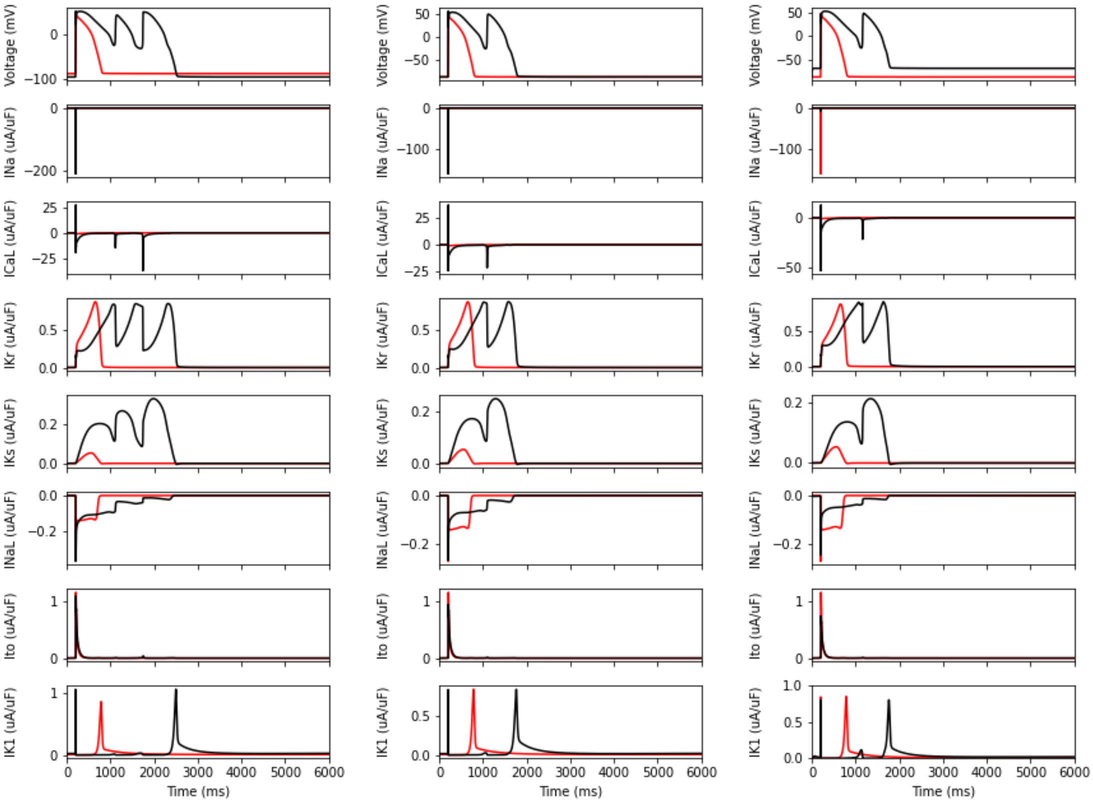

Figure 5.23: EADs provoked by the ICaL increase EAD protocol at 75% (left), 100% (middle), and 200% concentration of extracellular potassium, all after pacing to steady state with normal Ko and a cycle length of 3000 ms. The control trace is shown in red.

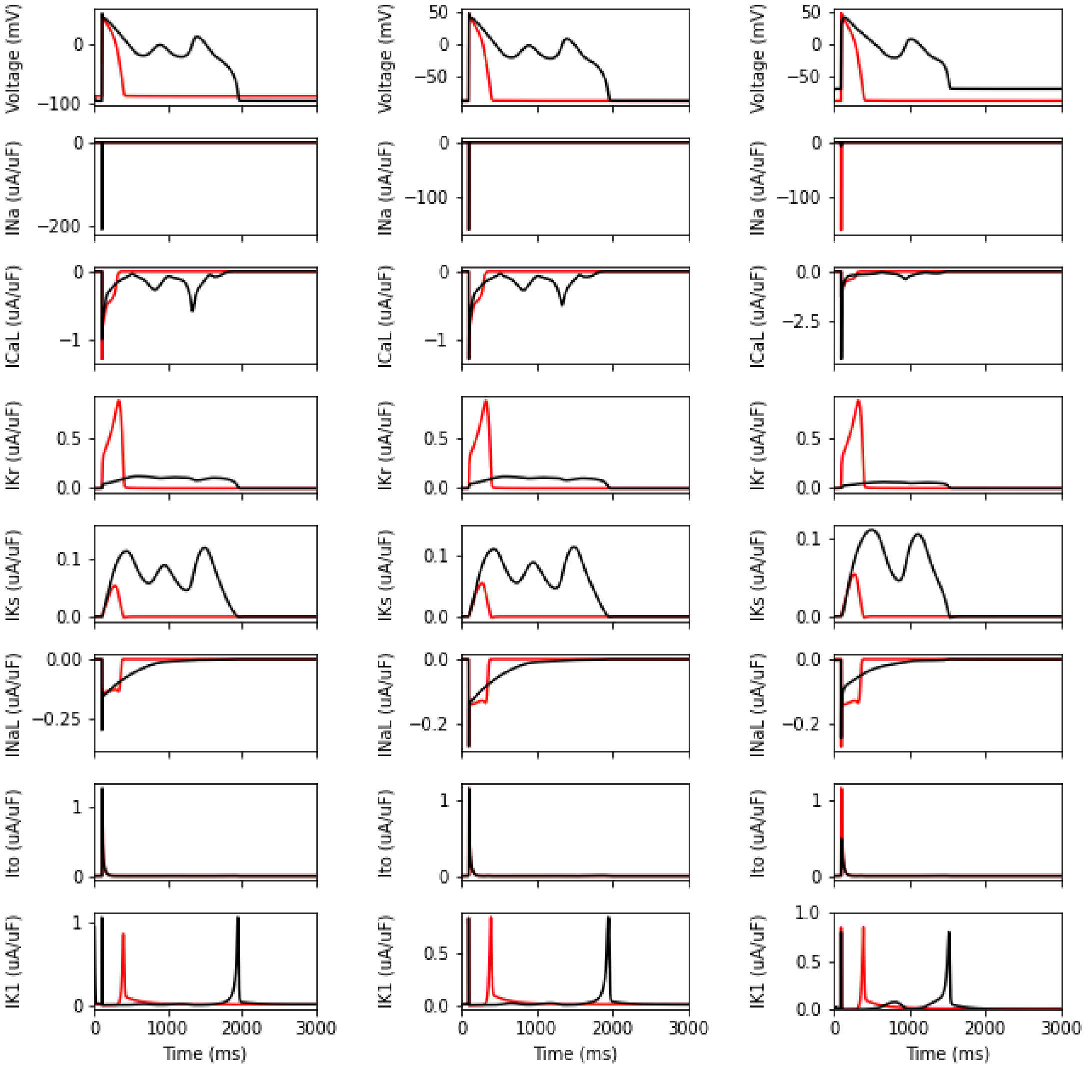

Figure 5.24: EADs provoked by the hERG block EAD protocol at 75% (left), 100% (middle), and 200% concentration of extracellular potassium

hERG block EAD intervention are more strongly related to differences in sodium and potassium currents.

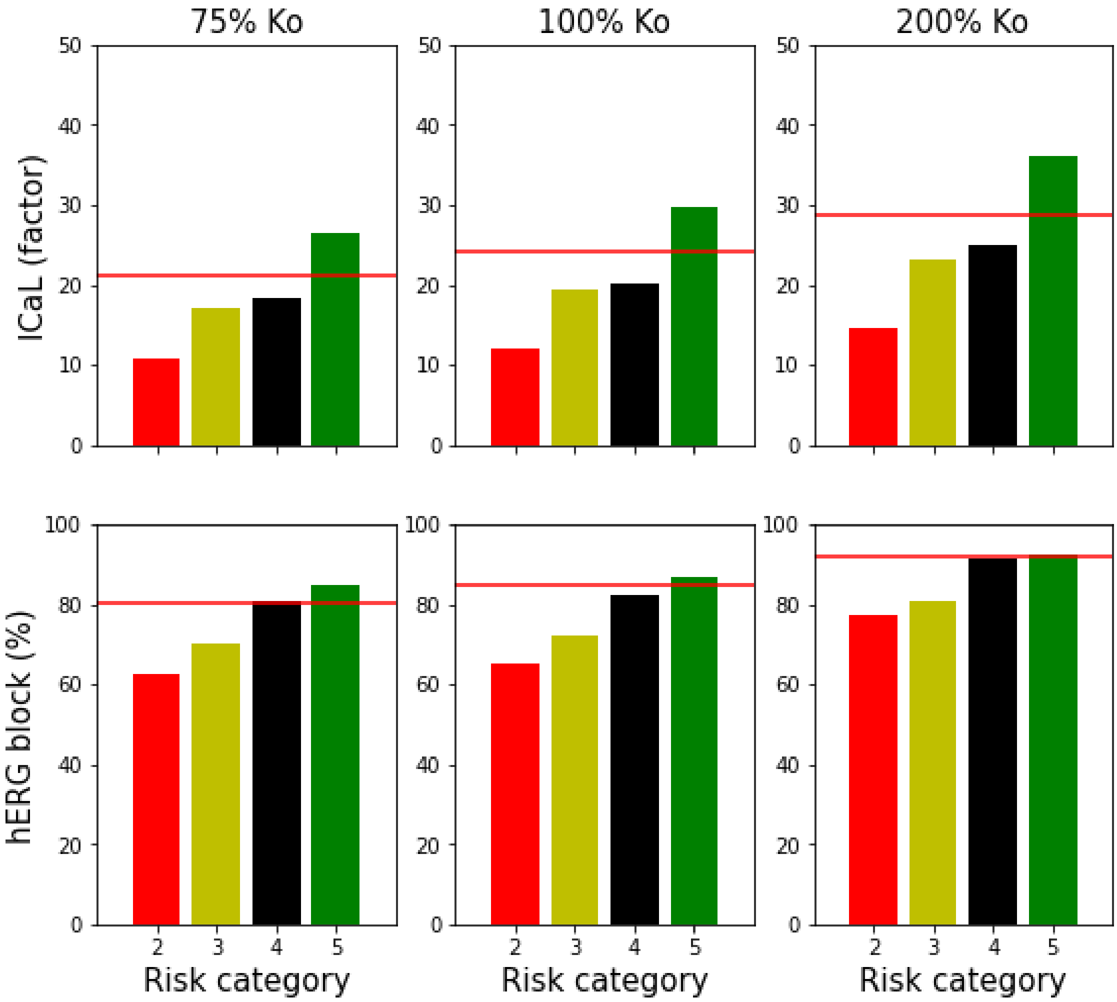

Figure 5.25: Average EAD threshold within each category with extracellular potassium concentration multiplied by $\frac{3}{4}$ (left), 1 (centre), and 2 (right). The top row shows the average L-type calcium EAD thresholds (factors), and the bottom row shows the hERG block EAD thresholds (factors).

The average EAD thresholds for each risk category at each extracellular potassium concentration are shown in Figure 5.25.

In Figure 5.26, the EAD thresholds for the four risk categories are plotted separately against extracellular potassium concentration.

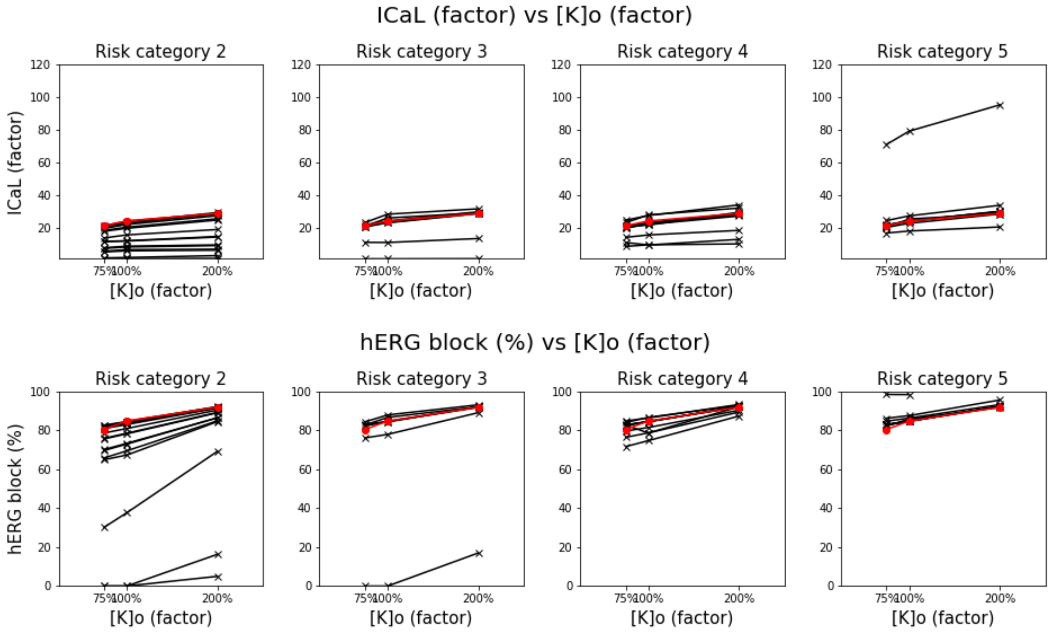

Figure 5.26: The top row shows the average L-type calcium EAD thresholds (factors), and the bottom row shows the hERG block EAD thresholds (percent).

While the leave-one-out accuracy differs with extracellular potassium concentration for the ICaL intervention, when the categories are assigned using the entire dataset, the probability density functions of the different concentrations are, as with the changes in cycle length, functionally identical, and the leave-one-out results show that there is a slight difference in robustness between these methods.

This is not the case for the hERG block EAD protocol, where increasing potassium concentration to 200% decreased the separation between the different risk categories, and made the

[K]o	Metric	LDA	SVM
75%	ICaL (factor)	0.82927	1.09756
100%	ICaL (factor)	0.90244	1.24390
200%	ICaL (factor)	0.85366	1.21951
75%	hERG block (%)	0.92683	1.12195
100%	hERG block (%)	0.92683	1.51220
200%	hERG block (%)	1.21951	1.27500

Table 5.4: Leave-one-out cross-validation errors for linear discriminant analysis (LDA) and support vector machines (SVM) for each concentration of extracellular potassium.

classification accuracy worse.

5.4.3 Effect of drug concentration

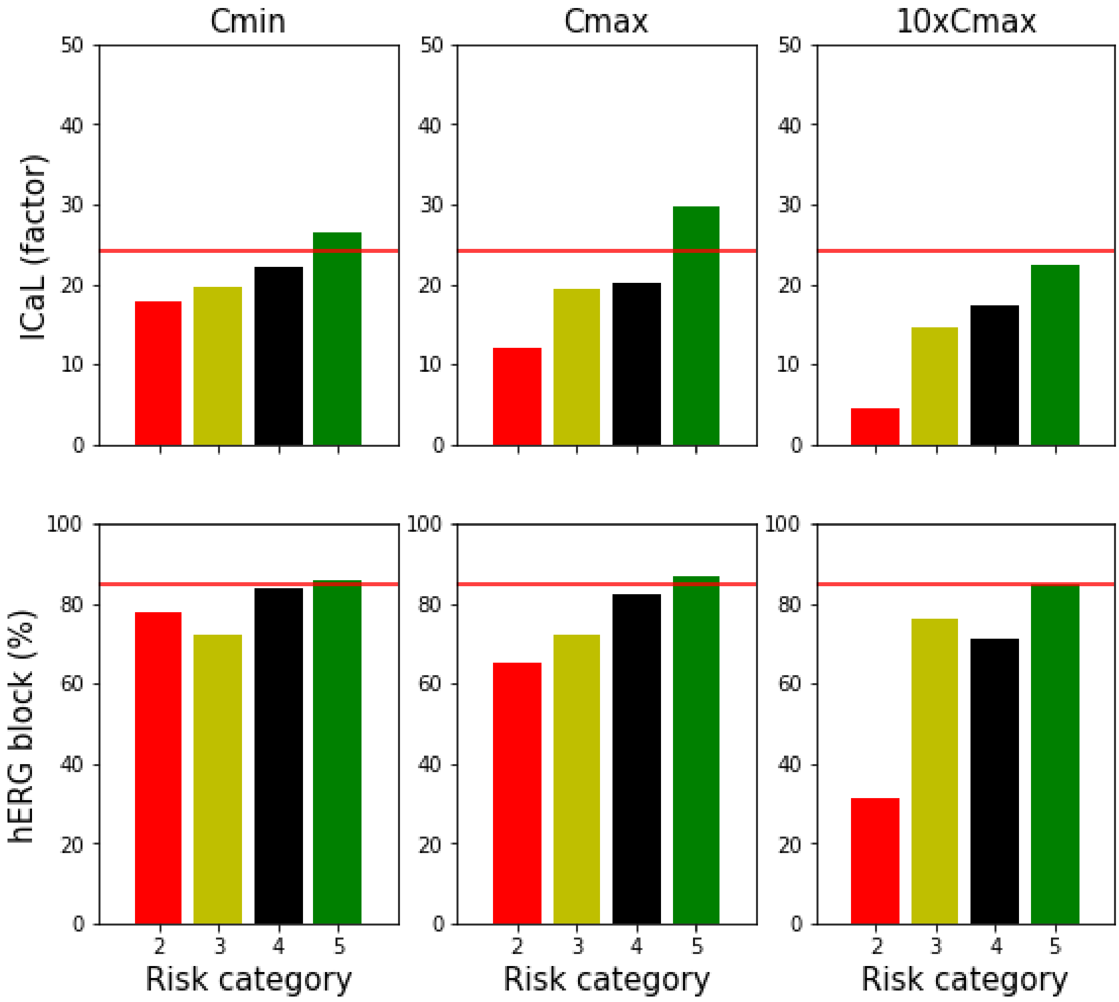

Figure 5.27: Average EAD threshold within each category at $\mathrm{EFTPC}_{\mathrm{min}}$, $\mathrm{EFTPC}_{\mathrm{max}}$ and 10 × $\mathrm{EFTPC}_{\mathrm{max}}$. The top row shows the average L-type calcium EAD thresholds (factors), and the bottom row shows the hERG block EAD thresholds (%).

The difference between $\mathrm{EFTPC}_{\mathrm{min}}$ and $\mathrm{EFTPC}_{\mathrm{max}}$ varies enormously depending on the medication. For example, $\mathrm{EFTPC}_{\mathrm{min}}$ for ajmaline is 263 times lower than its $\mathrm{EFTPC}_{\mathrm{max}}$, whereas for pentamidine the maximum concentration is only 1.25 times higher than the minimum. In Figure 5.29, the EAD thresholds at $\mathrm{EFTPC}_{\mathrm{min}}$ are shown as a percentage of $\mathrm{EFTPC}_{\mathrm{max}}$. This removes some of the crossing-over features seen in Figure 5.28.

It seems intuitive that torsadogenic risk would be increased by increasing doses of medications,

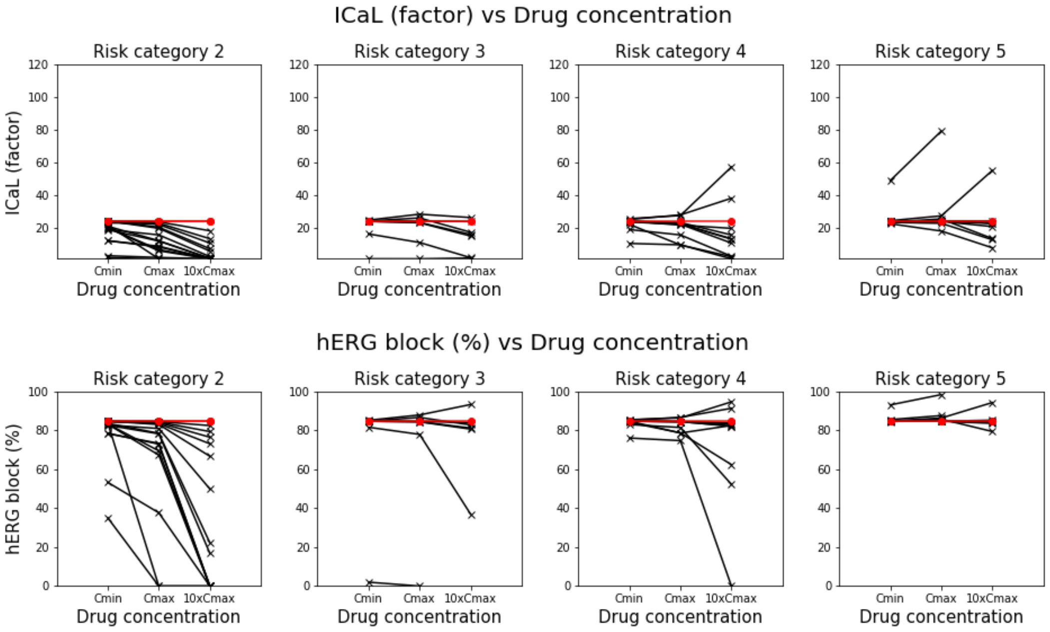

Figure 5.28: The top row shows the L-type calcium EAD thresholds (factors), and the bottom row shows the hERG block EAD thresholds (percent).

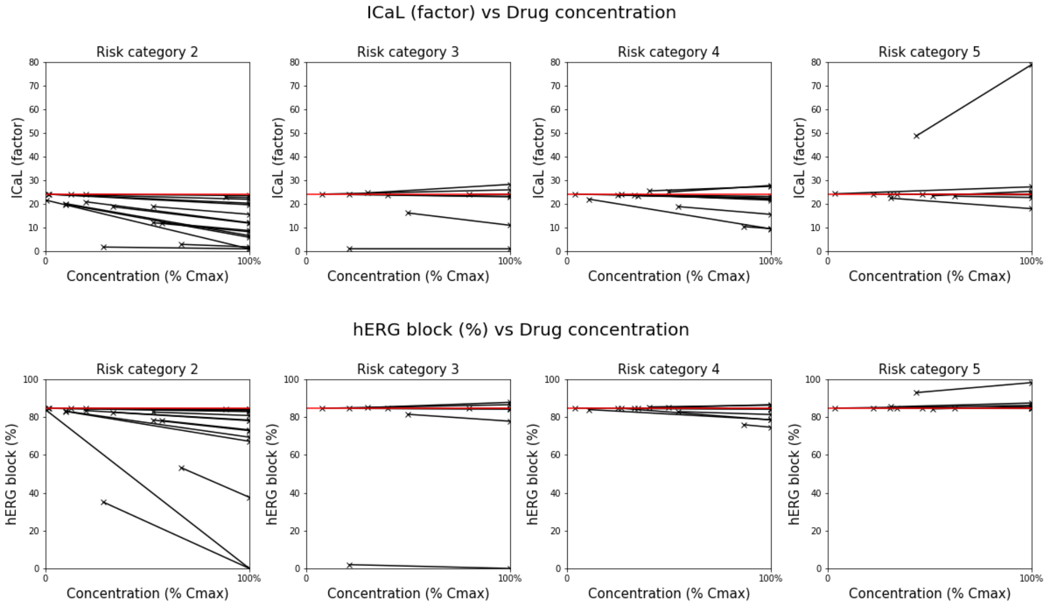

Figure 5.29: The top row shows the L-type calcium EAD thresholds (factors), and the bottom row shows the hERG block EAD thresholds (percent).

Concentration	Metric	LDA	SVM
Cmin	ICaL (factor)	1.04878	1.17073
Cmax	ICaL (factor)	0.90244	1.24390
10xCmax	ICaL (factor)	0.97561	1.10000
Cmin	hERG block (%)	1.34146	1.31707
Cmax	hERG block (%)	0.92683	1.51220
10xCmax	hERG block (%)	1.00000	0.81579

Table 5.5: Leave-one-out errors in classification at different drug concentrations using linear discriminant analysis (LDA) and support vector machines (SVM)

and most drugs did have higher EAD thresholds at lower concentrations and lower thresholds at higher concentrations. However, there were several exceptions, particularly for drugs of low torsadogenic risk. For every intervention, the drugs diltiazem, mibefradil, nifedipine, and nitrendipine were protective against EADs at higher concentrations. All of these drugs block the depolarising currents (such as fast sodium or L-type calcium) much more strongly than they block the hERG current. In the case of diltiazem, this protective effect was so strong that no EADs could be provoked at the 10xCmax concentration. Thioridazine shows an interesting response to concentration: raising the concentration to Cmin to Cmax makes the cell more vulnerable to EADs, but raising the concentration further to 10xCmax has a protective effect against EADs. While thioridazine is a strong hERG blocker, it is also a strong blocker of depolarising currents. At high enough concentrations this opposing effect is sufficient to reverse the EAD-inducing effects of the hERG block. This suggests that an effective strategy for decreasing the torsadogenic risk posed to patients by thioridazine might be to increase, rather than decrease, the dosage - although this would have to be balanced by consideration of other side-effects of the medication.

5.4.4 Effect of endo- or epicardial model

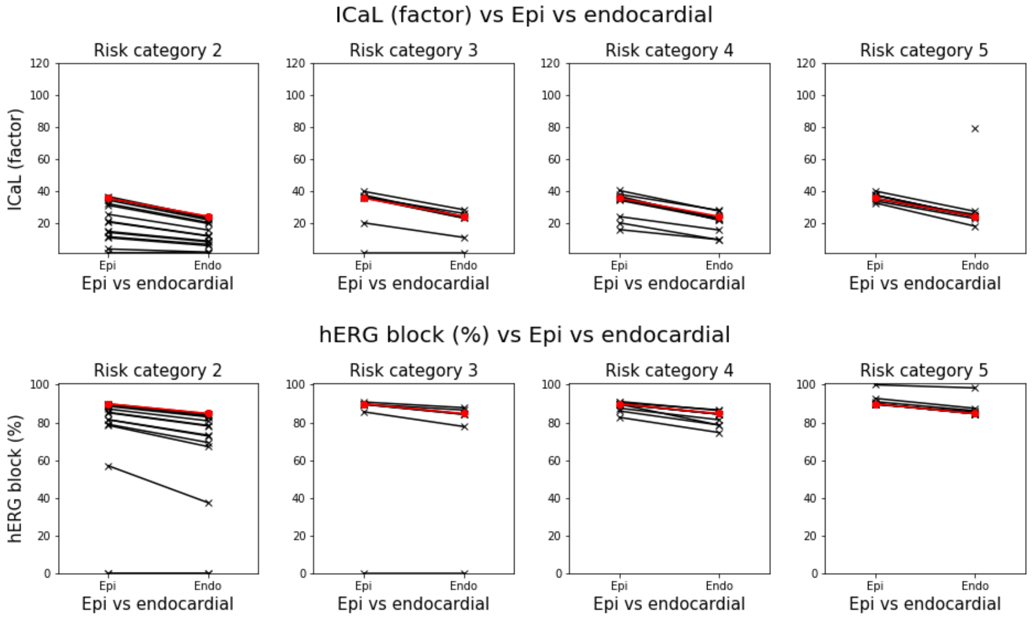

Figure 5.30: The top row shows the average L-type calcium EAD thresholds (factors), and the bottom row shows the hERG block EAD thresholds (percent).

The difference in current activation for the epi- and endocardial model variants is shown in Figure 5.32. The action potential duration is shorter in the epicardial model, and the repolarising IKs, IKr, and IK1 currents are increased. The balance of depolarising currents during the plateau phase is different - ICaL is increased, and INaL is decreased. For both interventions, a greater arrhythmic insult was required in order to induce an EAD under control (un-drugged) conditions. The ICaL increase EAD protocol required the conductance to be increased by a factor of 35.42x, as opposed to 24.13x for the endocardial model. This is not simply due to differences in conductance of this current in the model - the threshold increases nearly 1.5x, whereas the ICaL conductance is increased 1.2x in the epicardial model. The hERG block EAD protocol required a block of 89.8%, compared to 84.7% for the endocardial model.

For comparison, EADs provoked by each method at just above the threshold values are shown in Figure 5.32. The action potential is still shorter in the epicardial model, even when the repolarisation reserve is reduced by either increasing ICaL or decreasing hERG. The EADs

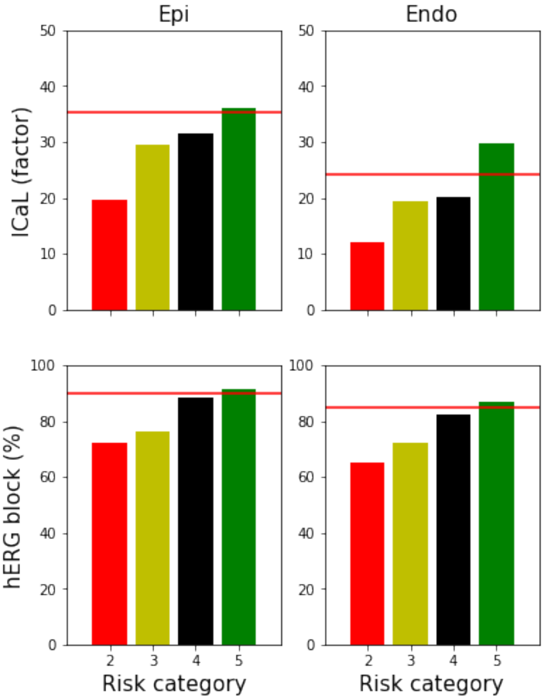

Figure 5.31: Average EAD threshold within each category for the epi- and endocardial model variants. The top row shows the average L-type calcium EAD thresholds (factors), and the bottom row shows the hERG block EAD thresholds (factors).

involve a greater contribution from the ICaL current and a smaller contribution from the INaL current in the epicardial cells for both interventions. The repolarising IKs current has a greater role in repolarisation in the epicardial cell for the hERG block protocol than in the endocardial cell.

EAD thresholds were almost universally lower for the endocardial cell model than for the epicardial cell model. i.e. the endocardial cell model was more prone to EADs and required less provocation, as shown in Figure 5.30.

However, the classifications did change; for the hERG block EAD metric, chlorpromazine (category 3) and cibenzoline (category 5) were both assigned category 4 when LDA was used on the thresholds from the endocardial model, but they were both assigned to category 5 when the epicardial thresholds were used.

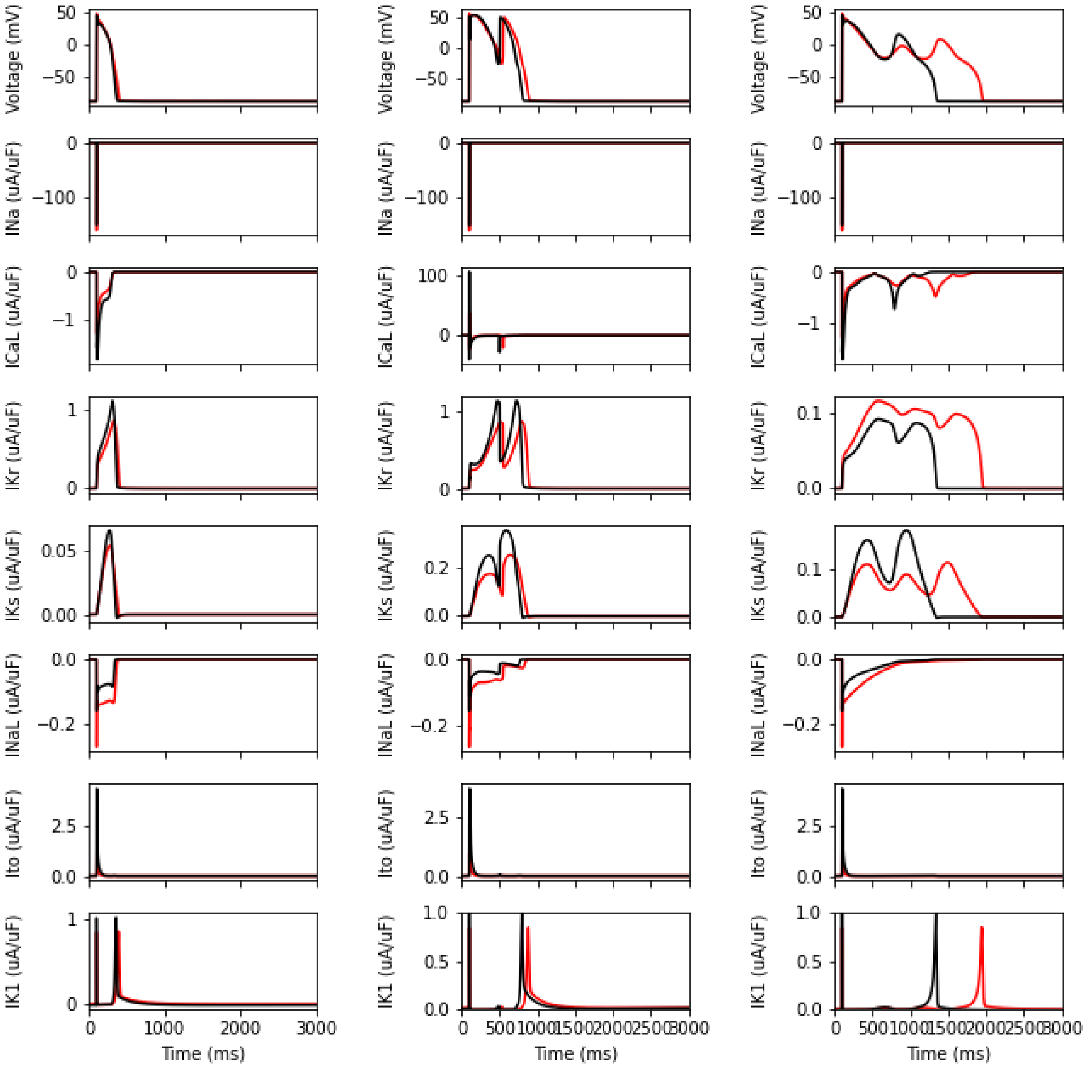

Figure 5.32: Difference in membrane voltage and current activation in the endocardial (red) and epicardial (black) model variants, for a normal pace (left), an ICaL-induced EAD (middle), and a hERG block-induced EAD (right). The ICaL EADs were induced by increasing the conductance 24.13x (red) and 35.42x (black), and the IKr EADs were induced by 84.7% block (red) and 89.8% block (black).

Cell type	Metric	LDA	SVM
Epi	ICaL (factor)	1.09756	1.07500
Endo	ICaL (factor)	0.90244	1.24390
Epi	hERG block (%)	0.92683	1.31707
Endo	hERG block (%)	0.92683	1.51220

Metric	Modification	LDA	SVM
APD90 (ms)		0.82927	0.73171
ICaL (factor)	CL: 2000 ms	0.80488	1.19512
ICaL (factor)	CL: 1000 ms	0.80488	1.07317
hERG block (%)	Conc: 10xCmax	1.00000	0.81579
ICaL (factor)	3/4 ko	0.82927	1.09756
ICaL (factor)	CL: 500 ms	0.82927	1.19512
ICaL (factor)	2Ko	0.85366	1.21951
ICaL (factor)	CL: 3000 ms	0.90244	1.24390
Injury current at -20 mV		0.92683	1.02439
hERG block (%)	3/4 ko	0.92683	1.12195
hERG block (%)	CL: 2000 ms	0.92683	1.48780
hERG block (%)	Cell type: epi	0.92683	1.31707
hERG block (%)	CL: 3000 ms	0.92683	1.51220
Herg IC50 / Cmax		0.97561	1.29268
ICaL (factor)	Conc: 10xCmax	0.97561	1.10000
ICaL (factor)	Conc: Cmin	1.04878	1.17073
CqInward at 25x conc		1.04878	1.36585
QNet at 25x		1.07317	1.24390
ICaL (factor)	Cell type: epi	1.09756	1.07500
hERG block (%)	CL: 1000 ms	1.14634	1.47500
hERG block (%)	2Ko	1.21951	1.27500
hERG block (%)	Conc: Cmin	1.34146	1.31707

Table 5.7: Overall comparison between 1D classifiers. The original simulations have a white background, those with modified cycle length are in yellow, modified drug concentrations are in blue, modified extracellular potassium concentrations are in red and the epicardial cell model results are in green.

5.5 Overall accuracy comparison

The accuracy of each 1D classifier we have considered is shown in Table 5.7. APD90 remains the most accurate metric, but the accuracy of the EAD classifiers was improved by adding pro- and anti-arrhythmic modifiers. In particular, leave-one-out cross-validation shows that the stability of the ICaL EAD metric was improved by using shorter cycle lengths and modifying the extracellular potassium concentration, whereas the hERG block EAD metric was only improved by a small reduction in cycle length to 2000 ms, decreasing the extracellular potassium concentration, and using a higher concentration of the drugs.

5.6 Conclusion

For all of the EAD-provoking interventions we have investigated here, the primary mechanism behind the EAD was the reactivation of the ICaL current, and not INa current. The INaL current was reduced during the plateau phase for the ICaL EAD intervention and the hERG block intervention, but not for the injury current intervention. The mechanism of repolarisation after the EAD differed - in the injury current and ICaL increase interventions, IKr and IKs were increased, but in the hERG block intervention, only IKs was increased. Unlike the other metrics we considered, the means of each EAD-inducing intervention threshold increased monotonically with risk category when drug effects were applied. Linear discriminant analysis outperformed support vector machines for assigning drugs to categories based on EADs. The EAD-based metrics outperformed every other metric apart from APD90 when using a four- or two-category system, as verified by leave-one-out cross-validation and receiver operator characteristic curves. Accuracy of classification was improved by combining metrics, particularly when the EAD metrics were combined with APD90. Leave-one-out cross-validation shows that the robustness of the ICaL increase EAD protocol can be improved by using a shorter cycle length or changing the extracellular potassium concentration. The good performance of the EAD-based classifiers compared to other metrics in the literature shows that they have value as arrhythmic risk metrics.

Chapter 6

Discussion

Contents

6.1 Key findings

In this thesis, we have developed a metric for the prediction of pro-arrhythmic risk that outperforms other metrics such as the Lancaster and Sobie (2016) two-dimensional metric, the Li et al. (2017) cqInward metric, the Dutta et al. (2017) qNet metric, and the Redfern et al. (2003) hERG/Cmax safety margin, when compared using either leave-one-out cross-validation or receiver operator characteristic curves. The improved performance was consistent over a four-category risk stratification system, a binary system considering only the extremes of risk, and a binary system considering all of the drugs. The EAD metrics were also able to correctly classify drugs which prolong the QT interval but do not cause Torsades de Pointes, which is an improvement over the Mirams et al. (2011) APD90 metric. We also investigated the performance of two machine learning methods for the calculation of boundaries between risk classes and discovered that linear discriminant analysis (LDA) is more suitable for separating metrics with large overlaps and extreme outliers than support vector machines (SVM).

6.2 EAD metrics correctly classify some drugs that APD90 gets wrong

While APD prolongation is often linked with Torsades, some drugs which prolong APD are not torsadogenic (Sager, 2008). Ranolazine is an example of a drug which is not linked to Torsades but does prolong action potential duration (Kramer et al., 2013; Milberg and Haverkamp, 2005; Cobbe, 2004; Stockbridge et al., 2013), while suppressing the formation of EADs (Antzelevitch et al., 2004). The APD90 metric mis-classifies ranolazine from the intermediate risk category 4 to the most dangerous category 2. However, the hERG block EAD metric is able to correctly classify ranolazine.

The hERG EAD metric-based classification of ranolazine into the correct category is consistent across all modifiers. The ICaL EAD metric mis-classified ranolazine at a cycle length of 3000 ms, but correctly classified it at shorter cycle lengths, and also when the drug concentration or extracellular potassium concentration were reduced. Ranolazine is known to strongly block the persistent sodium current, which is active during the plateau phase and linked to arrhythmogenesis (Song et al., 2006; Shimizu and Antzelevitch, 1997).

The APD90 metric also mis-classified the category 5 drug verapamil into category 4. Both the hERG EAD metric and the injury current EAD metric assigned the correct class to verapamil. Verapamil prolongs APD but does not induce EADs (Liang et al., 2013), and can prevent TdP (Farkas et al., 2009). Verapamil strongly blocks the L-type calcium current. Cibenzoline, a fast sodium blocker and nitrendipine, an L-type calcium current blocker, were both correctly classified by the hERG EAD metric and not the APD90 metric.

Verapamil and flecainide were correctly classified by the qNet and cqInward metrics. Ranolazine, cibenzoline, and nitrendipine were mis-classified into a more dangerous group by qNet and cqInward.

While EADs are generally accompanied by an increase in APD90, neither purely EAD-based metrics nor the qNet and cqInward metrics were linearly related to APD. Instead, both types of metric offered some improvement over APD90 for drugs which prolong the action potential, but do not cause Torsades.

6.3 EAD-based arrhythmic risk metrics are more accurate than other metrics

We used machine learning methods to separate drugs into risk categories based on the EAD threshold values for each of the interventions, and then assessed the accuracy using leave-one-out cross-validation. For comparison, we calculated the Mirams et al. (2011) APD90 metric, the Lancaster and Sobie (2016) two-dimensional metric, the Li et al. (2017) cqInward metric, the Dutta et al. (2017) qNet metric, and the Redfern et al. (2003) hERG/Cmax safety margin, and compared the classification accuracy. With the exception of APD90, the EAD-based risk metrics outperformed all of the other metrics calculated for this dataset. Used as a one-dimensional predictor, the L-type calcium increase EAD metric was slightly more accurate than the hERG increase EAD metric or the injury current EAD metric.

APD90 is a well-established predictor of proarrhythmic risk (Mirams et al., 2011), as it is linked to the rabbit heart wedge (Beattie et al., 2013) and Thorough QT (Mirams et al., 2014) experiments. The Lancaster and Sobie (2016) two-dimensional classifier uses both APD50 and the diastolic calcium concentration for classification. We calculated this metric for both the Grandi et al. (2010) and the O'Hara et al. (2011) models, and the Grandi model performed better. The addition of the calcium concentration made the classification accuracy worse - when APD50 was considered alone, the accuracy was precisely the same as for the APD90 metric.

This may be due to the way that the amplitude of the calcium transient in the O'Hara et al. (2011) model increases in response to sodium current block, as discussed in Tomek et al. (2019).

Most EAD-based torsadogenic risk metrics rely on an increase in the drug concentration far beyond the usual physiological levels. Increased drug concentration is known to be a risk factor for drug-induced Torsades, most notably in the case of terfenadine, which is most torsadogenic in patients with impaired metabolic function (Woosley et al., 1993; Bryan, 2011; Yap and Camm, 2003). Increasing drug concentration also has the benefit of maximising the effects of the drug. Combining pro-arrhythmic underlying conditions with increased drug concentrations has been used by Christophe and Crumb (2019) and Christophe (2022) to improve the performance of EAD-based classifiers. However, drugs can also have torsadogenic effects at normal concentrations. Our work offers a novel EAD-based classifier that uses only pro-arrhythmic interventions to induce EADs, without an increase in drug concentration. Instead, the drug effects are only maximised by pacing the model to steady state with drug block. The Li et al. (2017) cqInward metric and Dutta et al. (2017) qNet metrics are both based on the sum of currents during the action potential - cqInward considers only late sodium and L-type calcium current, whereas qNet also includes several key potassium currents. While these metrics do not specifically rely on the detection of EADs or calculation of APD90, they are related to both, as the sum of these currents during the action potential will be larger when action potential is prolonged, and when an EAD is formed. Indeed, in Dutta et al. (2017), the qNet metric was found to correlate with the hERG block EAD threshold. When calculated using our drug dataset, this correlation was much less pronounced, especially for drugs of high torsadogenic risk. This indicates that the EAD threshold metrics are not redundant when compared with qNet, and can offer further information alongside the qNet metric to further separate risk categories. This is shown by the fact that combining the ICaL increase EAD metric with the qNet or cqInward metrics increased the accuracy of classification.

The good performance of our EAD-based metrics compared to the present state-of-the-art shows that a torsadogenic predictor based on EAD-provoking interventions at physiological drug concentrations has value as a tool for the prediction of drug-induced arrhythmia.

6.3.1 Variability in measurements of IC50 values affects classification results

As part of this work, we gathered a dataset of IC50 values for drugs of known torsadogenic risk, favouring manual patch-clamp over automated, and values from human cells at body temperature. Variability in measurements of drug kinetic parameters such as IC50 values is a known problem in the prediction of drug-induced Torsades de Pointes arrhythmia (Li et al., 2020b; Mirams et al., 2016; Johnstone et al., 2016), and the differences in results for pre-existing proarrhythmic methods using different input datasets are an illustration of this.

For example, for the qNet metric created by Dutta et al. (2017), using our drug dataset for the twelve validation compounds led to much worse performance than that reported in the original paper, even using the same model and method of simulating hERG block. In particular, bepridil, which is classified as the 4th most torsadogenic compound out of the twelve validation compounds in the Dutta et al. (2017) paper, was eleventh when qNet was calculated using this dataset. The difference in bepridil's hERG IC50 values between the two datasets is stark: we have used the value from Redfern et al. (2003), which is 600 nM, and the experimental measurements obtained for Dutta et al. (2017) give an IC50 of 50 nM - a 12x more potent block of the ion current. Compounding this difference, our dataset also has a value for bepridil's L-type calcium block that is 13x more potent than theirs. A comparison between the IC50 values is shown in Table 6.1. With the exception of the hERG current, Dutta et al. (2017) used the Crumb et al. (2016) dataset for the IC50 values used for simulations. Johnstone et al. (2016) investigated the uncertainty found in the calculation of IC50 values in that dataset and found that the distribution of pIC50 values that can be calculated from the experimental data can cover a range of 1 uM, which in terms of IC50s means a ten-fold difference between the highest and lowest possible values. For most of the IC50 values, ours were similar to the other dataset, with most only varying by a factor of 1-2. Values with a factor greater than 10 are shaded in red (if our dataset had a stronger block) and green (if our dataset had a weaker block).

The difference in ranking between the twelve validation compounds using the Crumb et al. (2016) dataset and our dataset is shown in Figure 6.1. The qNet metric was more robust to changes in dataset than the cqInward metric. Like bepridil, quinidine also had large differences

Drug	hERG	INaL	ICaL	INa	Ito	IK1	IKs
bepridil	12.000	1.000	0.075	1.263	0.768		0.349
chlorpromazine	1.593	1.000	0.366	0.617	0.001	0.658	
cisapride	0.644		0.002		0.043		0.000
diltiazem	0.562		0.482	0.128	0.000		
dl-sotalol	2.514						
dofetilide	1.020		102.574	788.436			
mexiletine	1.731	1.965	2.615				
ondansetron	0.614	1.000	1.000	1.535			
quinidine	0.302		0.302	1.346	250.903	0.005	1.000
ranolazine	1.391	0.824		4.275			0.053
terfenadine	0.387		0.535	0.202			0.005
verapamil	0.497		0.496		196.036		

Table 6.1: Difference (factor) between IC50 values used in this work and the ones from Dutta et al. (2017). Higher values mean that our dataset had a larger IC50 value and therefore a weaker block of that current. Values greater than 10 are shaded in green, and values less than 0.1 are shaded in red.

in IC50 data between datasets - however, the ranking for the qNet metric was the same. Our dataset had IC50 values for quinidine that were 3x lower for both hERG and ICaL, and the opposing effects of these two differences prevented perturbations to the qNet score. The largest differences in quinidine IC50s were for Ito and IK1 - we had a much stronger block for IK1 and a much weaker block for Ito than the other dataset. As these are both repolarising currents, the difference in values again had opposing effects. DL-sotalol is a strong blocker of hERG and a very weak blocker of the other currents. Our IC50 value for hERG block was 2.5x higher, and unlike quinidine, dl-sotalol is an outlier for both metrics, as there are no opposing currents involved to ameliorate the effects. Ondansetron and mexiletine had relatively small differences in IC50 values between datasets, and their ranking is relatively similar between datasets for the qNet metric. However, these small differences caused a large change in the cqInward metric for ondansetron.

There were large differences between the results using different drug datasets, even for IC50 values that were comfortably within a factor of 10, i.e. within a realistic range that could be obtained even in the same lab, using the same experimental protocols (Johnstone et al., 2016). These differences imply that uncertainty in drug kinetic measurements is a key feature that must be incorporated into risk categorisation metrics in order to ensure that they are robust to perturbations in input parameters. This is in line with the CiPA principles for uncertainty

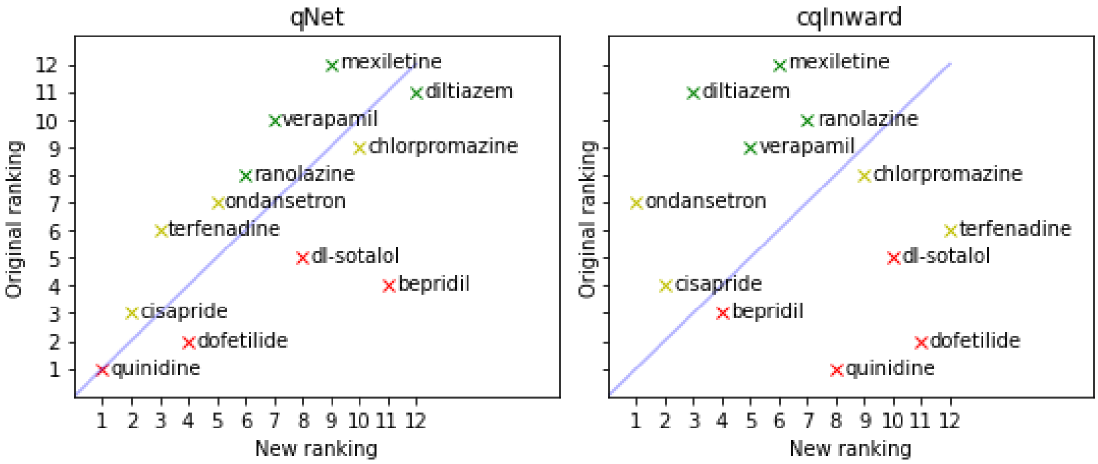

Figure 6.1: Difference in ranking of the twelve CiPA validation compounds for qNet (left) and cqInward (right) when using our dataset (X axis) or the original dataset (Y axis).

quantification (Mirams et al., 2016; Li et al., 2020b). The improved performance of qNet over cqInward shows that the consideration of both repolarising and depolarising currents during the action potential can add robustness against these perturbations.

6.3.2 The hERG block EAD threshold metric is a perfect classifier when considering only binary extremes of risk

Assessing drug datasets in terms of a binary classification is a common form of analysis for torsadogenic risk prediction (Mirams et al., 2014; Beattie et al., 2013; Lancaster and Sobie, 2016; Passini et al., 2017; Christophe, 2022; Li et al., 2019; Christophe and Crumb, 2019). Here, we have produced receiver operator characteristic curves for the metrics of interest, and calculated the area under the curve as a measure of metric performance. This allows for assessment of classifiers without the need to use machine learning techniques to find the boundaries between groups - instead, each possible boundary is considered to get an overall measure of the sensitivity-specificity trade-off for each metric. When considering only the most dangerous (group 2) and least dangerous (group 5) drugs, APD90 and the hERG block EAD metric were both perfect classifiers. While there is some variation in the way that intermediate-risk drugs are classified (often, the two intermediate groups used for this study are combined into one), the most and least dangerous are consistent between the Redfern et al. (2003) and CiPA categories. The

ICaL-induced EAD metric outperformed the Redfern et al. (2003) hERG safety margin when considering the extreme groups, meaning that the addition of multi-ion current block is an improvement over simple hERG block alone for this problem. However, the ICaL EAD metric performed worse when binary classification was performed for the full dataset, meaning that it was less successful at differentiating between the intermediate classes.

Compared to the EAD and APD90 metrics, qNet and cqInward performed worse for both types of binary classifier. Using this dataset, cqInward over-estimated the risk of the least torsadogenic drugs, and under-estimated the most torsadogenic drugs, whereas the qNet metric instead under-estimated the risk for outliers in the most torsadogenic category. In Li et al. (2019), the areas under the ROC curve calculated for the qNet metric for their drug dataset were higher, ranging from 0.901 (when high and intermediate risk categories were combined) to 0.988 (when low and intermediate risk categories were combined). As discussed above, these metrics performed worse when our drug dataset was used, even considering the differences in dynamic hERG modelling, so this difference is consistent with that.

EAD metrics performed better than qNet and cqInward when evaluated using a four-class risk categorisation system, a binary system using all of the drugs, and a binary system considering only the most and least dangerous drugs. This shows that the metrics are robust over different risk categorisation systems and underlines their value as proarrhythmic risk metrics.

6.4 Linear discriminant analysis outperforms support vector machines for categorising 1D EAD-based metrics

Linear discriminant analysis and support vector machines are both methods which can be used for choosing boundaries in classification problems. The boundaries chosen using these methods differed greatly, and for 1D EAD-based methods, LDA outperformed SVM in terms of accuracy when assessed using leave-one-out cross-validation. The two main problems with the metrics under consideration in this work are the relatively small number of data points - a total of 41 drugs split into four groups - and the degree of overlap between the categories, which was large for every metric calculated using this dataset. For EAD-based metrics, the outliers in the intermediate risk categories were further apart than for APD, and overlapped more severely with other groups. This means that relying on the overlapping values alone for boundary calculations, as in SVM, makes the intermediate categories extremely small. However, when all of the values in each group are considered, such as in LDA, the contribution of the non-overlapping values, combined with the extra information provided by the assumption of a normal distribution, compensates for the increased overlap and creates more accurate classification.

Support vector machines offer an improvement over linear discriminant analysis when used to separate risk categories of the APD90 metric. This is an improvement over the original Mirams et al. (2011) method, which used LDA. Lancaster and Sobie (2016) used SVM for finding category boundaries, and in this work we have also found SVM to be the best machine learning technique to use with this metric. LDA performed better than SVM for the qNet and cqInward metrics, which is in line with the results from Li et al. (2019), where logistic regression (a similar method to LDA, which uses all the data points in each group, without the assumption of normality) was used to assign boundaries to overlapping classes.

With torsadogenic risk metrics, there is likely to be a degree of overlap between classes, especially when the metric is based on something which shows dynamical chaos, like the formation of EADs, or when a distribution of inputs is used to represent variability. When the overlap spans fewer classes, such as with APD90 and the 2D metrics reported in this thesis, a simple classifier based on the points closest to the boundaries, such as SVM, is sufficient. However, when there is a large spread within each risk group, a method such as LDA, which considers all the data points in the groups, is preferable.

The ultimate aim of a risk metric would be to create total separation between risk categories, making LDA redundant as a method for choosing boundary values. However, considering the variability found in drug parameters, underlying physiology, and the way that risk categories are assigned based on real-world data, a certain amount of overlap is probable. Therefore, making the most use of every value in the dataset by using LDA rather than just considering the boundaries, like in SVM, prediction accuracy for overlapping metrics can be improved.

6.5 Combining APD and EAD metrics increases classification accuracy

When a 2D classifier is used, further separation between risk categories can be achieved, particularly when EAD-based metrics are combined with APD90.

When APD90 is combined with EAD metrics, the extra separation along the APD axis overcomes the limitations of increased overlap between groups on the EAD axes, and support vector machines become a better method of classification for these 2D metrics than linear discriminant analysis.

However, while the combination of EAD metrics and APD90 increases the overall classification accuracy of the EAD metrics, it does not offer further information over APD90 alone. The combination of the injury current EAD intervention and the hERG block EAD intervention does offer some new information: the drugs amiodarone, methadone, and tedisamil are all correctly classified using this method, while being mis-classified by APD90, and by both EAD metrics when used separately.

A previous 2D classifier reported in the literature is the Lancaster and Sobie (2016) metric, which combines APD50 with diastolic calcium concentration.

6.6 Future work

Future work to build on these findings could include an investigation into the effects of variability in human cells on the induced thresholds, in the manner of Passini et al. (2017). Systems which show dynamical chaos, like the genesis of EADs, show sharp discontinuities in results, and the addition of a wider level of baseline variability in the cell models under consideration would show the locations of these discontinuities in parameter space, as well as simulating the biologically-relevant variability found *in vivo*.

As in Mirams et al. (2014), Christophe (2013), and Passini et al. (2017), for the EAD metrics in this work, we have only used the O'Hara et al. (2011) model. Using the updated Dutta et al. (2017) model could provide further information about torsadogenic effects, particularly when considering the effect of rate dependence and the importance of the INaL current. Persistent sodium plays a larger role in repolarisation in the Dutta et al. (2017) model than in the O'Hara et al. (2011) model, which means that the anti-arrhythmic effect of INaL block will be more pronounced in this model, meaning that drugs such as mexiletine, ranolazine, and flecainide that strongly block INaL will have higher EAD thresholds. Flecainide, in particular, is frequently mis-classified as being more dangerous than it is in these simulations, so this would likely be an improvement. The Tomek et al. (2019) model shows improvement over the O'Hara et al. (2011) model in several relevant ways. In the ORd model, the L-type calcium current flows in the wrong direction briefly after the peak of the action potential. When the conductance of this current is increased, as it is in our simulations, this reverse flow is even larger. The reformulation of ICaL in the ToR-ORd model prevents this, and so would improve the simulation of ICaL increase as an EAD inducing intervention. ToR-ORd has a lower plateau potential than ORd, which would be protective against EADs caused by ICaL reactivation, thus raising ICaL thresholds. Block of INa in the ToR-ORd model leads to a reduction in ICaL, which means that drugs which block INa have a stronger anti-arrhythmic effect. However, using an optimised model does not always improve the accuracy of proarrhythmic risk prediction, as found in Tomek et al. (2019), where the Passini et al. (2017) metric was calculated using the new model and found to be less accurate than when simulations used the original O'Hara et al. (2011) model.

Our EAD-provoking interventions reduce repolarisation reserve in several different ways - by increasing the depolarising L-type calcium current, by decreasing the repolarising hERG current, and by adding a brief, depolarising stimulus current. There are a number of other options for creating similar effects - the conductance of other depolarising currents such as the late sodium current can be increased, other repolarising currents such as IKs and IK1 can be decreased, the activation and inactivation kinetics of currents can be modified to increase the open probabilities during the vulnerable window region around the plateau voltage, and the intracellular calcium dynamics can be modified. While we were unable to induce EADs by increasing gNaL, increasing intracellular calcium concentration or decreasing gKs in the original O'Hara et al. (2011) model, the improved modelling of persistent sodium in the Dutta et al. (2017) model and the modifications to intracellular calcium dynamics in the Tomek et al. (2019) model would open up these possibilities.

Another interesting future direction for this work could be to use the distributions of possible

IC50 values and Hill coefficients calculated in Johnstone et al. (2016) to produce distributions of EAD risk metrics. One way to create an improved, more stable torsadogenic risk metric would be to choose metrics for which categorisations are correct throughout the probability distributions of the input parameters. In Li et al. (2019), the qNet metric is compared to APD90 and the Lancaster and Sobie (2016) metric using this approach. We have reported a preliminary investigation into extending this work to the EAD threshold metrics in McMillan et al. (2017b).

Chapter 7

Conclusion

In this thesis, we have used computer modelling and simulation of human heart cells for the prediction of drug-induced cardiac adverse events. We gathered data for a set of 41 drugs, including IC50s, EFTPCs, and torsadogenic risk categories, using manual patch clamp ion current measurements where possible, from drugs of known levels of torsadogenic risk. Ion current block was then implemented in a human ventricular cell model to mimic the effects of these drugs at realistic physiological concentrations. Three interventions were implemented to induce EADs in the model: an increase in L-type calcium current conductance, a decrease in the hERG rapid delayed rectifier potassium current conductance, and an injury current applied during the action potential. Algorithms for detecting EADs and finding thresholds were created and used to calculate the minimum intervention necessary to produce an EAD for each of the drugs and interventions. The dataset was also used to calculate other metrics from the literature for benchmarking and comparison: the Mirams et al. (2011) APD90 metric, the Lancaster and Sobie (2016) 2D classifier metric, the Dutta et al. (2017) qNet metric, and the Li et al. (2017) cqInward metric. The machine learning techniques of linear discriminant analysis and support vector machines were used for categorisation of drugs into risk categories based on the threshold and metric values obtained from the simulations. Metrics were also combined, and pro- and anti-arrhythmic modifications were investigated in order to increase the separation between risk classes. Leave-one-out cross-validation and receiver operator characteristics were used to assess the suitability of these metrics for proarrhythmic risk prediction.

Using this dataset of IC50 and EFTPC values, EAD-based metrics outperformed all other metrics under consideration except for APD90, using both four-class and binary risk categories. This includes the Redfern et al. (2003) hERG block safety margin. The EAD metrics were able to accurately predict the risk of some drugs which APD90 gets wrong, showing that they have promise as an improvement over APD90 in some cases, including for verapamil and ranolazine, which both prolong the action potential and block hERG but are not associated with Torsades.

The prediction of torsadogenic risk based on *in silico* metrics which take into account screening data from early in the drug development pipeline can allow non-torsadogenic drugs which prolong the QT interval to be accurately assessed for their risk, increasing the specificity of prediction and preventing safe drugs, like verapamil and ranolazine, from being discarded unnecessarily.

Bibliography

C. C. Aggarwal. *Data Classification.* 2015. ISBN 978-1-4665-8674-1.

T. Aiba, G. G. Hesketh, A. S. Barth, T. Liu, S. Daya, K. Chakir, V. L. Dimaano, T. P. Abraham, B. O'Rourke, F. G. Akar, D. A. Kass, and G. F. Tomaselli. Electrophysiological consequences of dyssynchronous heart failure and its restoration by resynchronization therapy. *Circulation*, 119(9):1220–1230, 2009.

C. Antzelevitch, L. Belardinelli, A. C. Zygmunt, A. Burashnikov, J. M. Di Diego, J. M. Fish, J. M. Cordeiro, and G. Thomas. Electrophysiological effects of ranolazine, a novel antianginal agent with antiarrhythmic properties. *Circulation*, 110(8):904–10, 2004.

J. L. Bauman, R. A. Bauernfeind, J. V. Hoff, B. Strasberg, S. Swiryn, and K. M. Rosen. Torsade de pointes due to quinidine: observations in 31 patients. *American Heart Journal*, 107(3): 425–430, 1984.

K. A. Beattie, C. Luscombe, G. Williams, J. Munoz-Muriedas, D. J. Gavaghan, Y. Cui, and G. R. Mirams. Evaluation of an in silico cardiac safety assay: Using ion channel screening data to predict QT interval changes in the rabbit ventricular wedge. *Journal of Pharmacological and Toxicological Methods*, 68(1):88–96, 2013.

B. Y. G. W. Beeler and H. Reuter. Reconstruction of the action potential of ventricular myocardial fibres. *The Journal of Physiology*, 268:177–210, 1977.

P. B. Bennett, K. Yazawa, N. Makita, and A. L. George. Molecular mechanism for an inherited cardiac arrhythmia. *Nature*, 376(6542):683–5, 1995.

D. M. Bers. 16 - excitation-contraction coupling. In D. P. Zipes and J. Jalife, editors, *Cardiac Electrophysiology: From Cell to Bedside (Sixth Edition)*, pages 161 – 169. W.B. Saunders, Philadelphia, sixth edition edition, 2014. ISBN 978-1-4557-2856-5.

D. Bottino, R. C. Penland, A. Stamps, M. Traebert, B. Dumotier, A. Georgieva, G. Helmlinger, and G. S. Lett. Preclinical cardiac safety assessment of pharmaceutical compounds using an integrated systems-based computer model of the heart. *Progress in Biophysics Molecular Biology*, 90(3):414–443, 2006.

M. Brini and E. Carafoli. 5 - mammalian calcium pumps in health and disease. In D. P. Zipes and J. Jalife, editors, *Cardiac Electrophysiology: From Cell to Bedside (Sixth Edition)*, pages 43 – 53. W.B. Saunders, Philadelphia, sixth edition edition, 2014. ISBN 978-1-4557-2856-5.

J. Bryan. Despite its problems, terfenadine did set a new standard for hay fever treatment. *Pharmaceutical Journal*, 287:511–512, 2011.

J. Carro, J. F. Rodríguez, P. Laguna, and E. Pueyo. A human ventricular cell model for investigation of cardiac arrhythmias under hyperkalaemic conditions. *Philosophical Transactions. Series A, Mathematical, Physical, and Engineering Sciences*, 369(1954):4205–4232, 2011.

W. A. Catterall. 1 - voltage-gated sodium channels and electrical excitability of the heart. In D. P. Zipes and J. Jalife, editors, *Cardiac Electrophysiology: From Cell to Bedside (Sixth Edition)*, pages 1 – 11. W.B. Saunders, Philadelphia, sixth edition edition, 2014. ISBN 978-1-4557-2856-5.

W. A. Catterall, I. M. Raman, H. P. C. Robinson, T. J. Sejnowski, and O. Paulsen. The Hodgkin-Huxley heritage: from channels to circuits. *The Journal of Neuroscience*, 32(41):14064–14073, 2012.

I. Cavero and H. Holzgrefe. CiPA: Ongoing testing, future qualification procedures, and pending issues. *Journal of Pharmacological and Toxicological Methods*, 76:27–37, 2015.

M. G. Chang, D. Sato, E. d. Lange, J.-H. Lee, H. S. Karagueuzian, A. Garfinkel, J. N. Weiss, and Z. Qu. Bi-stable wave propagation and early afterdepolarization–mediated cardiac arrhythmias. *Heart Rhythm*, 9(1):115–122, 2012. Publisher: Elsevier.

P.-C. Chang, Y.-C. Hsieh, C.-H. Hsueh, J. N. Weiss, S.-F. Lin, and P.-S. Chen. Apamin induces early afterdepolarizations and torsades de pointes ventricular arrhythmia from failing rabbit ventricles exhibiting secondary rises in intracellular calcium. *Heart Rhythm*, 10(10):1516–1524, 2013. WOS:000325150300019.

B.-R. Choi, F. Burton, and G. Salama. Cytosolic Ca2+ triggers early afterdepolarizations and Torsade de Pointes in rabbit hearts with Type 2 Long QT syndrome. *The Journal of Physiology*, 543(Pt 2):615–631, 2002.

B. Christophe. Simulation of early after-depolarisation in non-failing human ventricular myocytes: Can this help cardiac safety pharmacology? *Pharmacology Reports*, 65(5):1281–1293, 2013.

B. Christophe. Occurrence of early afterdepolarization under healthy or hypertrophic cardiomyopathy conditions in the human ventricular endocardial myocyte: In silico study using 109 torsadogenic or non-torsadogenic compounds. *Toxicology and Applied Pharmacology*, 438: 115914, 2022.

B. Christophe and W. J. Crumb. Impact of disease state on arrhythmic event detection by action potential modelling in cardiac safety pharmacology. *Journal of Pharmacological and Toxicological Methods*, 96:15–26, 2019.

C. E. Clancy and Y. Rudy. Na+ channel mutation that causes both Brugada and long-QT syndrome phenotypes: a simulation study of mechanism. *Circulation*, 105(10):1208–1213, 2002.

S. Cobbe. Electrophysiological perspectives: What has ranolazine taught us? *European Heart Journal Supplements*, 6:I9–I11, 2004.

S. D. Cohen and A. C. Hindmarsh. CVODE, a stiff/nonstiff ODE solver in C. *Computers in Physics*, 10(2):138–143, 1996.

Committee on Safety of Medicines and Medicines Control Agency. Cisapride (Prepulsid) withdrawn. *Current Problems in Pharmacovigilance*, 26:9–14, 2000.

J. Cooper, S. McKeever, and A. Garny. On the application of partial evaluation to the optimisation of cardiac electrophysiological simulations. In *Proceedings of the 2006 ACM SIGPLAN Symposium on Partial Evaluation and Semantics-based Program Manipulation*, PEPM '06, pages 12–20, New York, NY, USA, 2006. ACM. ISBN 1-59593-196-1.

J. Cooper, R. J. Spiteri, and G. R. Mirams. Cellular cardiac electrophysiology modeling with Chaste and CellML. *Frontiers in Physiology*, 6:511, 2015.

P. F. Cranefield. Action potentials, afterpotentials, and arrhythmias. *Circulation Research*, 41 (4):415–423, 1977.

N. Cristianini and J. Shawe-Taylor. *An Introduction to Support Vector Machines: And Other Kernel-based Learning Methods.* Cambridge University Press, New York, NY, USA, 2000. ISBN 0-521-78019-5.

W. J. Crumb, J. Vicente, L. Johannesen, and D. G. Strauss. An evaluation of 30 clinical drugs against the comprehensive in vitro proarrhythmia assay (CiPA) proposed ion channel panel. *Journal of Pharmacological and Toxicological Methods*, 81:251–262, 2016.

A. A. Cuellar, C. M. Lloyd, P. F. Nielsen, D. P. Bullivant, D. P. Nickerson, and P. J. Hunter. An overview of cellml 1.1, a biological model description language. *Simulation*, 79(12):740–747, 2003.

M. E. Curran, I. Splawski, K. W. Timothy, G. M. Vincent, E. D. Green, and M. T. Keating. A molecular basis for cardiac arrhythmia: HERG mutations cause long QT syndrome. *Cell*, 80 (5):795–803, 1995.

F. Dessertenne. [Ventricular tachycardia with 2 variable opposing foci]. *Archives des maladies du coeur et des vaisseaux*, 59(2):263–72, 1966.

E. de Lange, Y. Xie, and Z. Qu. Synchronization of Early Afterdepolarizations and Arrhythmogenesis in Heterogeneous Cardiac Tissue Models. *Biophysical Journal*, 103(2):365–373, 2012. Publisher: Elsevier.

D. DiFrancesco and D. Noble. A model of cardiac electrical activity incorporating ionic pumps and concentration changes. *Philosophical Transactions of the Royal Society of London. Series B, Biological Sciences*, 307(1133):353–398, 1985.

S. Dutta, A. Mincholé, E. Zacur, T. A. Quinn, P. Taggart, and B. Rodriguez. Early afterdepolarizations promote transmural reentry in ischemic human ventricles with reduced repolarization reserve. *Progress in Biophysics and Molecular Biology*, 120(1-3):236–248, 2016.

S. Dutta, K. C. Chang, K. A. Beattie, J. Sheng, P. N. Tran, W. W. Wu, M. Wu, D. G. Strauss, T. Colatsky, and Z. Li. Optimization of an In silico Cardiac Cell Model for Proarrhythmia Risk Assessment. *Frontiers in Physiology*, 8, 2017.

N. El-Sherif, R. H. Zeiler, W. Craelius, W. B. Gough, and R. Henkin. QTU prolongation and polymorphic ventricular tachyarrhythmias due to bradycardia-dependent early afterdepolarizations. Afterdepolarizations and ventricular arrhythmias. *Circulation Research*, 63:286–305, 1988.

R. C. Elkins, M. R. Davies, S. J. Brough, D. J. Gavaghan, Y. Cui, N. Abi-Gerges, and G. R. Mirams. Variability in high-throughput ion-channel screening data and consequences for cardiac safety assessment. *The Journal of Pharmacological and Toxicological Methods*, 68(1):112–122, 2013.

European Medicines Agency. Note for Guidance on the Nonclinical Evaluation of the Potential for Delayed Ventricular Repolarization (QT Interval Prolongation) by Human Pharmaceuticals. *ICH Topic S7B*, 2005.

A. Fabiato and P. Coumel. Torsades de Pointes, a quarter of a century later: a tribute to Dr. F. Dessertenne. *Cardiovascular Drugs and Therapy*, 5:167–169, 1991.

A. S. Farkas, P. Makra, N. Csík, S. Orosz, M. J. Shattock, F. Fülöp, T. Forster, M. Csanády, J. G. Papp, A. Varró, and A. Farkas. The role of the Na+/Ca2+ exchanger, INa and ICaL in the genesis of dofetilide-induced torsades de pointes in isolated, AV-blocked rabbit hearts. *British Journal of Pharmacology*, 156(6):920–932, 2009.

P. Fomby and A. J. Cherlin. Chronic heart failure slows late sodium current in human and canine ventricular myocytes: implications for repolarization variability. *Nature*, 72(2):181–204, 2011.

G. Frommeyer and L. Eckardt. Drug-induced proarrhythmia: risk factors and electrophysiological mechanisms. *Nature Reviews Cardiology*, 13:36–47, 2015.

A. Garny and P. J. Hunter. OpenCOR: a modular and interoperable approach to computational biology. *Frontiers in Physiology*, 6, 2015.

E. Grandi, F. S. Pasqualini, and D. M. Bers. A novel computational model of the human ventricular action potential and Ca transient. *Molecular Cell*, 48(1):112–120, 2010.

D. Guo, Q. Liu, T. Liu, G. Elliott, M. Gingras, P. R. Kowey, and G.-X. Yan. Electrophysiological Properties of HBI-3000: A New Antiarrhythmic Agent With Multiple-channel Blocking Properties in Human Ventricular Myocytes. *Journal of Cardiovascular Pharmacology*, 57(1): 79–85, 2011.

M. A. Habbab and N. El-Sherif. Drug-induced torsades de pointes: role of early afterdepolarizations and dispersion of repolarization. *American Journal of Medicine*, 89(2):241–6, 1990.

J. Hall. *Guyton and Hall Textbook of Medical Physiology E-Book*. Guyton Physiology. Elsevier Health Sciences, 2010. ISBN 9781437726749.

T. Hastie. *The elements of statistical learning: data mining, inference, and prediction [electronic resource]*. Springer series in statistics. Springer, New York, second edition, corrected 7th printing. edition, 2009. ISBN 978-0-387-84858-7.

J.-Q. He, Y. Ma, Y. Lee, J. A. Thomson, and T. J. Kamp. Human embryonic stem cells develop into multiple types of cardiac myocytes: action potential characterization. *Circulation Research*, 93(1):32–39, 2003.

M. Hiraoka, K. Ikeda, and T. Sano. The mechanism of barium-induced automaticity in ventricular muscle fibers. *Advances in Myocardiology*, 1:255–266, 1980.

M. Hiraoka, A. Sunami, Z. Fan, and T. Sawanobori. Multiple ionic mechanisms of early afterdepolarizations in isolated ventricular myocytes from guinea-pig hearts. *Annals of the New York Academy of Sciences*, 644:33–47, 1992.

A. Hodgkin and A. Huxley. A quantitative description of membrane current and its application to conduction and excitation in nerve. *The Journal of Physiology*, 117:500–544, 1952.

R. B. Huffaker, J. N. Weiss, and B. Kogan. Effects of early afterdepolarizations on reentry in cardiac tissue: a simulation study. *American Journal of Physiology-Heart and Circulatory Physiology*, 292(6):H3089–H3102, 2007. Publisher: American Physiological Society.

G. James. *An introduction to statistical learning: with applications in R [electronic resource]*. Springer texts in statistics. Springer, New York, second edition. edition, 2021. ISBN 978-1-07-161418-1.

M. J. Janse and A. L. Wit. Electrophysiological mechanisms of ventricular arrhythmias resulting from myocardial ischemia and infarction. *Physiological reviews*, 69(4):1049–169, 1989.

M. J. Janse, R. Coronel, and T. Opthof. Counterpoint: M cells do not have a functional role in the ventricular myocardium of the intact heart. *Heart Rhythm*, 8(6):934–937, 2011.

C. T. January and J. M. Riddle. Early afterdepolarizations: mechanism of induction and block. A role for L-type Ca2+ current. *Circulation Research*, 64(5):977–990, 1989.

R. H. Johnstone, R. Bardenet, D. J. Gavaghan, and G. R. Mirams. Hierarchical Bayesian inference for ion channel screening dose-response data. *Wellcome Open Research*, 1:6, 2016.

P. Kang, M. Liao, M. R. Wester, J. S. Leeder, and R. E. Pearce. Exome sequencing and systems biology converge to identify novel mutations in the L-type calcium channel, CACNA1C, linked to autosomal dominant Long QT Syndrome. *Circulation: Cardiovascular Genetics*, 36(3):490–499, 2010.

A. M. Katz. Effects of digitalis on cell biochemistry: sodium pump inhibition. *Journal of the American College of Cardiology*, 5:16A–21A, 1985.

S. P. Kelly. Aconite poisoning. *Medical Journal of Australia*, 153(8):499, 1990.

J. Kramer, C. A. Obejero-Paz, G. Myatt, Y. A. Kuryshev, A. Bruening-Wright, J. S. Verducci, and A. M. Brown. MICE Models: Superior to the HERG Model in Predicting Torsade de Pointes. *Scientific Reports*, 3:299–307, 2013.

Y. Kurata, I. Hisatome, H. Matsuda, and T. Shibamoto. Dynamical Mechanisms of Pacemaker Generation in IK1-Downregulated Human Ventricular Myocytes: Insights from Bifurcation Analyses of a Mathematical Model. *Biophysical Journal*, 89(4):2865–2887, 2005.

Y. Kurata, K. Tsumoto, K. Hayashi, I. Hisatome, M. Tanida, Y. Kuda, and T. Shibamoto. Dynamical mechanisms of phase-2 early afterdepolarizations in human ventricular myocytes: insights from bifurcation analyses of two mathematical models. *American Journal of Physiology-Heart and Circulatory Physiology*, 312(1):H106–H127, 2017. WOS:000395794800010.

Y. Kurata, K. Tsumoto, K. Hayashi, I. Hisatome, Y. Kuda, and M. Tanida. Multiple Dynamical Mechanisms of Phase-2 Early Afterdepolarizations in a Human Ventricular Myocyte Model: Involvement of Spontaneous SR Ca2+ Release. *Frontiers in Physiology*, 10:1545, 2020. WOS:000508449900001.

E. G. Lakatta, Y. Yaniv, and V. A. Maltsev. 25 - cardiac impulse is initiated by a coupled system of membrane ion channels and ca2+ cycling proteins. In D. P. Zipes and J. Jalife, editors, *Cardiac Electrophysiology: From Cell to Bedside (Sixth Edition)*, pages 243 – 252. W.B. Saunders, Philadelphia, sixth edition edition, 2014. ISBN 978-1-4557-2856-5.

M. C. Lancaster and E. A. Sobie. Improved prediction of drug-induced Torsades de Pointes through simulations of dynamics and machine learning algorithms. *Clinical Pharmacology and Therapy*, 100(4):371–379, 2016.

C. L. Lawrence, M. H. Bridgland-Taylor, C. E. Pollard, T. G. Hammond, and J. P. Valentin. A rabbit Langendorff heart proarrhythmia model: predictive value for clinical identification of Torsades de Pointes. *British Journal of Pharmacology*, 149(7):845–860, 2006.

G.-L. Li, A. M. Saguner, G. H. Fontaine, and R. Frank. Fragmented endocardial signals and early afterdepolarizations during torsades de pointes tachycardia. *Cardiology Journal*, 27(1): 54–61, 2020a. Number: 1.

Z. Li, S. Dutta, J. Sheng, P. N. Tran, W. Wu, K. Chang, T. Mdluli, D. G. Strauss, and T. Colatsky. Improving the in silico assessment of proarrhythmia risk by combining hERG (Human Ether-à-go-go-Related Gene) channel–drug binding kinetics and multichannel pharmacology. *Circulation: Arrhythmia Electrophysiology*, 10(2):e004628, 2017.

Z. Li, B. J. Ridder, X. Han, W. W. Wu, J. Sheng, P. N. Tran, M. Wu, A. Randolph, R. H. Johnstone, G. R. Mirams, Y. Kuryshev, J. Kramer, C. Wu, W. J. Crumb, and D. G. Strauss. Assessment of an In Silico Mechanistic Model for Proarrhythmia Risk Prediction Under the CiPA Initiative. *Clinical Pharmacology & Therapeutics*, 105(2):466–475, 2019.

Z. Li, G. R. Mirams, T. Yoshinaga, B. J. Ridder, X. Han, J. E. Chen, N. L. Stockbridge, T. A. Wisialowski, B. Damiano, S. Severi, P. Morissette, P. R. Kowey, M. Holbrook, G. Smith, R. L. Rasmusson, M. Liu, Z. Song, Z. Qu, D. J. Leishman, J. Steidl-Nichols, B. Rodriguez, A. Bueno-Orovio, X. Zhou, E. Passini, A. G. Edwards, S. Morotti, H. Ni, E. Grandi, C. E. Clancy, J. Vandenberg, A. Hill, M. Nakamura, T. Singer, L. Polonchuk, A. Greiter-Wilke, K. Wang, S. Nave, A. Fullerton, E. A. Sobie, M. Paci, F. M. Tshinanu, and D. G. Strauss. General Principles for the Validation of Proarrhythmia Risk Prediction Models: An Extension of the CiPA In Silico Strategy. *Clinical Pharmacology & Therapeutics*, 107(1):102–111, 2020b.

P. Liang, F. Lan, A. S. Lee, T. Gong, V. Sanchez-Freire, Y. Wang, S. Diecke, K. Sallam, J. W. Knowles, P. J. Wang, P. K. Nguyen, D. M. Bers, R. C. Robbins, and J. C. Wu. Drug screening using a library of human induced pluripotent stem cell-derived cardiomyocytes reveals disease-specific patterns of cardiotoxicity. *Circulation*, 127(16):1677–1691, 2013.

G.-X. Liu, B.-R. Choi, O. Ziv, W. Li, E. de Lange, Z. Qu, and G. Koren. Differential conditions for early after-depolarizations and triggered activity in cardiomyocytes derived from transgenic LQT1 and LQT2 rabbits. *Journal of Physiology-London*, 590(5):1171–1180, 2012. WOS:000301491100020.

Z. Liu, R. B. Williams, and B. D. Rosen. The potential contribution of ranolazine to Torsade de Pointe. *Journal of Cardiovascular Disease Research*, 4(3):187–190, 2013.

Y. Lu, M. P. Mahaut-Smith, A. Varghese, C. L.-H. Huang, P. R. Kemp, and J. I. Vandenberg. Effects of premature stimulation on HERG K+ channels. *The Journal of Physiology*, 537(Pt 3):843–851, 2001.

C. H. Luo and Y. Rudy. A dynamic model of the cardiac ventricular action potential. I. Simulations of ionic currents and concentration changes. *Circulation Research*, 74(6):1071–96, 1994.

J. Ma, L. Guo, S. J. Fiene, B. D. Anson, J. A. Thomson, T. J. Kamp, K. L. Kolaja, B. J. Swanson, and C. T. January. High purity human-induced pluripotent stem cell-derived cardiomyocytes: electrophysiological properties of action potentials and ionic currents. *AJP: Heart and Circulatory Physiology*, 301:2006–2017, 2011.

A. Mahajan, Y. Shiferaw, D. Sato, A. Baher, R. Olcese, L.-H. Xie, M.-J. Yang, P.-S. Chen, J. G. Restrepo, A. Karma, A. Garfinkel, Z. Qu, and J. N. Weiss. A rabbit ventricular action potential model replicating cardiac dynamics at rapid heart rates. *Biophysical Journal*, 94(2): 392–410, 2008.

R. R. Makkar, B. S. Fromm, R. T. Steinman, M. D. Meissner, and M. H. Lehmann. Female gender as a risk factor for torsades de pointes associated with cardiovascular drugs. *JAMA*, 270(21):2590–7, 1993.

R. E. McAllister, D. Noble, and R. W. Tsien. Reconstruction of the electrical activity of cardiac Purkinje fibres. *The Journal of Physiology*, 251(1):1–59, 1975.

B. McMillan, D. J. Gavaghan, and G. R. Mirams. Early afterdepolarisation tendency as a simulated pro-arrhythmic risk indicator. *Toxicology Research*, 6(6):912–921, 2017a.

B. McMillan, R. H. Johnstone, D. J. Gavaghan, and G. R. Mirams. A Comparison of Existing and New Methods for Torsade de Pointes Risk Classification Based on Multi-ion Channel Screening. *Journal of Pharmacological and Toxicological Methods*, 88:207–208, 2017b.

J. Medbø and O. Sejersted. Plasma potassium changes with high intensity exercise. *The Journal of Physiology*, 421:105–122, 1990.

P. Milberg and W. Haverkamp. Verapamil prevents torsade de pointes by reduction of transmural dispersion of repolarization and suppression of early afterdepolarizations in an intact heart model of LQT3. *Basic Research in Cardiology*, 371:365–371, 2005.

G. R. Mirams, Y. Cui, A. Sher, M. Fink, J. Cooper, B. M. Heath, N. C. McMahon, D. J. Gavaghan, and D. Noble. Simulation of multiple ion channel block provides improved early prediction of compounds' clinical torsadogenic risk. *Cardiovascular Research*, 91(1):53–61, 2011.

G. R. Mirams, C. J. Arthurs, M. O. Bernabeu, R. Bordas, J. Cooper, A. Corrias, Y. Davit, S.-J. Dunn, A. G. Fletcher, D. G. Harvey, M. E. Marsh, J. M. Osborne, P. Pathmanathan, J. Pitt-Francis, J. Southern, N. Zemzemi, and D. J. Gavaghan. Chaste: an open source C++ library for computational physiology and biology. *PLoS Computational Biology*, 9(3):e1002970, 2013.

G. R. Mirams, M. R. Davies, S. J. Brough, M. H. Bridgland-Taylor, Y. Cui, D. J. Gavaghan, and N. Abi-Gerges. Prediction of Thorough QT study results using action potential simulations based on ion channel screens. *Journal of Pharmacological and Toxicological Methods*, 70(3): 246–54, 2014.

G. R. Mirams, P. Pathmanathan, R. A. Gray, P. Challenor, and R. H. Clayton. Uncertainty and variability in computational and mathematical models of cardiac physiology. *The Journal of Physiology*, 594(23):6833–6847, 2016.

S. R. Mittal. Slow junctional rhythm, QTc prolongation and transient torsades de-pointes following combined use of Ivabradine, Diltiazem and Ranolazine. *The Journal of the Association of Physicians of India*, 62(5):426–427, 2014.

J. M. Nerbonne. 3 - voltage-regulated potassium channels. In D. P. Zipes and J. Jalife, editors, *Cardiac Electrophysiology: From Cell to Bedside (Sixth Edition)*, pages 23 – 32. W.B. Saunders, Philadelphia, sixth edition edition, 2014. ISBN 978-1-4557-2856-5.

H. Nishikage, T. Nakanishi, Y. Takamitsu, and J. Yamamoto. Sequential changes in the plasma concentration of risperidone following intentional overdose. *Clinical Neuropharmacology*, 25 (6):307–9, 2002.

D. Noble. Cardiac action and pacemaker potentials based on the Hodgkin-Huxley equations. *Nature*, 188:495–497, 1960.

D. Noble. A modification of the Hodgkin—Huxley equations applicable to Purkinje fibre action and pacemaker potentials. *The Journal of Physiology*, 160:317–352, 1962.

D. Noble. Modeling the heart. *Physiology (Bethesda, Md.)*, 19:191–197, 2004.

D. Noble, A. Garny, and P. J. Noble. How the Hodgkin-Huxley equations inspired the Cardiac Physiome Project. *The Journal of Physiology*, 590(11):2613–2628, 2012.

T. O'Hara, L. Virág, A. Varró, and Y. Rudy. Simulation of the undiseased human cardiac ventricular action potential: model formulation and experimental validation. *PLoS Computational Biology*, 7(5):e1002061, 2011.

E. Passini, A. Mincholé, R. Coppini, E. Cerbai, B. Rodriguez, S. Severi, and A. Bueno-Orovio. Mechanisms of pro-arrhythmic abnormalities in ventricular repolarisation and anti-arrhythmic therapies in human hypertrophic cardiomyopathy. *Journal of Molecular and Cellular Cardiology*, 96:72–81, 2016.

E. Passini, O. J. Britton, H. R. Lu, J. Rohrbacher, A. N. Hermans, D. J. Gallacher, R. J. H. Greig, A. Bueno-Orovio, and B. Rodriguez. Human In Silico Drug Trials Demonstrate Higher Accuracy than Animal Models in Predicting Clinical Pro-Arrhythmic Cardiotoxicity. *Frontiers in Physiology*, 8, 2017.

E. Patterson, W. M. Jackman, B. J. Scherlag, and R. Lazzara. The monophasic action potential in clinical cardiology. *Clinical Cardiology*, 14(6):505–510, 1991.

E. Patterson, R. Lazzara, B. Szabo, H. Liu, D. Tang, Y. H. Li, B. J. Scherlag, and S. S. Po. Sodium-calcium exchange initiated by the Ca2+ transient: An arrhythmia trigger within pulmonary veins. *Journal of the American College of Cardiology*, 47(6):1196–1206, 2006.

S. S. Po, D. W. Wang, I. C. Yang, J. P. Johnson, L. Nie, and P. B. Bennett. Modulation of HERG potassium channels by extracellular magnesium and quinidine. *Journal of Cardiovascular Pharmacology*, 33(2):181–185, 1999.

L. Priebe and D. J. Beuckelmann. Simulation Study of Cellular Electric Properties in Heart Failure. *Circulation Research*, 82(11):1206–1223, 1998. Publisher: American Heart Association.

Z. Qu, L.-H. Xie, R. Olcese, H. S. Karagueuzian, P.-S. Chen, A. Garfinkel, and J. N. Weiss. Early afterdepolarizations in cardiac myocytes: beyond reduced repolarization reserve. *Cardiovascular research*, 99(1):6–15, 2013.

D. Rampe, M. L. Roy, A. Dennis, and A. M. Brown. A mechanism for the proarrhythmic effects of cisapride (Propulsid): High affinity blockade of the human cardiac potassium channel HERG. *FEBS Letters*, 417(1):28–32, 1997.

S. E. Rau, J. R. Bend, J. M. O. Arnold, L. T. Tran, J. D. Spence, and D. G. Bailey. Grapefruit juice—terfenadine single-dose interaction: Magnitude, mechanism, and relevance. *Clinical Pharmacology & Therapeutics*, 61(4):401–409, 1997.

W. S. Redfern, L. Carlsson, A. S. Davis, W. G. Lynch, I. MacKenzie, S. Palethorpe, P. K. Siegl, I. Strang, A. T. Sullivan, R. Wallis, A. J. Camm, and T. G. Hammond. Relationships between preclinical cardiac electrophysiology, clinical QT interval prolongation and torsade de pointes for a broad range of drugs: evidence for a provisional safety margin in drug development. *Cardiovascular Research*, 58(1):32–45, 2003.

D. M. Roden. Early after-depolarizations and Torsade-De-Pointes - implications for the control of cardiac-arrhythmias by prolonging repolarization. *European Heart Journal*, 14:56–61, 1993.

D. M. Roden. Taking the "idio" out of "idiosyncratic": predicting torsades de pointes. *Pacing and clinical electrophysiology: PACE*, 21(5):1029–1034, 1998.

D. M. Roden and R. L. Abraham. Refining repolarization reserve. *Heart Rhythm*, 8(11):1756–1757, 2011.

Roden Dan M. Repolarization Reserve. *Circulation*, 118(10):981–982, 2008.

R. A. Rose and P. H. Backx. 2 - calcium channels in the heart. In D. P. Zipes and J. Jalife, editors, *Cardiac Electrophysiology: From Cell to Bedside (Sixth Edition)*, pages 13 – 22. W.B. Saunders, Philadelphia, sixth edition edition, 2014. ISBN 978-1-4557-2856-5.

P. T. Sager. Key clinical considerations for demonstrating the utility of preclinical models to predict clinical drug-induced torsades de pointes. *British Journal of Pharmacology*, 154(7): 1544–1549, 2008.

P. T. Sager, G. Gintant, J. R. Turner, S. Pettit, and N. Stockbridge. Rechanneling the cardiac proarrhythmia safety paradigm: A meeting report from the Cardiac Safety Research Consortium. *American Heart Journal*, 167(3):292–300, 2014.

D. Sato, L.-H. Xie, A. A. Sovari, D. X. Tran, N. Morita, F. Xie, H. Karagueuzian, A. Garfinkel, J. N. Weiss, and Z. Qu. Synchronization of chaotic early afterdepolarizations in the genesis of cardiac arrhythmias. *Proceedings of the National Academy of Sciences of the United States of America*, 106(9):2983–2988, 2009.

D. Sato, C. E. Clancy, and D. M. Bers. Dynamics of sodium current mediated early afterdepolarizations. *Heliyon*, 3(9):e00388, 2017. WOS:000432025800017.

J. W. Schleifer, D. Sorajja, and W.-K. Shen. Advances in the pharmacologic treatment of ventricular arrhythmias. *Expert Opinion on Pharmacotherapy*, 16(17):2637–2651, 2015.

P. J. Schwartz, L. Crotti, and R. Insolia. Long-QT syndrome from genetics to management. *Circulation: Arrhythmia and Electrophysiology*, 5(4):868–877, 2012.

B. M. Scirica, D. A. Morrow, H. Hod, S. A. Murphy, L. Belardinelli, C. M. Hedgepeth, P. Molhoek, F. W. A. Verheugt, B. J. Gersh, C. H. McCabe, and E. Braunwald. Effect of ranolazine, an antianginal agent with novel electrophysiological properties, on the incidence of arrhythmias in patients with non-ST-segment-elevation acute coronary syndrome. *Circulation*, 116 (15):1647–1652, 2007.

M. Segers. *Le rôle des potentiels tardifs du coeur.* Mémoires de l'Académie Royale de Médecine de Belgique: Collection in octavo. 1941.

A. Selzer and H. W. Wray. Quinidine Syncope. Paroxysmal ventricular fibrillation occurring during treatment of chronic atrial arrhythmias. *Circulation*, 30:17–26, 1964.

T. R. Shannon, F. Wang, J. Puglisi, C. Weber, and D. M. Bers. A mathematical treatment of integrated Ca dynamics within the ventricular myocyte. *Biophysical Journal*, 87(5):3351–71, 2004.

L. Sherwood. *Human Physiology - From Cells to Systems.* Thomson/Brooks/Cole, 5th edition, 2004. ISBN 0534395015.

W. Shimizu and C. Antzelevitch. Sodium channel block with mexiletine is effective in reducing dispersion of repolarization and preventing Torsade de Pointes in LQT2 and LQT3 models of the Long-QT Syndrome. *Circulation*, 96(6):2038–2047, 1997.

W. Shimizu and C. Antzelevitch. Cellular basis for the ECG features of the LQT1 form of the Long-QT Syndrome. *Circulation*, 98(21):2314–2322, 1998.

S. Sicouri and C. Antzelevitch. A subpopulation of cells with unique electrophysiological properties in the deep subepicardium of the canine ventricle: the M cell. *Circulation Research*, 68 (68):1729–1741, 1991.

Y. Song, J. C. Shryock, S. Wagner, L. S. Maier, and L. Belardinelli. Blocking late sodium current reduces hydrogen peroxide-induced arrhythmogenic activity and contractile dysfunction. *The Journal of Pharmacology and Experimental Therapeutics*, 318(1):214–222, 2006.

S. Sridhar, N. Vandersickel, and A. V. Panfilov. Effect of myocyte-fibroblast coupling on the onset of pathological dynamics in a model of ventricular tissue. *Scientific Reports*, 7:40985, 2017. WOS:000392375900001.

B. Y. P. Stern, F. A. Edwards, and B. Sakmann. Relation between Na+-K+ pump, Na+ activity and force in strophanthidin inotropy in sheep cardiac Purkinje fibres. *The Journal of Physiology*, (404):247–278, 1992.

N. Stockbridge, J. Morganroth, R. R. Shah, and C. Garnett. Dealing with global safety issues. *Drug Safety*, 36(3):167–182, 2013.

A. L. Tarca, V. J. Carey, X.-W. Chen, R. Romero, and S. Drăghici. Machine learning and its applications to Biology. *PLoS Computational Biology*, 3(6):e116, 2007.

K. H. W. J. ten Tusscher and A. V. Panfilov. Alternans and spiral breakup in a human ventricular tissue model. *AJP: Heart and Circulatory Physiology*, 291(3):H1088–1100, 2006.

K. H. W. J. ten Tusscher, D. Noble, P. J. Noble, and A. V. Panfilov. A model for human ventricular tissue. *AJP: Heart and Circulatory Physiology*, 286(4):H1573–H1589, 2003.

G. Thomas, M. Chung, and C. J. Cohen. A dihydropyridine (Bay K 8644) that enhances calcium currents in guinea pig and calf myocardial cells. A new type of positive inotropic agent. *Circulation Research*, 56(1):87–96, 1985.

J. Tomek, A. Bueno-Orovio, E. Passini, X. Zhou, A. Minchole, O. Britton, C. Bartolucci, S. Severi, A. Shrier, L. Virag, A. Varro, and B. Rodriguez. Development, calibration, and validation of a novel human ventricular myocyte model in health, disease, and drug block. *eLife*, 8, 2019.

D. X. Tran, D. Sato, A. Yochelis, J. N. Weiss, A. Garfinkel, and Z. Qu. Bifurcation and Chaos in a Model of Cardiac Early Afterdepolarizations. *Physical Review Letters*, 102(25):258103, 2009. Publisher: American Physical Society.

K. E. Trinkley, R. L. Page, H. Lien, K. Yamanouye, and J. E. Tisdale. QT interval prolongation and the risk of torsades de pointes: essentials for clinicians. *Current Medical Research and Opinion*, 29(12):1719–26, 2013.

K. Tsumoto, Y. Kurata, K. Furutani, and Y. Kurachi. Hysteretic Dynamics of Multi-Stable Early Afterdepolarisations with Repolarisation Reserve Attenuation: A Potential Dynamical Mechanism for Cardiac Arrhythmias. *Scientific Reports*, 7(1):10771, 2017. Number: 1 Publisher: Nature Publishing Group.

A. I. Undrovinas, L. Belardinelli, N. A. Undrovinas, and H. N. Sabbah. Ranolazine improves abnormal repolarization and contraction in left ventricular myocytes of dogs with heart failure by inhibiting late sodium current. *Journal of Cardiovascular Electrophysiology*, 17:1–20, 2006.

R. Urso, P. Blardi, and G. Giorgi. A short introduction to pharmacokinetics. *European Review for Medical and Pharmacological Sciences*, 6(2):33–44, 2002.

H. H. Valdivia. 6 - structural and molecular bases of sarcoplasmic reticulum ion channel function. In D. P. Zipes and J. Jalife, editors, *Cardiac Electrophysiology: From Cell to Bedside (Sixth Edition)*, pages 55 – 69. W.B. Saunders, Philadelphia, sixth edition edition, 2014. ISBN 978-1-4557-2856-5.

E. Van Nieuwenhuyse, G. Seemann, A. V. Panfilov, and N. Vandersickel. Effects of early afterdepolarizations on excitation patterns in an accurate model of the human ventricles. *Plos One*, 12(12):e0188867, 2017. WOS:000417337800045.

N. Vandersickel, I. V. Kazbanov, A. Nuitermans, L. D. Weise, R. Pandit, and A. V. Panfilov. A Study of Early Afterdepolarizations in a Model for Human Ventricular Tissue. *PLOS ONE*, 9 (1):e84595, 2014.

N. Vandersickel, T. P. d. Boer, M. A. Vos, and A. V. Panfilov. Perpetuation of torsade de pointes in heterogeneous hearts: competing foci or re-entry? *The Journal of Physiology*, 594(23):6865–6878, 2016. _eprint: https://physoc.onlinelibrary.wiley.com/doi/pdf/10.1113/JP271728.

A. O. Verkerk, M. W. Veldkamp, N. De Jonge, R. Wilders, and A. C. Van Ginneken. Injury current modulates afterdepolarizations in single human ventricular cells. *Cardiovascular Research*, 47(1):124–132, 2000.

P. G. A. Volders, M. A. Vos, B. Szabo, K. R. Sipido, S. H. M. De Groot, A. P. M. Gorgels, H. J. J. Wellens, and R. Lazzara. Progress in the understanding of cardiac early afterdepolarizations and torsades de pointes: Time to revise current concepts. *Cardiovascular Research*, 46(3): 376–392, 2000.

W. Trautwein, U. Gottstein, and J. Dudel. Der Aktionsstrom der Myokardfaser im Sauerstoffmangel. *Pflügers Archiv*, 60, 1954.

J. W. Warmke and B. Ganetzky. A family of potassium channel genes related to eag in Drosophila and mammals. *Proceedings of the National Academy of Sciences of the United States of America*, 91(8):3438–3442, 1994.

L. D. Weise, A. V. Panfilov, T. Nakajima, Y. Hosoya, and H. Fujita. A Discrete Electromechanical Model for Human Cardiac Tissue: Effects of Stretch-Activated Currents and Stretch Conditions on Restitution Properties and Spiral Wave Dynamics. *PLoS ONE*, 8(3):e59317, 2013.

D. G. Whittaker, R. A. Capel, M. Hendrix, X. H. S. Chan, N. Herring, N. J. White, G. R. Mirams, and R.-A. B. Burton. Cardiac TdP risk stratification modelling of anti-infective compounds including chloroquine and hydroxychloroquine. *Royal Society Open Science*, 8(4):rsos.210235, 210235, 2021.

Wikimedia Commons. File:diagram of the human heart (cropped).svg — wikimedia commons, the free media repository, 2016. [Online; accessed 8-August-2017].

G. Williams and G. R. Mirams. A web portal for in-silico action potential predictions. *Journal of Pharmacological and Toxicological Methods*, 75:10–16, 2015.

B. Wiśniowska and S. Polak. Am I or am I not proarrhythmic? Comparison of various classifications of drug TdP propensity. *Drug Discovery Today*, 22:10–16, 2017.

A. L. Wit. Afterdepolarizations and triggered activity as a mechanism for clinical arrhythmias. *Pacing and Clinical Electrophysiology*, 41(8):883–896, 2018.

R. L. Woosley, Y. Chen, J. P. Freiman, and R. A. Gillis. Mechanism of the cardiotoxic actions of terfenadine. *JAMA*, 269(12):1532–1536, 1993.

L. Wu, D. Guo, H. Li, J. Hackett, G.-X. Yan, Z. Jiao, C. Antzelevitch, J. C. Shryock, and L. Belardinelli. Role of late sodium current in modulating the proarrhythmic and antiarrhythmic effects of quinidine. *Heart Rhythm*, 5(12):1726–1734, 2008.

L. H. Xie, F. Chen, H. S. Karagueuzian, and J. N. Weiss. Oxidative stress-induced afterdepolarizations and calmodulin kinase II signaling. *Circulation Research*, 104(1):79–86, 2009.

Y. Xie, D. Sato, A. Garfinkel, Z. Qu, and J. N. Weiss. So Little Source, So Much Sink: Requirements for Afterdepolarizations to Propagate in Tissue. *Biophysical Journal*, 99(5):1408–1415, 2010. Publisher: Elsevier.

M. Yamada, K. Ohta, A. Niwa, N. Tsujino, T. Nakada, and M. Hirose. Contribution of L-type Ca2+ channels to early afterdepolarizations induced by I Kr and I Ks channel suppression in guinea pig ventricular myocytes. *The Journal of Membrane Biology*, 222(3):151–166, 2008.

Y. G. Yap and A. J. Camm. Drug induced QT prolongation and Torsades de Pointes. *Heart*, 89: 1363–1372, 2003.

Z. Zhao, H. Wen, N. Fefelova, C. Allen, A. Baba, T. Matsuda, and L.-H. Xie. Revisiting the ionic mechanisms of early afterdepolarizations in cardiomyocytes: predominant by Ca waves or Ca currents? *American Journal of Physiology-Heart and Circulatory Physiology*, 302(8): H1636–H1644, 2012. WOS:000302911500010.

Corrections

1. In terms of scientific writing, conclusions are limited to a brief repetition of findings, without these being placed on a wider context.

The discussion and conclusion chapters have been rewritten.

2. Result chapters would also benefit from a clear exposition of underlying hypotheses and their rationale.

The results chapters have been combined and rewritten.

3. Please improve quality of Figures 2.2, 2.3, 2.5 and 3.1.

Please see updated Figures 2.2, 2.3, and 2.5 on pages 16, 16, and 21. Figure 3.1 has been removed as it was related to the unpublished paper discussed below.

4. When referring to your results as investigations on model choice for safety predictions, please clarify that this relates to endocardial vs epicardial variants, and not to different ionic models.

This has been clarified wherever mentioned.

5. Positive shift of sodium channel inactivation as a representation of SC5NA mutations in Brugada Syndrome: Although the study by Chen et al. (Nature 1998;392:293–296) on T160M mutant sodium channels showed a faster recovery from inactivation in Xenopus oocytes, later work by Baroudi et al. (FEBS Letters 2000;467: 12–16) proved a different phenotype for mutation T1620M when expressed in mammalian cells, leading to a slower recovery from inactivation. This is consistent with results from Deschênes et al. (Cardiovasc Res 2000:46;55–65), Shirai et al. (Cardiovasc Res 2000;53:348–354) or Tan et al. (Am J Physiol Heart Circ Physiol 2006;291:H1822–H1828), to cite some, in which a slowing of recovery from inactivation is observed for a wide variety of SCN5A mutations. Unless strong evidence supporting a faster recovery from inactivation in SCN5A mutations can be provided, please remove any claims linking your results with Brugada Syndrome.

Without a solid basis in the literature for using a positive fast sodium current inactivation curve shift for proarrhythmic risk classification, I've omitted this intervention from the thesis entirely, but results are still available in the supplementary materials.

6. Chapter 2, Page 43: Confusing interpretation of the experiments by Patterson et al. 2006. Please revisit the mechanisms of EAD generation in pulmonary vein cells with a short action potential duration.

The paragraph in Section 3.4.2 on page 46 has been updated.

7. Chapter 2, description of human ventricular mathematical models: Please provide the rationale behind those described. Several statements are misleading. Ten Tusscher et al. model: "This model was able to produce a re-entrant spiral wave when used in a 2D tissue model". Relevance for this thesis? Earlier models did as well. Grandi et al. model: "The modified Grandi model was able to reproduce several human myocyte behaviours including rate adaptation and calcium transient

dynamics". Others were unable?

Section 2.3.4 (page 25) has been re-written to give an updated and revised history of human electrophysiological models.

8. Chapter 4: Please specify drug risk classes in Table 4.1. shown.

Risk categories have been added to Table 4.1 on page 63.

9. Page 66: "As there is a great deal of overlap in the categories, as we have shown graphically in the previous sections". Neither classes nor overlaps shown.

Figure 4.1 has been added on page 62 to show the overlap graphically.

10. Chapter 5, Figures 5.13 and 5.14: Please elaborate your description and interpretation of these figures. For example, referring to Fig. 5.14, the thesis reads: "The optimal leaf ordering algorithm was moderately successful in sorting the drugs in ascending order of torsadogenic risk". For which of the metrics shown?

The figures in the results chapter have been re-made and the descriptions have been updated.

11. Chapter 6, Page 98: Please indicate EAD thresholds in the absence of drug action for the different cycle lengths considered, to facilitate comparisons with thresholds at 3s pacing. Page 98: There are several typos in reporting metric differences for the hERG block EAD protocol.

The EAD thresholds at control have been added to Figure 5.16 on page 97.

12. Chapter 7, terminology: Please use throughout injury instead of electrotonic current.

This description has been updated wherever used.

13. Page 113: "This indicates that the choice of model for EAD prediction must be based on the choice of classification method." This should be the opposite.

The interpretation of results with respect to classification methods has been updated throughout the thesis, and this particular sentence has been removed.

14. Supplementary materials and codes must be deposited in ORA for future access, and properly referenced with their respective DOI.

The supplementary material and code are now provided along with the thesis, ready to be uploaded to ORA when the thesis is.

15. - Frequent misspellings: "adrinergic", "isoproterinol", "dilitazem" 16. - Page 51: "This lead" ¿¿ "This led" 17. - Page 78: Misspelling of afterdepolarisations 18. - Page 83: Typesetting of IC50 19. - Page 112: predicition -¿ prediction 20. - Page 131: phrase -¿ phase. Table 7.1 calls errors as accuracy. 21. - Page 135: electrophyiological modelling -¿ electrophysiological modelling 22. - Duplicated references: Dutta et al (2016a) and (2016b); Dutta et al (2017a) and (2017b); Li et al (2017a) and (2017b). Unpublished reference: Noble et al (in preparation, 2017).

These typos and references have been corrected.

23. The Literature Review needs to be brought to date to cover the work on EADs over the last 10 years, especially from the computational point of view (and from single cell to organ levels).

The literature review has been expanded and rewritten.

24. Most of this and subsequent result chapters heavily rely on an unpublished work for the choice of insults in the proposed EAD method for proarrhythmic risk prediction (Noble et al., 2017). Alternative routes for the justification of such interventions need to be sought.

Discussion of the unpublished work has been removed, and discussion of the choice of the interventions has been added to Section 3.5.1 on page 54.

25. In most chapters, the conclusion section is merely some sentences linking to the next chapter, rather than an actual conclusion.

The conclusion sections in each chapter have been rewritten.

26. Result chapters require a clear exposition of underlying hypotheses and their rationale, beyond the exposition of already well known facts.

The results chapters have been combined and rewritten.

27. The structure of these chapters also needs to be revisited, removing redundant methods sections that are just a repetition of the Methods chapter of the thesis. Crucial methodological details could be just reminded when describing the results.

The thesis chapters have been reorganised and the redundant methods sections have been removed.

28. Discussions need to go beyond a brief summary of the results, presenting a well-informed discussion within the context of the wider literature.

Chapter 6 (page 119) has been rewritten.

29. The Conclusions chapter should further highlight the novelty of the work and should also be much related to the objectives of the thesis.

Chapter 7 (page 131) has been rewritten.

30. Chapter 4, "Computational Methods". Further justification is required for the following methodological aspects, at least discussing their expected influence on the thesis results: 31. - Choice of ionic model for safety predictions: recent model improvements (Tomek et al. 2019) have been cited very superficially. However, some of these (e.g. plateau levels, or changes in ICaL and effects of drug block) could significantly affect the results presented in this thesis.

The expected influence of model choice and benefits of each option are now discussed in Section 6.3 on 121 and page 123.

32. - Choice of constant Hill coefficient of 1 for the modelling of drug block effects.

Additional references for this decision have been added to Section 4.2.1 on page 64.

33. - Choice of magnitudes for EADs insults (e.g. range of 80-fold increase for ICaL).

Further discussion of this has been added in Section 4.2.1 (page 67).

34. - Choice of duration of EAD insult protocols (model stabilization with drug action, then followed by only 4 beats after the specific EAD intervention).

Further discussion of this has been added in Section 4.2.1 (page 67) and Section 6.3 (page 121).

35. - Changes in protocols with respect to previous studies (cycle length for bradycardia vs O'Hara et al. 2011; injury current protocols vs Dutta et al. 2016).

The effect of cycle length on EAD thresholds and risk classification are investigated in Section 5.4.1

36. - Choice of LDA and SVM as classification methods vs alternatives, as classification accuracy heavily relies on the method used.

An overview of the options for machine learning classification methods has been added in Section 3.5.2 on page 55, and the effect on the results are discussed in Section 5.3.1 on page 90 and Section 6.4 on page 126.

37. - Choice of metrics for drug-induced proarrhythmic predictions, such as the use of outdated versions of proposed CiPA's metrics (cqInward vs qNet).

qNet has been added to the metrics considered in this paper.

38. Chapter 6, "Modulators of EADs as a pro-arrhythmic risk indicator". From the examiners' point of view, the biggest limitation of this study is the absence of mechanistic explanations on the observed pro-arrhythmic responses. As presented,

results read as a plain description of model outputs (more or less EADs under this intervention, this method more accurate here for classification. . .), without providing any interpretation or implications. Although the roles of the explored modulators of EADs are in general well-known (ratedependence, modulation of outward currents by extracellular potassium, cell type differences), we believe an angle that would make the work of publishable quality is a detailed analysis of the specific influence of each of these factors under drug action. In this regard, we would welcome a complementary analysis on the following aspects: 39. - Differential mechanisms of outliers in each arrhythmic class category under increased pacing cycle length (Figure 6.2).

This has been added to Section 5.4.1 on page 97.

40. - Differential mechanisms of outliers in each arrhythmic class category under varying extracellular potassium concentration, especially in terms of abnormal biphasic responses (Figure 6.4).

This has been added to Section 5.4.2.

41. - Differential mechanisms of outliers in each arrhythmic class underlying biphasic responses to drug exposure (Figure 6.6).

This has been added to Section 5.4.3.

42. - Improved description of classification results. What insight is gained from simply reporting LDA/SVM accuracies for each modulation and different EAD insults? (i.e. this more accurate in this case, the other works better for this other intervention. . .). Efforts need to be made in order to deliver a clear take-home message in terms of the most accurate predictor across the considered interventions. Moreover, the different interventions are only analysed in isolation. Investigations would be welcome on whether their combination would improve the prediction accuracy.

An overall comparison, including combinations of metrics, has been included in Section 5.5. Please note that the results of the error calculations have changed from the original thesis, as I have corrected the classification of ranolazine from risk category 3 to risk category 4.

43. - In general, figures would be easier to understand if the IKr EAD axis goes from 1 to 0 (instead of 0 to 1) to represent an increasing EAD intervention (increasing block of IKr).

This has been updated in all relevant figures.

44. - For investigations on cell type differences, and for consistency throughout the thesis, results should also cover EADs insults by shifts in sodium channel inactivation. Even if the epicardial model may not contain by default the required metadata in order to directly alter this property, there is no excuse for not incorporating such a minor change for a DPhil candidate in Computer Science.

As discussed above, the fast sodium current inactivation curve shift has been removed from the thesis due to a lack of biological basis for it. However, in the process of running simulations using the epicardial model, I have discovered that I added fast sodium shift to the epicardial model in the Chaste CellML repository in 2016 (at the same time as I added it to the endocardial model in the repository), but this was removed from later revisions of the main Chaste code, and apparently I forgot that I'd done it.

45. Chapter 7, "Electrotonic current". A more extensive literature research needs to be presented in this chapter to better set its context. In terms of mechanisms and further discussion, we believe the following points would reinforce the contents of this chapter: 46. - Only ICaL reactivation is mentioned as a possible mechanism for EADs onset under the application of an injury current. Are there any other inward/outward currents affected by its application?

A new section discussing the ionic mechanisms for EAD onset has been added to the literature review as Section 3.4.2 on page 42, and the specific mechanisms found for all of our interventions have been added to Section 5.1.2 on page 79.

47. - On visual evaluation, the results from Figure 7.11 suggest a good overlap if they were plotted together for all the considered durations of the injury current. Does this indicate that the proposed protocol for triggering EADs is basically regulated by baseline membrane kinetics, regardless of drug action? If so, what would be its usefulness for drug safety prediction?

The injury current intervention results are now plotted against other metrics in Figure 5.13. All of the metrics calculated in this study have similarly large amounts of overlap between risk categories, including those previously reported in the literature (Section 6.3 contains a discussion of the differences in input data that influence this difference). Approaches such as using linear discriminant analysis and combining metrics together can help to separate overlapping groups. The injury current is no worse in this regard than most of the metrics considered in this work.

48. - The last part of the results section (page 130) reads: "In figure 7.16, the EAD thresholds are plotted against the three official CiPA risk categories. There is some separation between the risk categories – in general, the most torsadogenic drugs (category 1) have a lower EAD threshold than the least torsadogenic drugs". This seems in apparent disagreement with the results presented in the referred figure, where all risk categories mostly overlap within 0.01 pApF-1. Again, what are the implications of such a narrow margin for drug safety predictions, and how does this affect the performance of the tested classifiers? Would this metric provide complementary information when used in conjunction with the metrics from the previous chapters?

Injury current in combination with other metrics is assessed in Section 5.3.2.

49. - What is the interest of considering CiPA risk categories? An effort of comparison with other studies using CiPA risk categories for classification should be made in the discussion of this chapter.

A discussion of different risk categorisation systems has been added in Section 3.5.3, and instead of using the CiPA categories - as I agree that this doesn't offer a lot of information over my original classes - I have instead investigated using a binary classifier to assess the utility of each metric when no intermediate categories are considered, to offer more information about the specific types of problem that each metric performs best at. This can be found in Section 5.3.3 on page 94.